THESIS FOR THE DEGREE OF DOCTOR OF PHILOSOPHY

Spatial Analysis and Modelling Motivated by Nerve Fiber Patterns

VIKTOR OLSBO

CHALMERS | GÖTEBORG UNIVERSITY

Department of Mathematical Sciences
Chalmers University of Technology
and University of Gothenburg
Göteborg, Sweden 2008

Spatial Analysis and Modelling Motivated by Epidermal Nerve Fibers
VIKTOR OLSBO
ISBN 978-91-7385-202-9

Doktorsavhandlingar vid Chalmers Tekniska Högskola
Ny serie nr 2883
ISSN 0346-718X

Department of Mathematical Sciences
Chalmers University of Technology and University of Gothenburg
SE-412 96 Göteborg
Sweden
Telephone + 46 (0)31-772 1000

Spatial Analysis and Modelling Motivated by Epidermal Nerve Fiber Patterns
VIKTOR OLSBO
Department of Mathematical Sciences
Chalmers University of Technology and University of Gothenburg

Abstract

Recent breakthroughs in imaging of skin tissue reveal new details on the distribution of nerve fibers in the epidermis. This thesis deals with analysis and modelling of such patterns. Our particular interest lies in comparing between epidermal nerve fiber patterns coming from healthy subjects and patterns coming from subject suffering from diabetes. Development of diagnostic statistical tools for determining early stages of diabetic neuropathy may allow diagnosis early in the progress of the disease when neuropathy is most likely to respond to treatment. In this thesis we suggest some spatial analysis techniques to detect differences in ENF patterns coming from subjects in different states of neuropathy. Furthermore, we introduce a set of models based on bivariate point processes serving as a starting point in modelling nerve fiber patterns. Fiber-like patterns are constructed by connecting the points of the processes, according to predetermined rules, via a line segment. We also derive integral formulas for the correlation between the volumes of the typical Poisson-Voronoi cell and the typical Stienen sphere in arbitrary dimensions.

Key words: Diabetic neuropathy, Epidermal nerve fibers, K-function, Poisson process, Pair-correlation function, Random set generated Cox process, Spatial point/fiber process, Stienen model, Voronoi tessellation

Acknowledgements

I would like to thank the following people:

My advisors Aila Särkkä, Tommy Norberg and Mats Kvarnström for encouragement, ideas, advise and a lot of patience. Without your help, this thesis would not be.

Lance Waller for great ideas and interesting discussions. Also the whole Waller family for their hospitality and warmth.

Everyone at the departement, and to mention a few among the ”seniors” that have had an extra impact on me during my years at mathematical sciences: Patrik Albin, Rossitza Dodunekova, Olle Häggström, Jacques de Mare, Torgny Lindvall, Holger Rootzén, Mats Rudemo and Kerstin Wiklander. Furthermore, Marianne Rossander-Bäckström for untiringly lending a helping hand with any administrative issues.

A special thanks goes to Anastassia Baxevani, Erik Brodin, Mikael Persson, Mattias Sundén, Johan Tykesson and Marcus Warfheimer for companionship and also to innebandygänget for many great games and good exercise.

My family and friends for everything.

Most of all I would like to thank Maja, Leon and Lilja for love, support and inspiration.

This work is dedicated to Inga Olsbo *19110913-20080203*, for always believing in me.

This thesis consists of the following papers:

Paper I: KENNEDY, W.R., OLSBO, V., SÄRKKÄ, A., WALLER, L., WENDELSCHAFER-CRABB, G. (2008) *Second-Order Spatial Analysis of Epidermal Nerve Fibers*, Submitted to *Statistics in Medicine*

Paper II: OLSBO, V. (2008) *A marked Poisson process induced by a random set generated Cox process*, Submitted.

Paper III: OLSBO, V. AND WALLER, L. (2008) *Development and evaluation of spatial point process models of epidermal nerve fibers*, Submitted to *Interface*.

Paper IV: OLSBO, V. (2007) *On the correlation between the volumes of the typical Poisson-Voronoi cell and the typical Stienen sphere*, Adv. Appl. Prob., **39**, 883-892.

Contents

Chapter 1

Introduction

Stochastic geometry and spatial statistics are important tools to model and analyse random geometric structures. They are used in a variety of fields such as forestry, astronomy, epidemiology, medicine, material science, economy and telecommunication, to name a few. In this thesis we are interested in modeling and analysing *epidermal nerve fiber* (ENF) patterns. ENFs are sensory fibers in the most outer layer of the skin (epidermis) and sense touch, heat, pain etc. An introduction to stochastic geometry can be found in [21] and for a more specific look at spatial statistics and point processes we suggest [2] and [3].

Epidermal nerve fibers grow from what is known as a *dorsal root ganglion cell*, a cell which relays sensory information to the central nervous system, to the basement membrane of the dermis and then grows from a trunk up into the epidermis and branch out. Although ENFs had long been assumed to exist, partly by theoretical assumptions and some empirical observations, no conclusive evidence of their existence was available until the late 1980:s [22, 7]. The development of both staining and imaging led to the possibility to establish the existence of ENFs via confocal microscopy. Once methods for visualizing and identifying ENFs were established, research quickly moved toward quantification of such fibers, especially to assess their potential diagnostic value. In particular, Kennedy *et al*. [8] report diminished numbers of ENFs per surface area in subjects suffering from *diabetic neuropathy*, described more in detail below, as well as reduced summed length of ENFs per volume, that is, reduced "coverage" of the epidermis by ENFs. For a more in-depth introduction to ENFs the reader is referred to the introduction in the first paper of the thesis, Paper I. In Figure 1.1 a side view of nerve fibers is displayed.

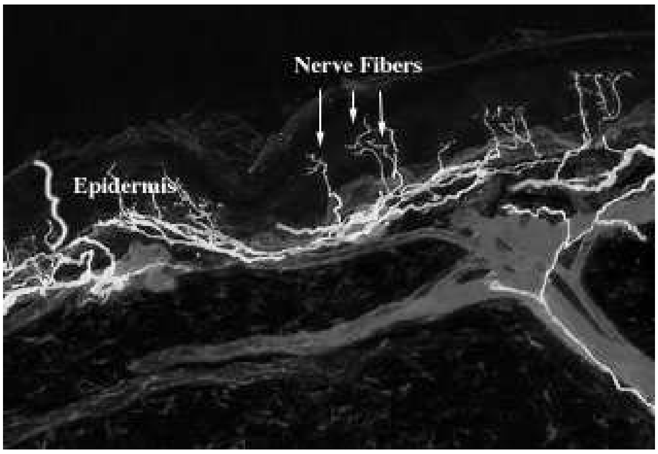

Figure 1.1: *Nerve fibers in the epidermis.*

The interest in ENFs lies not just in an overall picture but more specific, as described above, in their potential diagnostic value in connection to diabetic neuropathy. Diabetic neuropathy is a family of nerve disorders which a person with diabetes potentially can suffer from. As many as 65 percent of all diabetic patients suffer from neuropathies. There are four classes of neuropathies, *peripheral, autonomic, proximal* and *focal*. We are focused on peripheral diabetic neuropathy, which affects and displays symptoms in peripheral parts of the body, i.e. toes, feet, legs, hands, and arms. The symptoms include numbness, tingling, sharp pains, extreme sensitivity to touch and loss of balance and coordination, to name a few. There are no methods for early diagnose of this disease, and symptoms often appear at the point when treatment is ineffective. If changes in ENF patterns appear early in the disease state then the idea is to use point pattern analysis as a diagnostic tool.

In Paper I, we perform an exploratory analysis of the pattern of nerve trunks, which is the point at which the fiber enters the epidermis. Here we are using second-order quantitative methods from point process theory. We are trying to detect systematic differences in patterns coming from subjects with different degrees of diabetic neuropathy. There are four different classes in which the subjects are divided into. These are named *normal, mild, moderate* and *severe*, where normal means non-diabetic. The classification is done according to medical and physical testing.

In Paper II we present a class of marked Poisson process models, motivated by ENF. These are based on a bivariate point process (Φ_b, Φ_e) where the base process Φ_b is a

Poisson process and the ending process Φ_e is a *random set generated Cox process* (RSGCP), a point process model introduced by Penttinen and Niemi [17]. In an ENF setting the random closed set in the RSGCP represents an underlying heterogeneity affecting the ending process. The fiber pattern is obtained by connecting each point of the ending process to its nearest neighbor in the base process. This type of construction, when also Φ_e is a homogenous Poisson process, was introduced by Foss and Zuyev [6] as a model for telecommunication networks. In the third paper, Paper III, we explore two further point process models for modelling ENF patterns. The first is based on two independent Poisson processes. Each point in Φ_e is connected via a line segment to a randomly chosen point of Φ_b. In the second model Φ_b can be a general point process and serves as parent process in a Neyman-Scott type of cluster process, where the points in Φ_e are the offsprings. We scatter the offspring around the parent points and connect them to their respective parent point via a line segment. In both Paper II and Paper III, we look at quantities such as number of branches per base, branch lengths (individual and total) and angle distribution (the angle between an x-axis going trough the base point and the line segment connecting the ending point). In the RSGCP and the first approach of Paper III full distributional results are hard to obtain and most results concern the first two moments. In the second approach of Paper III we define these distributions of main characteristics ourselves. In Figure 1.2 a birds-eye view of ENF patterns is displayed. The models introduced in Paper II could be used as starting points when modelling the nerve fiber patterns. These models were however developed without having data and are of a more speculative and hypothetical nature. After obtaining data, the models in Paper II were modified according to what we observed. This process resulted in Pa-

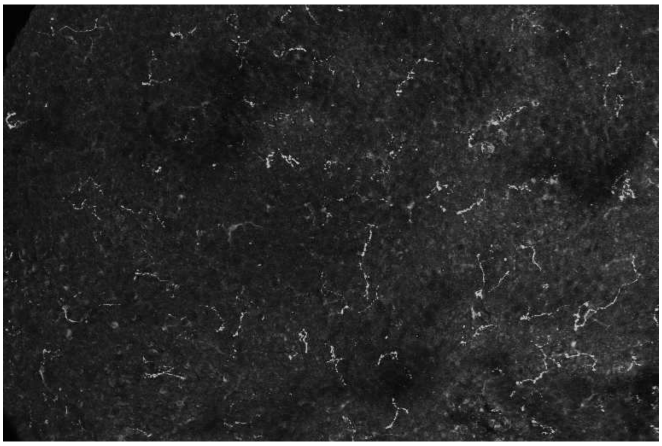

Figure 1.2: *Sample from a non-diabetic patient.*

per III. During the data mining process we discovered that the constraint that ending only connects to the nearest base was not valid. Still, most endings were connecting to their respective nearest neighbor in the base process but some did connect to the second nearest or the third nearest and so on. That was the reason why we introduced a modified version of the model in Paper II. We further confined to the case when Φ_e is a homogenous Poisson process. Still, the models are very simple and we only look at a few limited features of the underlying structures. Most likely more realistic models are also more complex leading to simulation based approaches. Furthermore, the models we discuss are in 2 dimensions but the ”true” data is in 3D. Since the fibers first shoot up and then start to spread out in a narrow band, a 2D-model is appropriate but it would be worth investigating whether 3D models would give some additional advantage. Also some dynamic time-space modelling should be of interest. There are some very interesting aspects of nerve fiber growth in connection with skin wounds.

The last paper, Paper IV, is of a more theoretical character and deals with the correlation between the volumes of the typical Poisson-Voronoi cell and the typical Stienen sphere in arbitrary dimensions. On the real line an analytical expression is obtained, and for $d \geq 2$ an integral formula is given. Using this formula it is possible to obtain numerical estimates of the correlation in arbitrary dimensions.

The outline of the thesis is as follows. In Chapter 2 we give some basics of stochastic geometry and spatial statistics. This section serves as a brief guide to the background material needed to better understand the appended papers. Further, in Chapter 3 we give summaries of Paper I-IV.

Chapter 2

Stochastic Geometry

In this introduction we will try to give the background on stochastic geometry and spatial statistics needed to read the four papers. First we give a general definition of point processes in $\mathbb{R}^d$ and recall some point process models which are then further discussed in the articles. In Paper IV we regard a d-dimensional Poisson process, while in Papers I-III only planar point process theory is needed. Further, estimation techniques (in 2D) of some commonly used statistics is discussed in Section 2.1.3. In Paper I we regard the ENFs as realizations of fibre processes and therefore we give some basic definitions in Section 2.2. The Voronoi tessellations and Stienen model are discussed in Section 2.3. If the end points of the ENFs are connected to the nearest base point, they are connected to the base that is in the same Voronoi cell, based on the tessellation generated by the base points. Furthermore, the Stienen model is studied further in Paper I and Paper IV.

Most of the material in this section is based on Stoyan, Kendall and Mecke [21] and Diggle [2] which are warmly recommended as starting points in this subject. Other recommended books are Illian *et al* [3], Møller and Waagepetersen [14] and Barndorff-Nielsen *et al* (eds.) [20].

2.1 Point Processes

2.1.1 Definitions

A point process, denoted by Φ, models a random set of points in some metric space. We will restrict our attention to $\mathbb{R}^d$. Formally, Φ is a measurable mapping from a probability space $(\Omega, \mathcal{F}, \mathbb{P})$ into a measurable space $[\mathbb{S}, \mathcal{S}]$, where $\mathbb{S}$ is the family of all *locally finite* and *simple* set of points, φ, in $\mathbb{R}^d$. A set being simple means that no two points are equal and it being locally finite means that each bounded subset of $\mathbb{R}^d$ contains only a finite number of points. The σ-algebra $\mathcal{S}$ is the smallest σ-algebra making all the mappings $\varphi \mapsto \varphi(B)$ measurable, for Borel sets B, where $\varphi(B)$ is the number of points of φ that lie in B. A point process can be regarded as either a random set of points or a *random measure*, counting the number of points in a region. We will use the notation Φ in both cases. These two different ways of viewing a point process lead to two different types of events. In the first case one looks at events of the type $\{\Phi \cap B = \emptyset\}$, the event that there are no points of Φ in B, while in the second $\{\Phi(B) = n\}$, the event that there are n points of Φ in the set B. A point process Φ induces a distribution P, defined by

$$P(Y) = \mathbb{P}\{\omega \in \Omega : \Phi(\omega) \in Y\}, \ \text{ for } Y \in \mathcal{S}.$$

The point process is said to be *stationary*, i.e. translation-invariant, if

$$P(S) = \mathbb{P}\{\Phi \in S\} = \mathbb{P}\{\Phi_{\mathbf{x}} \in S\} = P(S_{-\mathbf{x}}),$$

and *isotropic*, i.e. rotation-invariant, if

$$\mathbb{P}\{\Phi \in S\} = \mathbb{P}\{\mathbf{r}\Phi \in S\},$$

for $S \in \mathcal{S}$. Here $\Phi_{\mathbf{x}} = \{\mathbf{y} \in \mathbb{R}^2 : \mathbf{y} - \mathbf{x} \in \Phi\}$ and $\mathbf{r}\Phi = \{\mathbf{y} \in \mathbb{R}^2 : \mathbf{r}^{-1}\mathbf{y} \in \Phi\}$ for a rotation $\mathbf{r}$ about the origin. If Φ is both stationary and isotropic, Φ is said to be *motion-invariant.*

The intensity measure is defined as $\Lambda(B) = \mathbb{E}[\Phi(B)]$, for a Borel-set B. If Φ is stationary, then $\Lambda(B) = \lambda\nu_d(B)$, where λ is a non-negative constant and ν_d is the d-dimensional Lebesgue measure. The constant λ can be interpreted as the mean number of points per unit volume, and is called the *intensity*. The following theorem is fundamental in the theory of point processes.

Theorem 1. ***(Campbell Theorem)*** *Let Φ be a point process with intensity measure Λ. Then for any measurable function $f : \mathbb{R}^d \to \mathbb{R}^+$, we have that*

$$\mathbb{E}\left[\sum_{\mathbf{x}\in\Phi} f(\mathbf{x})\right] = \int f(\mathbf{x})\Lambda(d\mathbf{x}) = \lambda \int f(\mathbf{x})d\mathbf{x},$$

where the last equality holds only if the point process is stationary with intensity λ.

Two important distribution functions are the *spherical contact distribution function* (alt. the *empty space distribution function*) defined as

$$H(r) = 1 - \mathbb{P}\{\Phi(b(o,r)) = 0\}, \text{ for } r \geq 0,$$

where o denotes the origin and $b(o,r)$ denotes a ball centered at the origin with radius r, and the *nearest neighbor distance distribution function* defined by

$$D(r) = 1 - \mathbb{P}\{\Phi(b(o,r)) = 1|\, o \in \Phi\}.$$

The interpretation of H is that it is the distribution function of the distance from a "random" point in $\mathbb{R}^d$ to the nearest point of Φ. The function $D(r)$ can be interpreted as the distribution function of the distance from a *typical* point of the process to its nearest neighbor.

For a point process, there are analogous concepts of moments as for random variables, but in this setting we regard *moment measures*. In the following, let $f : \mathbb{R}^d \to \mathbb{R}^+$ be an arbitrary measurable function. The n^{th} *order moment measure* of Φ is the measure $\mu^{(n)}$, defined on $\mathcal{B}^{nd}$ by

$$\mathbb{E}\left[\sum_{\mathbf{x}_1,\ldots,\mathbf{x}_n\in\Phi} f(\mathbf{x}_1,...,\mathbf{x}_n)\right] = \int_{\mathbb{R}^{nd}} f(\mathbf{x}_1,...,\mathbf{x}_n)\mu^{(n)}(d(\mathbf{x}_1,...,\mathbf{x}_n)),$$

where $\mathcal{B}$ denotes the Borel σ-algebra. This implies that

$$\mu^{(n)}(B_1 \times ... \times B_n) = \mathbb{E}\left[\Phi(B_1)...\Phi(B_n)\right],$$

i.e. the expected number of n-tuples where the first point is in B_1, the second in B_2,..., and the n^{th} in B_n. The n^{th} *order factorial moment measure* of Φ is the measure $\alpha^{(n)}$, defined on $\mathcal{B}^{nd}$ by

$$\mathbb{E}\left[\sum_{\substack{\mathbf{x}_1,...,\mathbf{x}_n\in\Phi\\ \mathbf{x}_i\neq\mathbf{x}_j,\ i,j=1,...,n}} f(\mathbf{x}_1,...,\mathbf{x}_n)\right] = \int_{\mathbb{R}^{nd}} f(\mathbf{x}_1,...,\mathbf{x}_n)\alpha^{(n)}(d(\mathbf{x}_1,...,\mathbf{x}_n)),$$

i.e. only "real" n-tuples (without multiple points) are counted. If $\alpha^{(n)}$ is locally finite and absolutely continuous w.r.t. the nd-dimensional Lebesgue measure, then there exists a density $\varrho^{(n)}(\mathbf{x}_1,...,\mathbf{x}_n)$, called the n^{th}*order product density*, s.t.

$$\mathbb{E}\left[\sum_{\substack{\mathbf{x}_1,...,\mathbf{x}_n\in\Phi\\ \mathbf{x}_i\neq\mathbf{x}_j}} f(\mathbf{x}_1,...,\mathbf{x}_n)\right] = \int_{\mathbb{R}^{nd}} f(\mathbf{x}_1,...,\mathbf{x}_n)\varrho^{(n)}(\mathbf{x}_1,...,\mathbf{x}_n)d\mathbf{x}_1...d\mathbf{x}_n.$$

The n^{th} *order product density* has the following interpretation: if $Z_1,...,Z_n$ are pairwise disjoint spheres with centers $\mathbf{x}_1,...,\mathbf{x}_n$ and infinitesimal volumes $dV_1,...,dV_n$, then $\varrho^{(n)}(\mathbf{x}_1,...,\mathbf{x}_n)dV_1,...,dV_n$ is the probability that there is a point of Φ in each of the spheres $Z_1,...,Z_n$. If Φ is motion-invariant, then $\varrho^{(2)}$ only depends on the distance between $\mathbf{x}_1$ and $\mathbf{x}_2$, i.e.

$$\varrho^{(2)}(\mathbf{x}_1,\mathbf{x}_2) = \varrho^{(2)}(r),$$

where $r = |\mathbf{x}_1 - \mathbf{x}_2|$. We can define two other functions characterizing the second order properties of a point process via the second order product density. These are the *K function*

$$K(r) = \frac{d\, b_d}{\lambda^2}\int_0^r t^{d-1}\varrho^{(2)}(t)dt, \tag{2.1.1}$$

where b_d denotes the volume of the d-dimensional unit ball, and the *pair-correlation function*

$$g(r) = \frac{\varrho^{(2)}(r)}{\lambda^2} = \frac{1}{d\, b_d}\frac{dK(r)}{dr}. \tag{2.1.2}$$

The K-function is proportional to the expected number of further points of the process within distance r of a randomly chosen process point, and g is essentially the derivative of K. Often a variance-stabilized version of the K-function is used, see Besag and Diggle [1], namely

$$L(r) = \left(\frac{K(r)}{b_d}\right)^{\frac{1}{d}}.$$

The K-function can be defined using the *reduced Palm distribution* (at the point $\mathbf{x}$),

$$P^{!}_{\mathbf{x}}(Y) = \mathbb{P}\{\Phi \setminus \{\mathbf{x}\} \in Y \,|\, \mathbf{x} \in \Phi\}. \tag{2.1.3}$$

Then

$$\lambda K(r) = \mathbb{E}^{!}_{o}[\Phi(b(o,r))],$$

where $\mathbb{E}^{!}_{o}$ denotes expectation w.r.t. the reduced palm distribution (at the origin). The *Palm distribution* is defined as

$$P_{\mathbf{x}}(Y) = \mathbb{P}\{\Phi \in Y \,|\, \mathbf{x} \in \Phi\}. \tag{2.1.4}$$

One has to keep in mind that the events that we condition on have probability zero so these distributions have to be carefully defined. For a more rigorous definition of the Palm distributions see e.g. Stoyan, Kendall and Mecke [21].

2.1.2 Point Process Models

In this section we give a short introduction the point process models used in this thesis.

Poisson Process

A point process Φ with intensity measure Λ is called a Poisson process if

1. *The number of points, $\Phi(B)$, in a bounded Borel set B has Poisson distribution with mean $\Lambda(B)$.*
2. *If A and B are disjoint Borel sets, then $\Phi(A)$ and $\Phi(B)$ are independent.*

In this general setting Φ is not stationary. Often Λ is assumed to have a density with respect to the Lebesgue measure, i.e. $\Lambda(B) = \int_B \lambda(\mathbf{x})d\mathbf{x}$, for Borel sets B. The density $\lambda(\cdot)$ is called the *intensity function*. Further, if $\lambda(\mathbf{x}) = \lambda$, then Φ is stationary. It follows from conditions 1 and 2 above that conditioned on the number of points in a set S, the positions of the points are independent and uniformly distributed in S. The Poisson process setting is often referred to as *complete spatial randomness* (CSR) and serves as a baseline model.

It can be shown that for a Poisson process the reduced Palm distribution coincides with the distribution of the process P. It can further be shown that the Poisson process is characterized by this, see e.g. Jagers [4]. This implies that

$$\begin{aligned}\lambda K(r) &= \mathbb{E}^!_o[\Phi(b(o,r))] = \int \varphi(b(o,r))P^!_o(d\varphi) = \int \varphi(b(o,r))P(d\varphi) \\ &= \mathbb{E}[\Phi(b(o,r))] = \lambda v_d(b(o,r)) = \lambda b_d r^d,\end{aligned}$$

i.e. $K(r) = b_d r^d$. Furthermore, we obtain that $g(r) = 1$, $\varrho^{(2)}(r) = \lambda^2$ and $L(r) = r$ for a Poisson process.

Cox Processes

A further generalization of the Poisson process leads to Cox processes (or *Doubly Stochastic Poisson Processes*). Here Λ is a random measure and Φ is a Poisson process conditionally on Λ. One basic example of a Cox process would be to let the intensity measure (or *driving random measure*) be $\Lambda = I\nu_d$, for a non-negative random variable I. A more interesting example of a Cox process is the *log Gaussian Cox process* [12], where $\log \Lambda$ is a Gaussian random field. If the random field is stationary then the first and second-order characteristics of the Cox process are funtions of the mean and covariance function of the random field.

Neyman-Scott process
A well known Cox process is the Neyman-Scott process which is constructed as follows. First, *parent points* are scattered according to a stationary Poisson process, and then, a random number of *daughter points* are scattered independently and identically distributed around each parent point. The parent points are then removed, so one only observes the daughter points. The resulting process is stationary if the daughter process is stationary and if the distribution that governs the scattering of daughter points in addition is isotropic then the process is motion-invariant. It can be shown that the intensity of the process is $\lambda = \lambda_p \overline{c}$, where λ_p is the intensity of the parent process and $\overline{c}$ is the mean number of daughter points per parent. The Neyman-Scott process is an example of a *shot noise Cox process* [13].

Random set generated Cox process
If we define the driving random measure as $\Lambda(\mathbf{x}) = \lambda_1 \mathbf{1}_\Theta(\mathbf{x}) + \lambda_2 \mathbf{1}_{\Theta^c}(\mathbf{x})$, where Θ is a random closed set, see e.g. [21] the resulting process is known as a random set generated Cox process (RSGCP). Conditionally on Θ the process is a Poisson process of two different intensities, one inside Θ and another outside of Θ. This type of model

was introduced by Penttinen and Niemi [17], motivated by an application in forestry. The random set Θ is thought of as to represent an underlying heterogeneity. If Θ is stationary and isotropic then so is the Cox process, and the intensity and second-order characteristics are functions of the *volume fraction*, p and *covariance*, $C(r)$ of the random set. These quantities are defined as $p = P(o \in \Theta)$ and $C(r) = P(o \in \Theta,\, \mathbf{r} \in \Theta)$, $r = |\mathbf{r}|$, respectively.

Hard-Core Processes

Poisson processes can also be used as starting processes when so-called hard-core processes are constructed. In this type of process any point cannot lie closer than a distance $h > 0$ to the other points of the process. Two examples of hard-core processes are the *Matérn I* and *II* hard-core processes [9]. In Matérn I only the points having the nearest neighbor farther away than h are retained. Matérn II is a hard-core process produced by a dependent thinning of a Poisson process Φ. Each point is given a mark independently from the $\mathrm{U}(0, 1)$-distribution. A point $\mathbf{x} \in \Phi$ is retained if there are no points in $b(\mathbf{x}, h)$ having a longer mark than the point $\mathbf{x}$ has. A generalization of Matérns processes can be found in Månsson and Rudemo [15].

2.1.3 Estimation

When analysing point patterns, Φ observed in a bounded window $W \subseteq \mathbb{R}^2$, the analysis often starts by estimating some first and second-order characteristics. In this section we discuss estimation of intensity and the second-order characteristics K and $\varrho^{(2)}$. There are numerous other estimation techniques than the ones presented here, see e.g. [21]. The intensity, λ, can be estimated by

$$\hat{\lambda} = \frac{\Phi(W)}{|W|},$$

where $|W|$ denotes the area of W. To estimate the K-function, we will use the estimator introduced by Ripley [18] namely

$$\hat{K}(r) = \frac{|W|}{\Phi(W)^2} \sum_{x,y \in \Phi \cap W} k(x, y) \mathbf{1}_{\{0 < |x-y| \leq r\}}, \tag{2.1.5}$$

where the weights $k(x, y)$ are defined as $\frac{2\pi}{\alpha_{xy}}$. Here α_{xy} denotes the sum of all angles of the arcs lying in W of a circle with centre x and radius $|x - y|$. If $\alpha_{xy} = 2\pi$, the circle lies completely in W and point gets weight 1. The points for which the circle lies partly outside W have weights that are greater than 1. The product density and the pair-correlation function can be estimated using the edge corrected density estimator by Fiksel (see [5])

$$\hat{\varrho}^{(2)}(r) = \frac{1}{2\pi r} \sum_{x,y \in \Phi \cap W} \frac{c(|x - y| - r)}{|W_x \cap W_y|}, \tag{2.1.6}$$

where $c(\cdot)$ is a kernel and $W_x = \{z \in \mathbb{R}^2 \ : \ z - x \in W\}$. Fiksel suggests the Epanechninov kernel $c(x) = \frac{3}{4}\left(1 - x^2\right) \mathbf{1}_{\{|x|<1\}}$ and bandwidth $0.1\sqrt{\frac{5}{\lambda}}$.

One of the initial steps of analyzing spatial point pattern data is to test whether they can be regarded as a realization of a Poisson process or not. As seen above, for a Poisson process $K(r) = \pi r^2$ and $\varrho^{(2)}(r) = \lambda^2$. If $\hat{K}(r)$ or $\hat{\varrho^{(2)}}(r)$ deviate too much from what they should be under CSR then one should reject the hypothesis that the observed pattern is generated by a Poisson process. Further, $\hat{K}(r) > \pi r^2$ indicates clustering and $\hat{K}(r) < \pi r^2$ indicates regularity.

2.2 Fiber Processes in the Plane

2.2.1 Definitions

A fiber process in the plane models a random collection of curves in $\mathbb{R}^2$. A *fiber* is a sufficiently smooth simple curve, of finite length, in the plane. That is, the set $\{\gamma(t) : t \in [0, 1]\}$ is called a fiber if $\gamma \subset \mathbb{R}^2$, is the image of a curve $\gamma(t) = (\gamma_1(t), \gamma_2(t))$, s.t:

1. $\gamma : [0, 1] \to \mathbb{R}^2 \in \mathcal{C}^1$,
2. $|\gamma'(t)|^2 = \gamma_1'(t)^2 + \gamma_2'(t)^2 > 0, \forall\, t$
3. γ is one-to-one, i.e. the fiber does not intersect itself.

Further, γ also denotes a length measure, defined as

$$\gamma(B) = \int_0^1 \mathbf{1}_B(\gamma(t))\sqrt{\gamma_1'(t)^2 + \gamma_2'(t)^2}dt, \;\; B \in \mathcal{B}^2.$$

That is, $\gamma(B)$ is the length of the part of the fiber γ lying in B. A *fiber system*, ψ, is a closed subset of $\mathbb{R}^2$ which can be represented as a union of at most countably many fibers γ_i. Furthermore, any compact set is intersected by at most a finite number of fibers and distinct fibers can only have end-points in common. The length measure, corresponding to ψ is defined in terms of the measures γ_i by

$$\psi(B) = \sum_{\gamma_i \in \psi} \gamma_i(B).$$

The definitions above prevent fiber systems from having locally dense accumulations of self-intersection points. The locally finite and smoothness conditions ensure that the measure ψ is locally finite.

The family of all planar fiber systems is denoted by $\mathbb{F}$ and the corresponding σ-algebra by $\mathcal{F}$, where $\mathcal{F}$ is generated by sets of the form

$$\{\psi \in \mathbb{F} \,:\, \psi(B) < x\},$$

for $B \in \mathcal{B}^2$ and $x \in \mathbb{R}$. A (planar) *fiber process*, Ψ, is a random variable with values in $[\mathbb{F}, \mathcal{F}]$. The *distribution* of the fiber process is the measure P generated by Ψ, on $[\mathbb{F}, \mathcal{F}]$. There are analogous definitions of stationarity and isotropy as in the point process case.

Moment Measures

The *intensity measure*, Λ_Ψ, of Ψ is defined by

$$\Lambda_\Psi(B) = \mathbb{E}[\Psi(B)], \;\; B \in \mathcal{B}^2,$$

and is the expected total fiber length in the set B. If Ψ is stationary, we have that

$$\mathbb{E}[\Psi_x(B)] = \mathbb{E}[\Psi(B_x)],$$

and

$$\Lambda_\Psi = \lambda_L \nu_2,$$

where $\lambda_L \in [0, \infty]$ is the mean fiber length per unit area.

The *second moment measure*, $\mu_\Psi^{(2)}$, of Ψ is given by

$$\mu_\Psi^{(2)}(B_1 \times B_2) = \mathbb{E}[\Psi(B_1)\Psi(B_2)], \quad B_1, B_2 \in \mathcal{B}^2.$$

For a stationary fiber process, it can be expressed by

$$\mu_\Psi^{(2)}(B_1 \times B_2) = \lambda_L^2 \int_{\mathbb{R}^2} \int_{\mathbb{R}^2} \mathbf{1}_{B_1}(x)\mathbf{1}_{B_2}(x+h)dx\mathcal{K}_f(dh),$$

for $B_1, B_2 \in \mathcal{B}^2$, where $\mathcal{K}_f$ is the *reduced second moment measure* of Ψ. In the case of stationarity and isotropy it is enough to consider the *reduced second moment function* K_f, also referred to as the *fiber K-function*, defined as

$$K_f(r) = \mathcal{K}_f(b(o,r)), \text{ for } r \geq 0, \tag{2.2.1}$$

where $b(o,r)$ denotes a circle with center o and radius r. That is, $\lambda_L K_f(r)$ is the expected fiber length within distance r of a randomly chosen fiber point.

2.2.2 Estimation

The following edge corrected estimator of $\lambda_L K_f$ is used, see Stoyan, Kendall and Mecke [21]:

$$\kappa(r) = \frac{1}{\#\{\Psi \cap T\}} \sum_{x \in \Psi \cap T} k(x,r)\Psi(S(x,r,W)). \tag{2.2.2}$$

Here T is a test system. In our case T consists of parallel lines, e.g. the pixels in a digital image. Furthermore,

$$k(x,r) = \frac{2\pi}{\alpha_{x,r}},$$

where $\alpha_{x,r}$ is the sum of all the angles of the arcs in W of a circle with center x and radius r, the same as in the case of Ripley's estimator of the K-function. In Figure 2.1 $\alpha_{x,r} = 2\pi - (\beta + \lambda)$. Further, $S(x,r,W)$ denotes the regions of a circle, centered at x with radius r, with the whole arc lying in W. $S(x,r,W)$ is the marked area of the circle in Figure 2.1. This estimator is unbiased (no results of the variance are known).

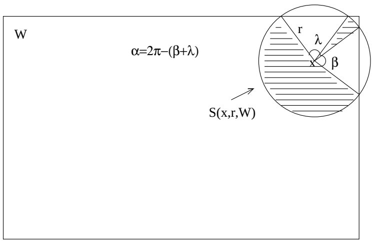

Figure 2.1: *Graphical explanation of* $S(x, r, W)$ *and* $\alpha_{x,r}$.

The intensity, λ_L can be estimated by:

$$\hat{\lambda}_L = \frac{\Psi(W)}{|W|}. \tag{2.2.3}$$

The estimator of $K_f(r)$ then becomes:

$$\hat{K}_f(r) = \frac{\kappa(r)}{\hat{\lambda}_L}.$$

2.3 Poisson-Voronoi Tessellations and the Stienen model

Let Φ be a homogenous Poisson process in $\mathbb{R}^d$ with intensity $\lambda \in (0, \infty)$. Now, let

$$\mathcal{V} = \{\, \mathcal{V}_{\mathbf{x}} \,:\, \mathbf{x} \in \Phi \,\},$$

for

$$\mathcal{V}_{\mathbf{x}} = \{\mathbf{y} \in \mathbb{R}^d \,:\, ||\mathbf{y} - \mathbf{x}|| \leq ||\mathbf{y} - \mathbf{z}||,\, \mathbf{z} \in \Phi\}.$$

Then, $\mathcal{V}$ is known as a *Poisson-Voronoi tessellation*. The points in Φ are called generators (or nuclei) of $\mathcal{V}$. The Poisson-Voronoi tessellation was introduced by Meijering [10]. For a more in-depth view on Poisson-Voronoi Tessellations, Møller [11] and Okabe *et al.* [16] are good starting points.

Around each point $\mathbf{x} \in \Phi$, let us now place a sphere with diameter being equal to the distance to the nearest neighbor of $\mathbf{x}$. Another way of looking at this is to attach the following mark to each point of Φ,

$$R_{\mathbf{x}} = \min_{\mathbf{y}\in\Phi\,:\,\mathbf{y}\neq\mathbf{x}} \{||\mathbf{x}-\mathbf{y}||/2\}.$$

Then, the random closed set

$$\mathcal{S} = \bigcup_{\mathbf{x}\in\Phi_b} b(\mathbf{x}, R_{\mathbf{x}}), \tag{2.3.1}$$

is called the Stienen model and was introduced by Stienen [19] motivated by an application in material science. A plot of both the tessellation and the Stienen model generated from the same realization of a Poisson process can be seen in Figure 2.2.

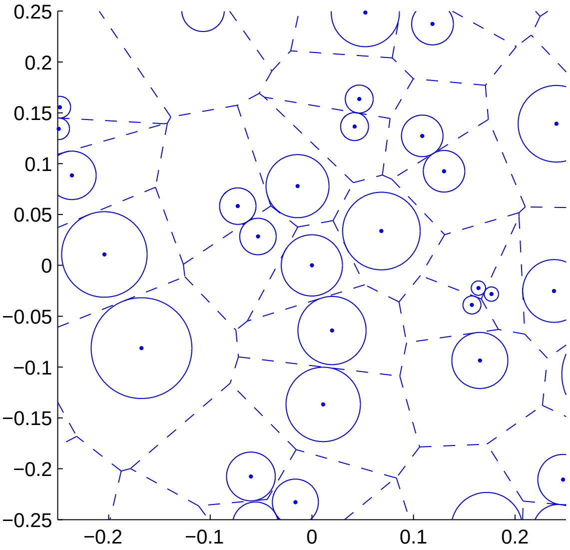

Figure 2.2: Realization of a Poisson-Voronoi tessellation and the Stienen model.

Chapter 3

Summary of Papers

3.1 Paper I: Second-Order Spatial Analysis of Epidermal Nerve Fibers

This paper deals with exploratory analysis of the ENF data. The tools used are second order characteristics of both planar point and fiber processes and the main goal is to detect differences between spatial patterns coming from diabetic and non-diabetic subjects. We use both the L-function and the pair-correlation function to compare the nerve trunk patterns (without the fibers) from the non-diseased and the three diabetic groups. Furthermore, we incorporate the whole fibre structure into the analysis. To be able to compare the fiber patterns, we first need to apply some image analysis tools in order to ”clean” the data. Then, the fiber K-function is used. Since some of the fibres die due to diabetes, the patterns coming from diabetic subjects, have less nerve points than the non-diabetic pattern. Since second-order characteristics are invariant under random thinning these are used to test if the ”diabetic patterns” are random thinnings of normal patterns. Monte Carlo methods are used in order to test whether the spatial patterns of diseased and non-diseased patients differ.

Since we have only a very limited amount of data, we can not draw any general conclusion from this analysis. However, we introduce some ideas that can be used and will serve as an initial step towards larger studies.

3.2 Paper II: A marked Poisson process induced by a random set generated Cox process

In this paper we suggest a set of point process models which can work as starting points in modelling epidermal nerve fiber patterns. First, some simplifications of the complex patterns are made, for example replacing the irregular paths of the fibers by straight lines. This can be justified by the fact that only the nerve endings transmit heat, pain etc. and therefore, the distances between endings and the corresponding trunks are most important. The main idea is that ENFs will more or less try to uniformly cover the body. This means that two nerve trunks lying close to each other are not likely to grow branches into each other, they will rather extend branches into open spaces. This basic feature is captured by the following model. We regard a marked point process model based on a bivariate point processes consisting of two stationary point processes made up of bases and endings, respectively. The idea is to have a branch system produced by connecting all points in the ending process to their respective closest neighbor of the base. This will make branches ”grow” into open spaces and furthermore, branches will not cross. The base process, Φ_b, is a homogenous poisson process and the ending process is a random set generated Cox process (RSGCP) [17]. The two main features this model captures are that endings are more probable to be in regions further away from the closest neighboring base points and Θ represents some underlying heterogeneity. In the ENF application this would be in the epidermis.

The characteristics we are mainly interested in are number of branches per base, branch lengths (individual and total per base) and angles between the segment joining bases and their associated endings and the x-axis. We obtain integral expressions for mean, variance and covariance of an additive functional for both a general Θ independent of Φ_b and also in the case when Θ is the Stienen model generated by Φ_b. This construction induces a hierarchical dependence between Φ_e and Φ_b and allows for different intensities in different regions of the Voronoi cells, based on the distances between the generators of the tessellation.

3.3 Paper III: Development and evaluation of spatial point process models of epidermal nerve fibers

We define two stochastic models describing the growth of branching systems, motivated by the growth and development of epidermal nerve fibers (ENFs) in human skin.

The models derive from two point processes, (Φ_b, Φ_e), describing the base and ending points of the fibers. Each point of Φ_e (the end point process) is connected to a unique point in Φ_b (the base point process). In the first model, both Φ_e and Φ_b are Poisson processes, yielding general baseline results. In the second model, we model the branching structure more directly by defining Φ_b as a general point process and Φ_e as a cluster process conditioned on the realization of Φ_b as its parent points. In both cases, we derive distributional properties for observable quantities of direct interest to neurologists such as the number, direction, and length of fibers for any particular base, conditional on the number and location of the other bases. We illustrate both models by fitting them to data from skin biopsy images of ENFs and provide inference regarding physiological properties of ENF growth.

3.4 Paper IV: On the Correlation Between the Volumes of the Typical Poisson-Voronoi Cell and the Typical Stienen Sphere

In this paper we regard a tessellation $\mathcal{V}$ generated by a homogenous Poisson process Φ in $\mathbb{R}^d$, and further the random set of spheres with centers being the points in Φ and having radius half the distance to the closest other point in Φ. We denote the typical cell and the typical sphere by $\mathcal{V}_o$ and $\mathcal{S}_o$, respectively, and the interest lies in the correlation between $\nu_d(\mathcal{V}_o)$ and $\nu_d(\mathcal{S}_o)$, where ν_d is the d-dimensional Lebesgue measure. Intuitively it feels as though this correlation should be strictly positive, and even close to one. Still, one must keep in mind that small spheres are often associated with large cells. That is, if two generators are close the corresponding cells need not to be small, see Figure 2.2. On the real line $\text{corr}(\nu_1(\mathcal{V}_o), \nu_1(\mathcal{S}_o)) = \frac{1}{\sqrt{2}}$, and for $d \geq 2$ we present an integral formula for $\text{corr}(\nu_d(\mathcal{V}_o), \nu_d(\mathcal{S}_o))$, from which it is possible to obtain numerical estimates for arbitrary dimensions. Furthermore, we obtain an upper bound on the correlation implying that $\lim_{d\to\infty} \text{corr}(\nu_d(\mathcal{V}_o), \nu_d(\mathcal{S}_o)) = 0$ and the numerical estimates suggests that the sequence decreases monotonically.

Bibliography

[1] BESAG, J. AND DIGGLE, P.J. (1977) *Simple Monte Carlo tests for spatial patterns*, Appl. Stat., **26**, 327-333.

[2] DIGGLE, P. (2003) *Statistical Analysis of Spatial Point Patterns, 2ed*, Arnold.

[3] ILLIAN, J., PENTTINEN, A., STOYAN, H. AND STOYAN, D. (2008) *Statistical Analysis and Modelling of Spatial Point Pattern*, John Wiley & Sons.

[4] JAGERS, P. (1973) *On Palm probabilities*, Probab. Theory Relat. Fields, **26**, 17-32.

[5] FIKSEL, T. (1988) *Edge-corrected density estimators for point processes*, Statistics, **19**, 67-75.

[6] FOSS, S. AND ZUYEV, S. (1996) *On a Voronoi Aggregative Process Related to a Bivariate Poisson Process*, Adv. Appl. Prob., 28, 965-981.

[7] KENNEDY, W.R., AND WENDELSCHAFER-CRABB, G. (1993) *The innervation of human epidermis*, Journal of the Neurological Sciences **115**, 184-190.

[8] KENNEDY, W.R., WENDELSCHAFER-CRABB, G. AND JOHNSON, T. (1996) *Quantitation of epidermal nerves in diabetic neuropathy*, Neurology, **47**, 1042-1448.

[9] MATÉRN, B. (1960) *Spatial Variation*, Meddelanden från Statens Skogsforskningsinstitut, **49**(5), 1-144.

[10] MEIJERING, J.L. (1953) *Interface area, edge length and number of vertices in crystal aggregates with random nucleation*, Philips Res. Rep., **8**, 270-290.

[11] MØLLER, J. (1994) *Lectures on Random Voronoi Tessellations*, Springer-Verlag, New-York.

[12] MØLLER, J. SYVERSVEEN, A.R. AND WAAGEPETERSEN, R.P. (1998) *Log Gaussian Cox processes*. Scand. Journal. of Stat. **25**, 451-482.

[13] MØLLER, J. (2003) *Shot noise Cox processes*, Adv. in Appl. Prob., **35**(3), 614-640.

[14] MØLLER, J. AND WAAGEPETERSEN R.P. (2004) *Statistical Inference and Simulation for Spatial Point Processes*, Chapman & Hall.

[15] MÅNSSON, M. AND RUDEMO, M. (2002) Random patterns of non-overlapping convex grains. Adv. Appl. Probability **34**, 718-738.

[16] OKABE, A., BOOTS, B., SUGIHARA, K. AND CHIU, S.N. (2000) *Spatial Tessellations, Concepts and Applications of Voronoi Diagrams, 2ed*, John Wiley & Sons.

[17] PENTTINEN, A. AND NIEMI, A. (2007) *On Statistical Inference for the Random Set Generated Cox Process with Set-marking*, Biometrical Journal **49**(2), 197-213.

[18] RIPLEY, B.D. (1976) *The Second-Order Analysis of Stationary Point Processes*, J. of Appl. Prob., **13**, 255-266.

[19] STIENEN, H. (1982) *Die Vergroeberung von Karbiden in reinen Eisen-Kohlenstoff Stahlen*, Dissertation, RWTH Aachen.

[20] BARNDORFF-NIELSEN, O.E., KENDAL, W.S. AND VAN LIESHOUT, M.N.M. (*eds.*) (2004) *Stochastic Geometry, Likelihood and Computation*, Chapman & Hall.

[21] STOYAN, D., KENDALL, W.S. AND MECKE, J. (1995) *Stochastic Geometry and its Applications, 2ed*, John Wiley & Sons.

[22] WANG, L., HILLIGES, M., JERNBERG, T., WIEGLEB-EDSTRÖM, D. AND JOHANSSON, O. (1990) *Protein gene product 9.5-immunoreactive nerve fibers and cells in human skin*, Cell and Tissue Research, **261**, 25–33.

Paper I

Second-order spatial analysis of epidermal nerve fibers

Lance A. Waller, Aila Särkkä, Viktor Olsbo,
Ioanna G. Panoutsopoulou, William R. Kennedy,
Gwen Wendelschafer-Crabb

Abstract

Recent breakthroughs in imaging of skin tissue reveal new details on the distribution of nerve fibers in the epidermis. Preliminary neurologic studies indicate qualitative differences in the spatial patterns of nerve fibers based on pathophysiologic conditions in the subjects. Of particular interest is the progress of diabetic neuropathy. It appears the spatial distribution of nerve fibers becomes more "clustered" as neuropathy advances. We consider two approaches to establish statistical inference relating to this observation. First, we view the set of locations where the nerves enter the epidermis from the dermis as a realization of a spatial point process. Secondly, we treat the set of fibers as a realization of a planar fiber process. In both cases we use estimated second-order properties of the observed data patterns to describe the degree and scale of clustering observed in the microscope images of blister biopsies. We illustrate the methods using confocal microscopy blister images taken from the thigh of one normal (disease-free) individual, and two images each taken from the thighs of subjects with mild, moderate, and severe diabetes and report measurable differences in the spatial patterns of nerve entry points/fibers associated with disease status.

KEYWORDS: Spatial point/fiber processes, pair-correlation function, K function, neurology, diabetic neuropathy

1 INTRODUCTION

Epidermal nerve fibers (ENFs) are thin, unmyelinated sensory nerve fibers that originate as single nerve fibers in dorsal root ganglia cells, travel through the dermis, extend into the epidermis, and terminate, with or without branching, at all levels of the epidermis from just above the dermal-epidermal interface "basement membrane" to near the surface of the skin[1]. While ENFs have been periodically observed for over 130 years, difficulties in staining and imaging led some to doubt their existence into the late 1980's. Expanding staining techniques proposed by Wang et al. [2], Kennedy and Wendelschafer-Crabb[1] conclusively established the existence of ENFs via confocal microscope studies. As an example, Figure 1 illustrates an image from a punch skin biopsy where the green filaments in the upper layer (epidermis) are ENFs as viewed from the side when the biopsy is sectioned perpendicular to the surface of the skin.

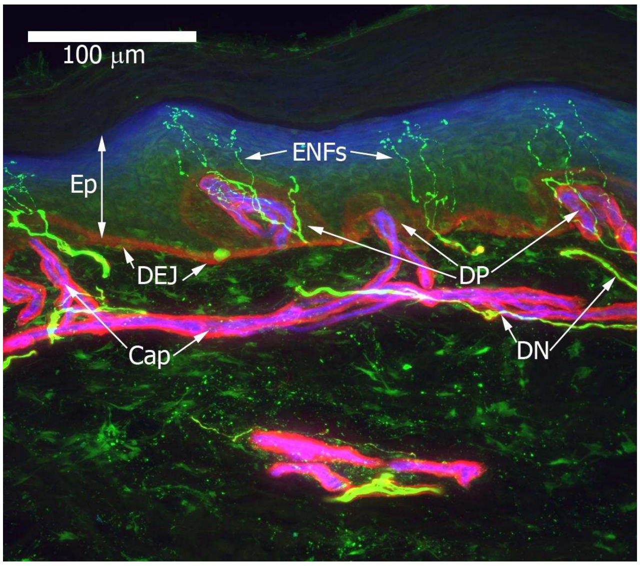

Figure 1: *A side view of nerve fibers and blood vessels in skin. Epidermal nerve fibers (ENFs - stained bright green with PGP 9.5 pan neuronal marker localization) arise from bundled fibers of dermal nerves (DN) that usually follow blood vessels and capillaries (Cap - colored magenta by combination of Ulex europaeus agglutinin I and type IV collagen staining) through the dermis to the superficial dermis where they form a horizontal plexus parallel to the dermal epidermal junction (DEJ - colored red by staining with type IV collagen). Individual ENFs penetrate the DEJ and extend into the epidermis (Ep - colored blue by reaction to Ulex europaeus agglutinin I). Nerve counts and distribution are determined based on the intersection of the nerve fibers with the DEJ. ENFs often arise from the top of dermal papilla (DP). This image is a composite made with a confocal microscope by combining 20 images collected at 2 μm increments through a thick triple-stained section. Colors only visible in the online version.*

Once methods for visualizing and identifying ENFs were established research quickly moved toward quantification of such fibers, especially to assess their potential diagnostic value. In particular, Kennedy et al. [3] report diminished numbers of ENFs per surface area in diabetic subjects, as well as reduced summed length of all ENFs per volume, that is, reduced "coverage" of the epidermis by ENFs. It is generally agreed that ENFs are counted where they penetrate the basement membrane to enter the epidermis [4]. Similarly, a diminished summed length of all ENFs can mean disappearing nerves or shortening of ENFs, although the former seems more likely and recent observations seem to suggest some lengthening of remaining ENFs during early nerve loss. That is, even though the *summed* total length of ENFs declines, *individual* ENFs may lengthen as the body tries to compensate for nerve loss.

Skin biopsy is a minimally invasive technique that allows quantitative assessment of the number and distribution of ENFs. "Punch" biopsies involve the removal of a 2-3 mm core of the epidermis and dermis, often from the hand, foot, calf, or thigh to detect the presence of peripheral neuropathy. Biopsies are cut into parallel sections and then immunostained with protein gene product (PGP) 9.5 to show nerves and with type IV collagen to stain the basement membranes at the dermal-epidermal junction and around blood vessels. Immunostained sections are imaged with a confocal microscope. This allows a view of nerve bundles rising from the dermis, then giving off single ENFs that extend through the basement membrane into the epidermis. Quantitative techniques are primarily limited to assessments of fiber linear density and length along a sampled section of the epidermis [5].

In contrast to the punch biopsy, Kennedy et al. [6] propose a less invasive technique for exploring ENFs based on a suction-induced blister (also 2-3 mm in diameter). During formation of the blister, ENFs are severed from their origin at the basement membrane level and remain in the epidermal blister roof. Then, instead of placing vertical slices on microscope slides, the epidermal blister roof is removed and flattened directly on a slide and immunostained, thus obtaining a "birds-eye view" of the ENF distribution[6] that is perpendicular to the view of the skin section. Suction blisters are more time-consuming to obtain than punch biopsies (requiring approximately 20-60 minutes) but the approach avoids the necessity of cutting, staining, and imaging multiple tissue sections. Recent results indicate that ENF densities (number of ENFs per unit area) observed from blister biopsies do not appear to systematically differ from punch biopsies, and normative density ranges for punch biopsy data ([4],[5]) appear to apply equally well to blister biopsy data[7].

Figure 2 illustrates a confocal image from a vertically sectioned suction blister. The ENFs are clearly visible in the epidermal blister roof (inset C). Blister fluid fills the space between the epidermis and the dermis. The separation plane is just above the basement membrane visible just below the fluid compartment. The near-by proximal stumps of some epidermal nerves are visible.

The dermal-epidemal junction undulates and dermal papilla (labeled DP in Figure 1) project into the epidermal space. Capillary loops and several dermal nerves reside within each papilla. It is worth noting that the basement membrane is closer to the surface (i.e. the epidermis is thinner) above the dermal papilla. The dermal papilla reflect variable thickness in the epidermal layer and this feature can appear as a cloudy background in blister images. ENFs often enter the dermis near dermal papilla resulting in possible spatial clustering of entry points for ENFs through the basement membrane, even in normal (non-diabetic) subjects, a feature that will impact our methodologic development below.

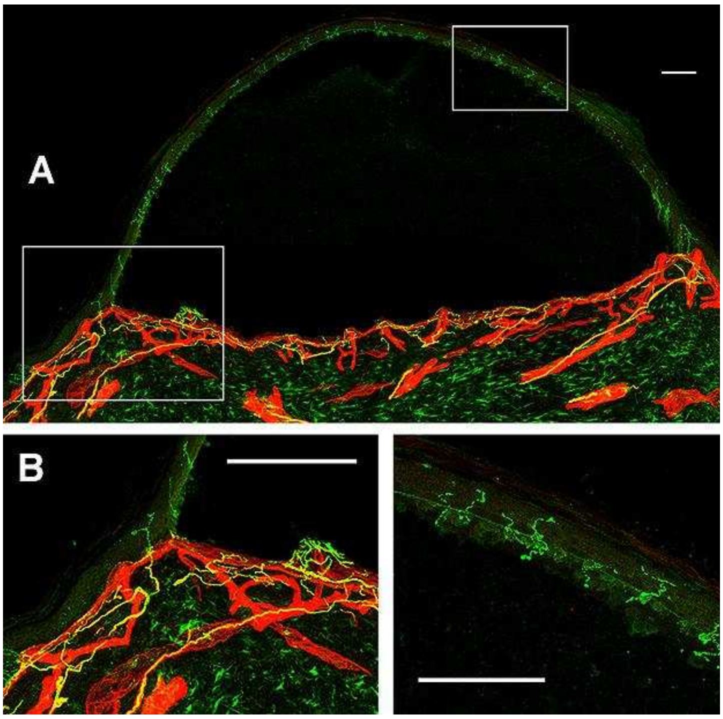

Figure 2: *Image of epidermal nerve fibers in blister roof. Rectangles in image A are enlarged in images B and C. The scale bar represents 200μm. (Image used with permission of the Kennedy Laboratory.)*

Our particular interest involves the spatial distribution of ENFs in the epidermis. Kennedy et al. [6] report that nerve fiber loss due to neuropathy does not seem to result in random removal of ENFs, rather the remaining nerves seem arranged in ”clusters” and exhibit some spatial pattern, perhaps secondary to collateral branching by the surviving nerve fibers. We seek to quantify this observation through statistical analysis of the spatial scale of clustering observed in blister images, and compare the scales observed for normal and neuropathic subjects, respectively. Such estimates may provide diagnostic statistical tools for determining early stages of neuropathy, based on a minimally invasive technique thereby allowing diagnosis early in the disease when neuropathy is most likely to respond to treatment.

Kennedy et al. [6] (p. 366) mention that ENFs from the symptomatic thigh of a subject with a lateral femoral cutaneous nerve disorder had a greater propensity to group in clusters than ENFs from the asymptomatic thigh, with intervening spaces sparsely innervated relative to ENFs of the normal thigh. A similar pattern was observed in diabetic subjects. Figure 3 illustrates the spatial distribution of ENFs from a portion of the blister roof taken from the thigh of a normal subject in the top image and from a subject with moderate diabetic neuropathy in the bottom image. The sample from the normal thigh appears to show a more regular pattern (with some clustering about dermal papilla) than that from the diabetic subject's thigh. It is important to note that most images (diabetic and non-diabetic) show evidence of some sort of clustering, the qualitative difference appears to be the spatial scale at which clustering occurs. Hence, our primary question of interest is: can we quantify differences in the spatial pattern of ENFs in nondiabetic subjects from the patterns in diabetic subjects, and identify the spatial scale where ENF patterns for diabetics are more clustered than those for nondiabetics?

We review basic definitions and second order properties of spatial point and fiber processes in Section 2, then apply these ideas to the ENF data in Section 3. The analyses allow quantification of the observations regarding changing patterns of clustering reported in Kennedy et al. [6] and offer new insight into the distances (spatial scales) at which measurable differences occur. Section 4 summarizes and discusses our results and offers directions for future analysis.

2 METHODS FOR SPATIAL POINT AND FIBER PROCESSES

2.1 Point Processes

Spatial point processes describe a family of stochastic process models where events generated by the model have an associated (random) location in space. Illian et al.[8], Diggle[9], Cressie[10] (Chapter 8), and Waller and Gotway[11] (Chapter 5) provide details regarding theory and applications from many diverse fields, e.g. forestry, astronomy, and cellular biology. We follow Diggle[9] and make a distinction between *points* and *events*. Points represent any location within the study area where the phenomenon

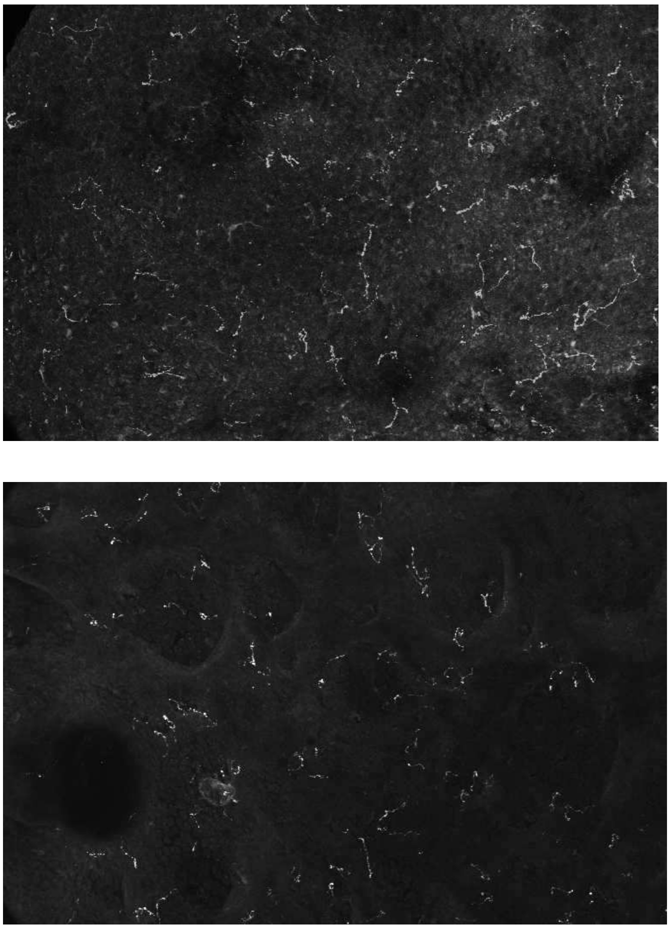

Figure 3: *Spatial distribution of nerve fibers (white) in a non-diabetic subject (top) and a subject with moderate diabetes (bottom).*

of interest *could* occur, events represent locations where this phenomenon *did* occur in a particular realization of the process. In our application, we define an event as the observed location of an ENF emergence from the basement membrane.

Our question of interest is whether or not the nerve fibers are significantly more “clustered” in diabetic subjects than in normal subjects, and, if so, at what spatial scale do these differences occur? Typically, one models spatial clustering as a departure from a model of spatial randomness defined by a spatial Poisson process[9]. Three primary features define a spatial Poisson process namely: (a) the number of events in non-overlapping regions are statistically independent, (b) for any region A,

$$\lim_{|A|\to 0} \frac{\text{Pr[exactly one event in } A]}{|A|} = \lambda > 0$$

where $|A|$ is the area of region A, and (c)

$$\lim_{|A|\to 0} \frac{\text{Pr[two or more events in } A]}{|A|} = 0.$$

Components (b) and (c) imply that the probability of a single event in a very small area is a constant (λ) independent of the region A, and that the probability of two or more events occurring in precisely the same location is zero. The quantity λ is the Poisson parameter, or the "intensity" of the process. If λ is constant across the region the Poisson process is homogeneous. When conditions (a)–(c) are met, the number of events in a region A is a Poisson random variable with mean $\lambda|A|$, and the events are uniformly located within A. By "uniformly" we mean that the locations of events are independent of the location of other events and equally likely in all locations. These properties are referred to as "complete spatial randomness" (CSR)[9].

Complete spatial randomness often serves as a boundary condition between processes that are more "clustered" than CSR, and processes that are more "regular" than CSR. Unfortunately, observed patterns do not always fall neatly into one of the three classes: clustered, CSR, regular. For example, consider a regular pattern of clusters where small clumps of events occur at regularly spaced locations, or clusters of a regular pattern where some regular pattern of events (e.g., the pattern of five pips on the side of a die) repeatedly occurs at clustered locations across the study area. In both examples, clustering exists at one spatial scale, regularity at another. Such examples appear in Reilly et al. [12] and Waller and Gotway [11] and illustrate the critical role played by spatial scale in describing observed patterns. This said, little appears in the statistical literature regarding direct estimates of spatial scale. This is not to say that existing methods ignore scale, but the issues of point and interval estimation of scale (which are very relevant to our application) have not been of primary interest in the analysis of spatial point patterns.

Many statistical tests of CSR appear in the literature (see Table 8.6 in Cressie [10]), and many are based on the distribution of two nearest neighbor distances: the distribution of distances from each event to its nearest neighboring event, or the distribution of distances from a randomly selected point to the nearest event. While revealing overall tendencies toward clustering or regularity, these nearest neighbor methods only consider the *nearest* distances, and do not directly tell us about the scale of clustering observed at a variety of distances in a particular data set. Furthermore, these methods examine behavior only at the "nearest neighbor" scale and cannot find clustering at one scale and regularity at another.

To address spatial scale, we consider Ripley's K function[13], a second order property of an observed point process defined as

$$K(h) = \lambda^{-1} E[\#\text{ of extra events within } h \text{ of a } \textit{randomly} \text{ chosen event}]\ ; h \geq 0.$$

Under CSR,

$$K_{CSR}(h) = \pi h^2 = \text{ area of circle radius } h \text{ around event,}$$

under regularity, $K(h)$ tends to be $< \pi h^2$, and under clustering, $K(h)$ tends to be $> \pi h^2$. Since $K(h)$ is a function of all interevent distances (not just the nearest neighbor distances), it is possible for a given realization to have, for example, $K(h) > \pi h^2, h < h^*$, and $K(h) < \pi h^2, h > h^*$ for some distance h^*. This would indicate that for distances below h^* events tend to be more clustered than expected under CSR, while for distances above h^* events tend to be more regularly distributed than under CSR. Hence, h^* is associated with the spatial scale of clustering found in the data.

It is worth mentioning that the intensity λ and K functions (first and second order properties of a spatial point process) do not together uniquely identify a spatial process. Baddeley and Silverman[14] provide an example of a process containing intermittent clustering that has intensity and K functions identical to those for CSR, so one needs to exercise caution in interpretation.

To aid in visualization, Besag[15] suggests a variance-stabilizing transformation of the K function, $L(h) = \{K(h)/\pi\}^{1/2}$ (the L function). The L function allows a more readily interpretable diagnostic plot, since we may plot h vs. $L(h) - h$ and compare the resulting curve to its expected value under CSR of zero for all h.

We estimate the K function using a standard edge-corrected approach[10], namely

$$\widehat{K}(h) = \frac{1}{N\widehat{\lambda}} \sum_{i=1}^{N} \sum_{j=1, i \neq j}^{N} w(\boldsymbol{s}_i, \boldsymbol{s}_j)^{-1} I(\|\boldsymbol{s}_i - \boldsymbol{s}_j\| \leq h), h > 0$$

where $\widehat{\lambda}$ denotes the estimated intensity, $\boldsymbol{s}_i$ denotes the location of the ith event ($i = 1, \ldots, N$), and $I(\cdot)$ the indicator function. The edge-correction weights, $w(\boldsymbol{s}_i, \boldsymbol{s}_j)$, are set equal to the proportion of the circumference of a circle centered at $\boldsymbol{s}_i$, passing through $\boldsymbol{s}_j$ that is within the study area. These weights, suggested by Ripley[16], define the proportion of points at distance $\|\boldsymbol{s}_i - \boldsymbol{s}_j\|$ from $\boldsymbol{s}_i$ at which events could be observed (i.e., are within the study area). The estimate assumes stationarity (constant intensity across the study area) and isotropy (rotation invariance), both of which are reasonable as starting points for our analysis. We use $\widehat{L} = \{\widehat{K}(h)/\pi\}^{1/2}$ as an estimate of the L function.

Diggle, Lange and Beneš[17] apply K functions to assess the distribution of pyramidal neurons in the brain, demonstrating the ability of estimated K functions to detect differences in patterns between control, schizo-affective, and schizophrenic subjects.

Inference is based primarily on Monte Carlo envelopes and bootstrapped hypothesis tests. In the analysis below, we use K functions not only to distinguish between diagnostic groups, but also to provide estimated ranges of the spatial scale of observed clustering. That is, while Diggle, Lange, and Beneš[17] seek inference on differences between K functions, we focus on inference about particular features observed within each K function.

Note that the K function is a *cumulative* function of distance as it measures the expected number of events up to a certain distance. In our application, we are interested in the clustering/regularity observed at a particular distance rather than the cumulative evidence for clustering/regularity observed up to that distance. Parallel to the roles of the cumulative hazard and hazard functions in survival analysis, some data analytic questions may be better answered by the derivative of the K function, rather than the K function itself. We consider the use of a scaled form of this derivative, termed the pair-correlation function g, defined as

$$g(h) = \frac{1}{2\pi h}\frac{dK(h)}{dh}. \tag{1}$$

The pair-correlation function provides a scaled measure of how likely two events are to occur at distance h of each other. Under CSR, $g(h)$ takes the value one. Values greater than one indicate clustering and values smaller than one regularity. As with the K (L) function, the pair-correlation function is a function of distance and may provide evidence for clustering or regularity at different spatial scales.

Estimation of $g(h)$ generally involves edge-corrected kernel estimators[18] [19]. Stoyan and Stoyan[20] outline the following estimation procedure for $g(h)$ based on isotropic spatial point processes. The pair-correlation function can be written as $g(h) = \lambda^2\rho(h)$, where ρ is called the second order product density. To estimate $\rho(r)$ we use the estimator

$$\hat{\rho}(r) = \frac{1}{\pi h}\sum_{i=1}^{N}\sum_{j=i+1}^{N}\frac{k(h-||x_i-x_j||)}{\nu(A_{x_i}\cap A_{x_j})}.$$

In the formula, $\nu(A)$ is the Lebesgue measure of the set A and $A_x = \{y : y = z + x, z \in A\}$ and $k(\cdot)$ is a kernel function. Following Stoyan and Stoyan[20] we use the Epanechnikov kernel function with bandwidth $\epsilon = \delta/\sqrt{\hat{\lambda}}$ with $\delta = 0.1 \cdot \sqrt{5}$ as suggested by Fiksel[21].

2.2 Fiber Processes

Spatial point processes allows us to study the spatial pattern of entry points for epidermal nerves. If the whole fiber pattern is of interest, as in our application, we may consider a generalization to spatial *fiber* processes. Briefly, a fiber process in the plane models a random collection of curves in $\mathbb{R}^2$. The curves (i.e. fibers) are supposed to be sufficiently smooth and of finite length. Distinct fibers have only end-points in common.

We can define an analogous of Ripley's K-function for fiber processes, namely

$$\lambda_L K_f(h) \quad = \quad \mathbb{E}[\text{fiber length, within distance } h \text{ of a randomly chosen fiber point}],$$

where λ_L is the mean fiber length per unit area. Unlike the point process case where we have a natural reference process (i.e., the Poisson process), no such process exists for fiber processes. However, as we will see below, we can compare the relative amount of clustering between two fiber patterns by using the fiber K function: the pattern whose fiber K function lies above the other represents clustered pattern of the two (for a given distance or set of distances).

Stoyan, Kendall & Mecke[19] suggest the following edge corrected estimator of $\lambda_L K$ (where A denotes the region of observation):

$$\kappa(h) = \frac{1}{\#\{\Phi_f \cap T\}} \sum_{x \in \Phi_f \cap T} k(x,h)\Phi_f(S(x,h,A)), \tag{2}$$

where

$$k(x,r) = \frac{\alpha_{x,h}}{2\pi},$$

and $\alpha_{x,r}$ denotes the sum of all the angles of the arcs in A of a circle with center x and radius h (i.e., $k(x,h)$ is the proportion of the circumference of a circle, centered at x with radius h, that lies within A). For example, in Figure **??** $\alpha_{x,h} = 2\pi - (\beta + \lambda)$. Further, $S(x,h,A)$ denotes the regions of a circle, centered at x with radius h, with the whole arc lying in A, illustrated by the marked area of the circle in Figure **??**. This estimator is unbiased but variance properties are currently unknown. If we estimate λ_L by:

$$\hat{\lambda}_L = \frac{\Phi_f(A)}{|A|}, \tag{3}$$

then the estimator of $K(h)$ becomes:

$$\hat{K}(h) = \frac{\kappa(h)}{\hat{\lambda}_L}. \tag{4}$$

3 APPLICATION TO THE NERVE FIBER DATA

3.1 Point Processes

We use the point and fiber process methods outlined above (pair-correlation and K functions) to explore the spatial distribution of the locations where ENFs enter the epidermis and of the fibers themselves, respectively, (from a set of seven images provided by the

Kennedy Laboratory, University of Minnesota. The confocal microscope images are available as digitized images with pixel size 0.8264 microns by 0.8264 microns. The confocal microscope images were acquired at 2 μm increments of depth throughout the blister (25-50 μm thick). The course of each ENF through the depth of the epidermis can be followed from image to image or as an object in a rendered volume.)

We focus on images taken from the thighs of non-diabetic controls and individuals in various stages of diabetic neuropathy classified as: mild, moderate, and severe based on epidermal nerve density. The pair of images in each disease class are from adjacent blisters on the same subject, providing some (preliminary) assessment of intra-individual variability in spatial patterns.

The current state of imaging the blister biopsies does not allow automated identification of the entry points for ENFs, the identification of these locations in each of seven images (one normal and two in each diabetes category) is done manually. We present the seven locational data sets in Figure 4. As the practice of imaging blister biopsies continues to improve, we expect more automatic identification of entry locations for future analyses.

Figure 5 illustrates the estimate of the variance-stabilized K function ($\widehat{L}$ function) analysis of the same images. The dashed black lines correspond to Monte Carlo "envelopes" corresponding to the 2.5th and 97.5th percentiles of $\widehat{L}$ at each distance, estimated from 500 independent simulations of CSR within the study area. The $\widehat{L}$ functions in Figure 5 indicate a fairly consistent "dip" observed at distances near 20 pixels (≈ 16.5 microns). This "dip" reflects regularity at short distances significantly increased over that expected under CSR (i.e., we observe more equal spacing at 20 pixels than expected under a CSR pattern). This is rather natural since each nerve has its own territory and therefore, two nerves (or nerve entry points) should not lie too close to each other.

Each plot in Figure 5 compares the $\widehat{L}$ plot based on the image from the thigh of the normal subject (same black line in all plots within a column) to a pair of images from a diabetic subject. The top, middle, and bottom rows involve comparisons with a mild, a moderate, and a severe diabetic subject, respectively. Many of the plots suggest some increased clustering in the diabetic subjects over that observed for the normal subject ($\widehat{L}$ based on the diabetic images lying above that based on the normal image), but all $\widehat{L}$ functions lie mostly within the (vertical) range expected under CSR. However, we stress that the research question of primary interest involves comparing the diseased patterns to the normal (non-diseased) pattern, not comparing any of the patterns to CSR.

Toward this goal, we consider a second approach more directly evaluating the observed patterns with respect to the observation of a tendency toward diminished numbers of ENFs with disease progression and the primary question of interest: are ENFs clustered differently in diseased subjects than in non-disease subjects? Specifically, we wish to compare the observed patterns from the diabetic subjects to that we would expect to observe if ENF entry points were removed at random from the normal pattern. In theory, such random "thinning" of the normal pattern will result in the same theoret-

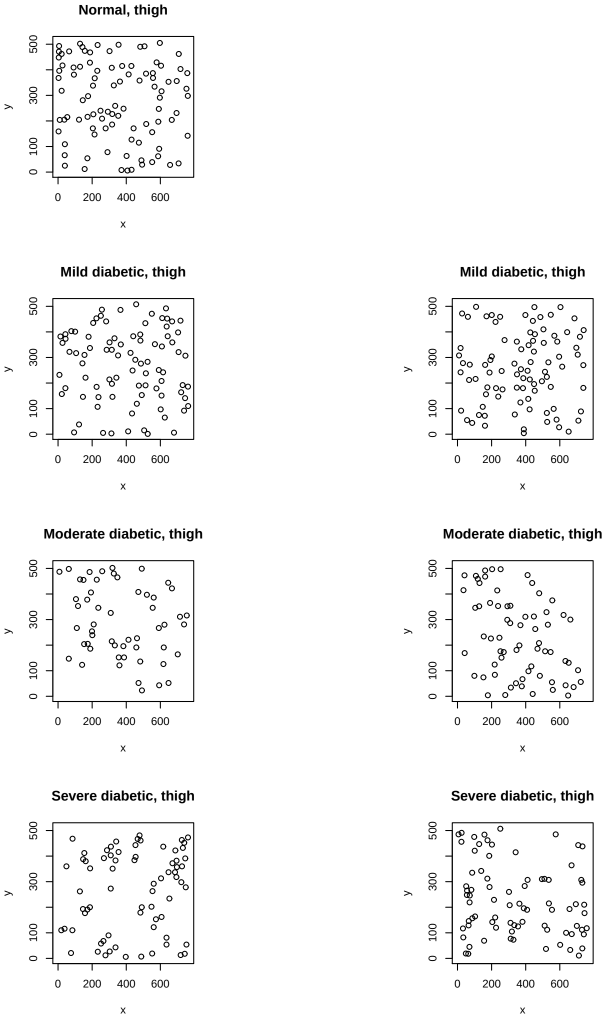

Figure 4: *ENF entry locations from a normal subject (first row), two subjects with mild diabetes (second row), two subjects with moderate diabetes (third row), two subjects with severe diabetes (last row).*

ical K function (hence L function), but $\widehat{K}$ and $\widehat{L}$ based on the thinned data will involve some variability based on which ENFs are removed. At each of 500 simulations, we

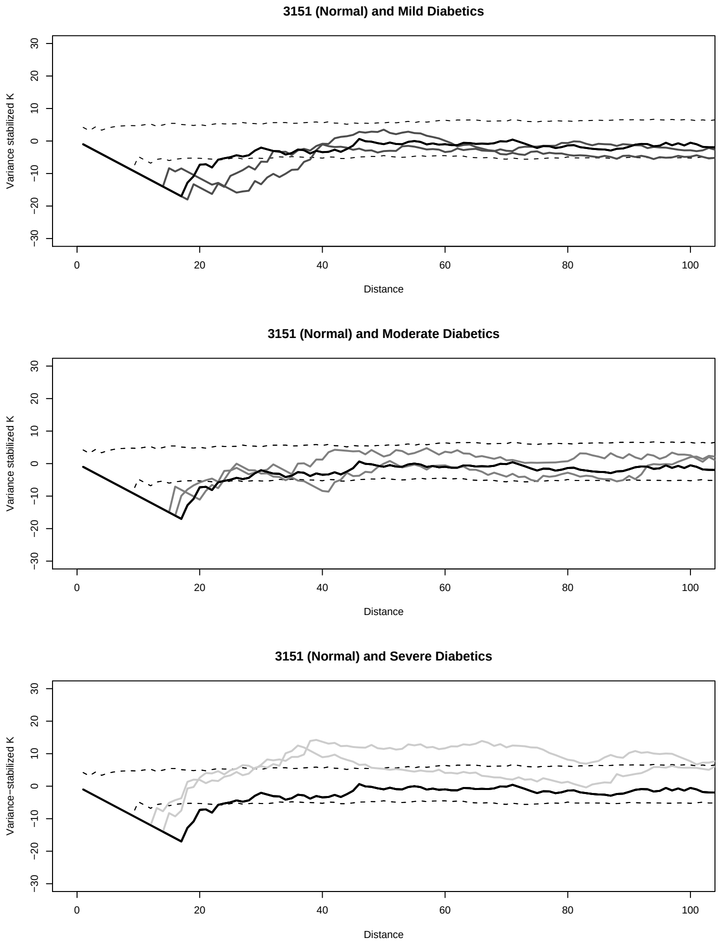

Figure 5: *Estimated variance-stabilized $\widehat{K}$ function ($\widehat{L}$ function) plots for the ENF data. The wide black line represents $\widehat{L}$ for the normal (non-diseased) subject, and the two wide grey lines $\widehat{L}$ for each of the diseased subjects within each disease class. The dashed lines represent the 2.5th and 97.5th percentiles of $\widehat{L}$ based on 500 replications of complete spatial randomness.*

thin the observed normal pattern at random to obtain the same number of ENF entry points as observed in the diabetic patterns, and recalculate $\widehat{L}$. We next calculate the empirical 2.5th and 97.5th percentiles of $\widehat{L}$ at each distance, and plot these envelopes as dotted lines in the middle and bottom rows of Figure 6. Note that the envelope based on the thinned simulations is centered around $\widehat{L}$ based on the non-diseased subject, and maintains the indication of regularity near 20 pixels. We also note much of the "wiggle" in the thinned envelope is due to variability in $\widehat{L}$ for the full data (e.g., peaks in $\widehat{L}$ are mirrored by peaks in the envelopes), and not Monte Carlo variability associated with the thinning process.

We next conduct a Monte Carlo hypothesis test of deviations from the normal pattern for distances between 30 and 60 pixels (approximately 24.8-49.6 microns) based on the test statistic

$$\max_{30 \leq h \leq 60} [L_{dis}(h) - L_{norm}(h)], \tag{5}$$

where $L_{dis}(h)$ is the variance-stabilized K function for the image from a diseased subject and $L_{norm}(h)$ is the same for the non-diseased subject[19]. That is, we compare the maximum observed deviation of the variance-stabilized K functions for images from diseased and non-diseased subjects at distances between 30 and 60 pixels. We choose these distances somewhat subjectively for our exploratory purposes based on the L plots, but we could base the range on the underlying known or suspected physiology for more formal inference. We obtain a distribution under our null hypothesis of random thinning by replacing $L_{dis}(h)$ with the variance-stabilized K function for each of the randomly thinned data sets from our simulation study. The results are not significant in the moderate cases but clearly so in the severe cases. The bottom plot in Figure 6 indicates the significant clustering observed in the severe diabetic subjects in this distance range. Note that we could not compare normal and mild diabetics in a similar manner since, in the images considered, we actually observe more ENFs in the image from the mild diabetic subject than for that of the normal subject. The bottom row of Figure 5 tells the same story: significantly increased clustering observed in the severe diabetic subject at distances between 30 and 60 pixels.

Figure 7 summarizes the estimated pair-correlation functions for the ENF data. The plots suggest increased clustering of ENFs among diabetic subjects, particularly apparent for the severe diabetic subjects. We observe exceedences of the pair-correlation function at lower distances than for $\widehat{L}$ as expected due to the L function's cumulative nature. That is, observed differences in the pair-correlation functions occur at the distance where clustering first occurs, while differences in the $\widehat{L}$ functions do not occur until the cumulative evidence mounts.

We next repeat the test of significance of the observed differences based on random thinnings of the normal pattern by replacing the $\widehat{L}$ in equation (5) by the estimated pair-correlation function in the test statistic, and defining the test for distances between 10 and 40 pixels. Again, we cannot apply the thinning-based test to compare patterns between the mild diabetic subject and the non-diseased subject since we ob-

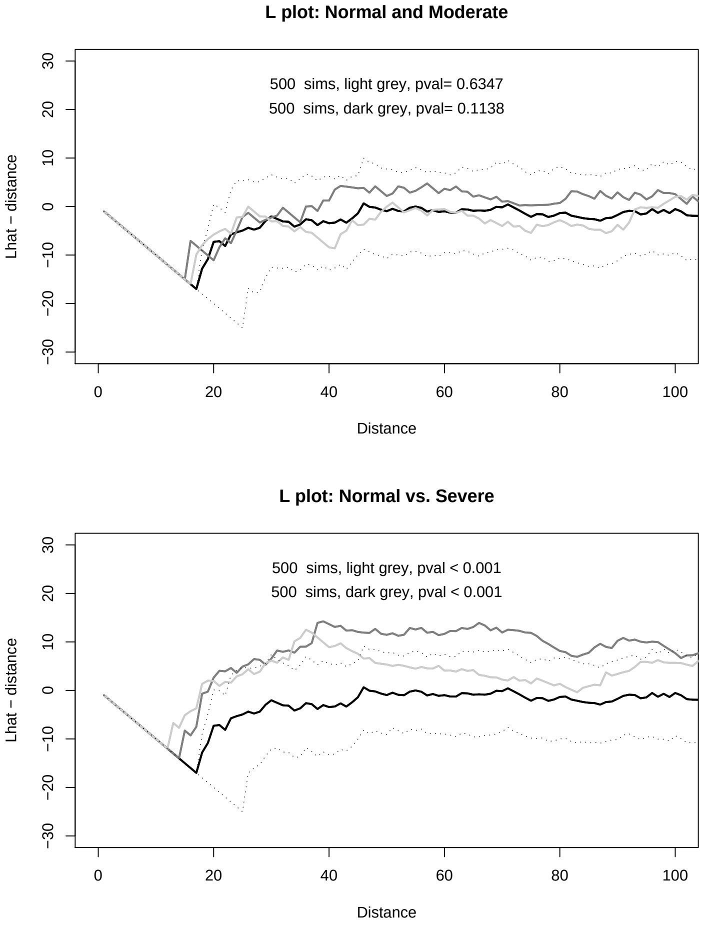

Figure 6: *Estimated variance-stabilized $\widehat{K}$ function ($\widehat{L}$ function) plots for the ENF data. The wide black line represents $\widehat{L}$ for the normal (non-diseased) subject, and the two wide grey lines $\widehat{L}$ for each of the diseased subjects within each disease class. The dashed lines represent the 2.5th and 97.5th percentiles of $\widehat{L}$ based on 500 random thinnings of the observed ENF pattern from the non-diabetic patient.*

serve more ENFs in the mild diabetic subject's images than in those of the non-diseased subject. In all cases, (moderate and severe diabetes) the diseased patterns are significantly more clustered than the normal pattern between 10 and 40 pixels (between 8.3 and 33.1 microns).

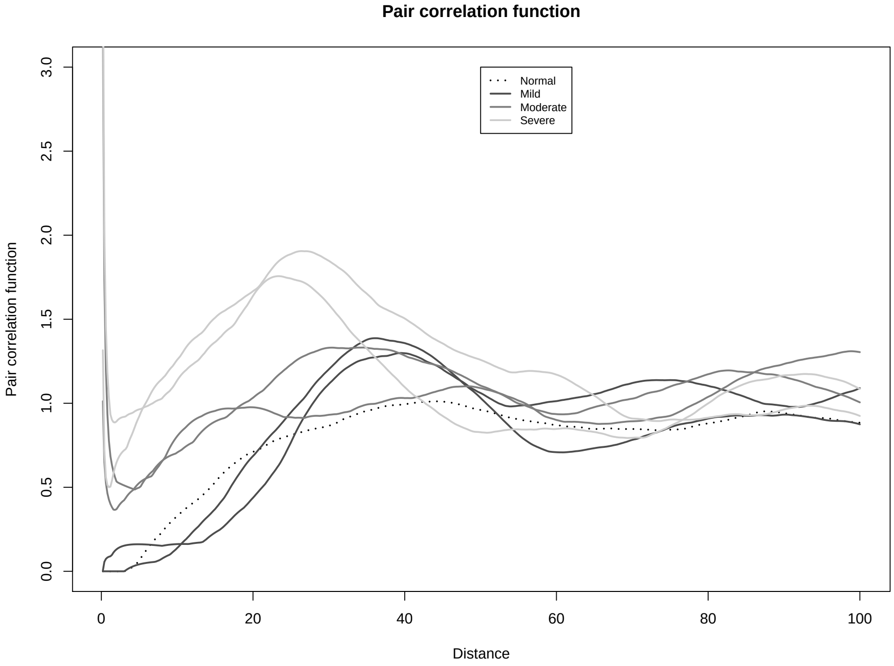

Figure 7: *Estimated pair correlation functions for the ENF data.*

3.2 Fiber Process

We next explore the spatial patterns of the nerve fibers (not only the entry points) by using the fiber K funtion, K_f. As can be seen in Figure 3, the nerve fiber images contain noise in the background, and we use Matlab-based image analysis techniques based on filtering and morphological operations in order to identify the individual fibers[22]. The result for one image can be seen in Figure 8 below.

The fiber K-function can be estimated from the "skeletonized" image by using the estimator given in Section 2.2

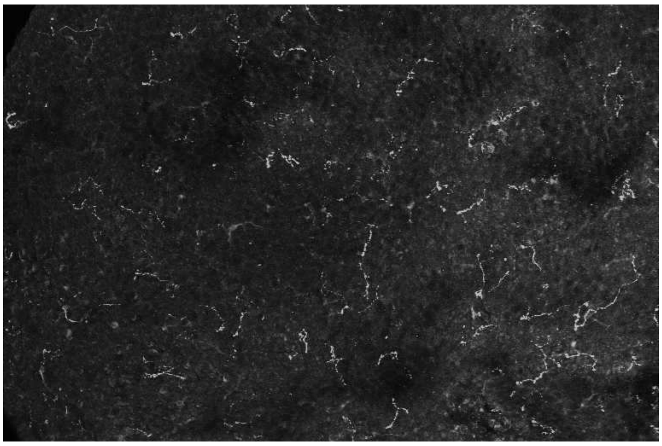

3151 (normal), skeletonized image

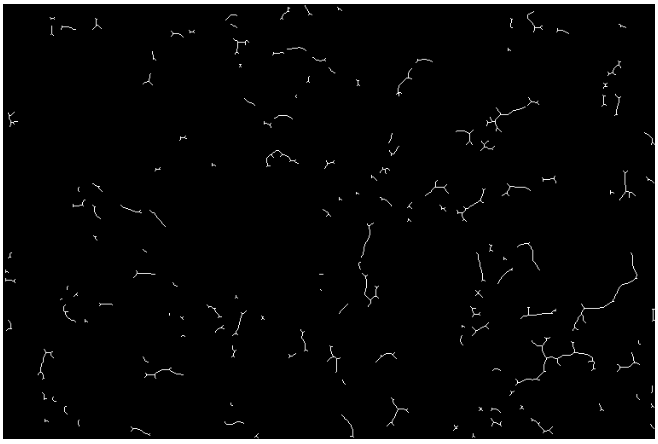

Figure 8: *Sample from a non-diabetic patient and the same image after using image analysis to identify nerve fibers (see text for details).*

It can be seen in Figure 9 that the normal pattern is least clustered, with increasing clustering as one moves to more severe stages of diabetes. We can study the significance of this observation in a similar manner as in Section 3.1. The null hypothesis is again that the diseased patterns are random thinnings of the normal pattern. We again thin the ENF entry points, now removing all fibers associated with the removed point of entry. The normal pattern was thinned at random to obtain the same number of entry points as in the diabetic pattern. Our test is based on 1000 simulations (i.e. random thinnings of

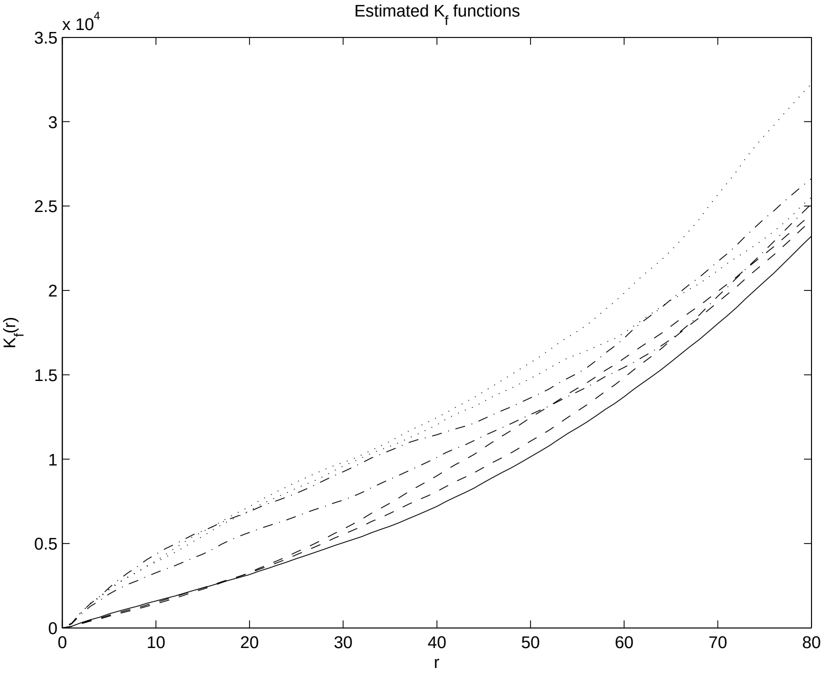

Figure 9: *Estimated K_f: normal (solid line), mild (dashed line), moderate (dashed and dotted line) and severe (dotted line).*

the normal fiber process), and the test statistic used is

$$\begin{aligned} T_{\text{mo}} &= \int_5^{30} [K_{\text{mo}}(h) - K_{\text{n}}(h)]^2 dh, \\ T_{\text{s}} &= \int_5^{30} [K_{\text{s}}(h) - K_{\text{n}}(h)]^2 dh, \end{aligned}$$

where K_{n}, K_{mo} and K_{s} are the fiber K-functions in the normal, moderate and severe cases, respectively. One minor complication involves the need for a unique assignment of each fiber to a unique entry point. To accomplish this, we use the Voronoi tessellation associated with the nerve entry point pattern. The Voronoi cell connected to a particular entry point consists of all points of the study region A that are closer to this entry point than any other entry point[23].

The estimated fiber K functions and the point-wise 95% confidence bounds are displayed in Figure 10. The p-values from the MC-tests are 0.0020 and 0.2458 in the moderate cases and less than 0.0001 in both of the severe cases, respectively. As with our point process above, the difference from the normal pattern is clearly evident in the severe cases. However, by considering the fibers as well as their points of origin, we obtain significant clustering for one of the images from the moderate diabetic.

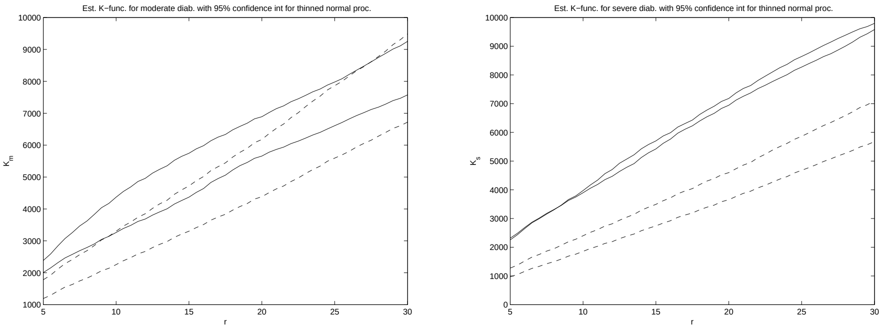

Figure 10: *Estimated fiber K functions for moderate diabetes (left) and severe diabetes (right), together with* 95% *confidence bands for thinned normal fiber process.*

4 DISCUSSION

Our second order analyses of the seven skin blister images suggest that we can quantify the observed variation in clustering of nerve entry points and nerve fibers due to disease state. In addition, these results allow some insight into the spatial scale of clustering, informing on the pathophysiology of ENFs. Furthermore, the initial dip in the L function estimates, see Figure 5, quantifies the size of "territory" per nerve (a feature qualitatively noted in Kennedy et al.[1] (p. 188)), while the pair-correlation function offers quantitative insight into the spatial scale at which observed clustering occurs.

The analyses above are largely exploratory, and represent an attempt to provide statistical quantification of a heuristically observed change in the spatial pattern of ENFs due to diabetes progression. The results illustrate promise in the spatial analysis of blister images, but, to date, most quantitative comparisons of ENFs focuses on changes in density (the average number of ENFs per unit area, calculated from skin punch biopsy data) rather than pattern (observed in blister biopsy data). As a result, the examples above are largely illustrations of the potential of the proposed methods and to set the stage for ongoing blister data collection containing replications within and across individuals in each disease stage. The addition of replicate observations will allow the use of methods from Diggle *et al.*[17] and Baddeley *et al.* [24] to provide average K, fiber

K, and pair correlation function estimates and potential for more thorough analysis.

Intra-individual variation in ENF patterns is an important issue having bearing on any possible global applicability of the results above. Along these lines, the Kennedy Laboratory has completed data collection on a large scale study involving collection of two blisters and two skin-punch biopsies at each of six body sites (foot, calf, thigh, hand, forearm and upper back) for five diseased and five non-diseased subjects in each five-year age group from ages 20 to 75 years. These samples will provide a rich source of data to quantify variation associated with age and gender. In addition, these data provide a unique opportunity to explore age-related trends in observed patterns with relatively short follow-up per subject. Incorporating intra-individual variation into the Monte Carlo approaches above would likely widen simulation envelopes and reduce significance, but provide more realistic models of the underlying variation.

In addition to intra-individual variation, inter-individual variation within disease class and age group will provide important information for more accurate modeling of the ENF process. The large scale study mentioned above will provide valuable insight into this level of variation, and offer opportunities to extend the approaches above to compare ENF patterns between non-diseased and mild diabetic subjects.

In short, our analyses to date show promising preliminary results quantifying differences in the spatial patterns of nerve entry points between diabetic and disease-free subjects. Patterns become more statistically distinguished with disease progression. Future analyses will address additional aspects (e.g., intra-individual variation, subjectivity in locational assignment, possible increased branching of ENFs, and changing ENF lengths) in these interesting neurological data.

ACKNOWLEDGEMENTS

This research was supported in part by NINDS grant R21 NS046258 (LAW) and by the Swedish Research Council and the Swedish Foundation for Strategic Research (AS and VO). The results, conclusions, and opinions expressed here are those of the authors and do not necessarily reflect those of the funding agencies.

References

[1] Kennedy WR, and Wendelschafer-Crabb G The innervation of human epidermis. *Journal of the Neurological Sciences* 1993; **115**: 184–190.

[2] Wang L, Hilliges M, Jernberg T, Wiegleb-Edström D, Johansson O, Protein gene product 9.5-immunoreactive nerve fibers and cells in human skin. *Cell and Tissue Research* 1990; **261**, 25–33.

[3] Kennedy WR, Wendelschafer-Crabb G, Johnson T. Quantitation of epidermal nerves in diabetic neuropathy. *Neurology* 1996; **47**: 1042–1448.

[4] Kennedy WR, Wendelschafer-Crabb G, Polydefkis M, McArthur J. (2005) Pathology and Quantitation of cutaneous nerves. In *Peripheral Neuropathy, 4th ed.*, Dyck PJ, Thomas PK (eds). Saunders: Philadelphia, 2005; 869–896.

[5] McArthur JC, Stocks EA, Hauer P, Cornblath DR, Griffin JW. Epidermal nerve fiber density: Normative reference range and diagnostic efficiency. *Archives of Neurology* 1998; **55**, 1513–1520.

[6] Kennedy WR, Nolano M, Wendelschafer-Crabb G, Johnson TL, and Tamura E. A skin blister method to study epidermal nerves in peripheral nerve disease. *Muscle and Nerve* 1999; **22**: 360–371.

[7] Panoutsopoulou I, Wendelschafer-Crabb G, Hodges JS, Kennedy WR. Skin blister and skin biopsy for quantifying epidermal nerve fibers: a comparative study. Under review.

[8] Illian J, Penttinen A, Stoyan H, and Stoyan D. *Statistical Analysis and Modelling of Spatial Point Patterns*. Wiley: Chichester, 2008.

[9] Diggle PJ. *Statistical Analysis of Spatial Point Patterns*. Academic Press: London, 2003.

[10] Cressie NAC. *Statistics for Spatial Data* (2nd ed.) Wiley: New York, 1993.

[11] Waller LA and Gotway CA. *Applied Spatial Statistics for Public Health Data*. Wiley: Hoboken, NJ, 2004.

[12] Reilly C, Schacker T, Haase AT, Wietgrefe S, Krason D. The clustering of infected SIV cells in lymphatic tissue. *Journal of the American Statistical Association* 2002; **97**, 943–954.

[13] Ripley BD. Modelling spatial patterns. *Journal of the Royal Statistical Society, Series B* 1977; **39**, 172–192.

[14] Baddeley AJ, Silverman BW. A cautionary example on the use of second-order methods for analyzing point patterns. *Biometrics* 1984; **40**: 1089–1093.

[15] Besag JE. Comment on ‘Modelling spatial patterns’ by B.D. Ripley. *Journal of the Royal Statistical Society, Series B* 1977; **39**: 193–195.

[16] Ripley BD. The second-order analysis of stationary point processes. *Journal of Applied Probability* 1976; **13**, 255–266.

[17] Diggle PJ, Lange N, Beneš FM. Analysis of variance for replicated spatial point patterns in clinical neuroanatomy. *Journal of the American Statistical Association* 1991; **86**: 618–625.

[18] Penttinen A, Stoyan D, Henttonen H. Marked point processes in forest statistics. *Forest Science* 1992; **38**, 806–824.

[19] Stoyan D, Kendall WS, and Mecke J. *Stochastic Geometry and Its Applications, 2nd ed*. Wiley: Chichester, 1995.

[20] Stoyan D, Stoyan H. Estimating pair correlation functions of planar cluster processes. *Biometrical Journal* 1996; **38**, 259-271.

[21] Fiksel T. Edge-corrected density estimators for point processes. *Statistics* 1988; **19**: 67–76.

[22] Nisslert R, Kvarnström M, Lorén N, Nydén M, Rudemo M. Identification of the three-dimensional gel microstructure from transmission electron micrographs. *Journal of Microscopy* 2007; **225**, 10–21.

[23] Okabe A, Boots B, Sugihara K. *Spatial Tesselations, Concepts and Applications of Voronoi Diagrams, 2nd ed*. Wiley: Chichester, 2000.

[24] Baddeley AJ, Moyeed RA, Howard CV, Boyde A. Analysis of a three-dimensional point pattern with replication. *Applied Statistics* 1997; **42**: 641–668.

Paper II

A marked Poisson process induced by a random set generated Cox process

Viktor Olsbo

Abstract

Motivated by epidermal nerve fiber patterns, we consider a set of marked Poisson process models in the plane. These models are induced by a bivariate point process, denoted by (Φ_b, Φ_e). The resulting processes are constructed by connecting each point of Φ_e to the nearest point of Φ_b via a line segment. The *base* process Φ_b is a Poisson process, while the *ending* process is a random set generated Cox process.. Furthermore, we introduce hierarchical constraints on Φ_e inducing dependence between the ending and the beginning process. Features of interest are the number of ending points per base, individual branch length, total branch length per base, angle between base and ending.

Keywords: Cox process; Epidermal nerve fibers; Mark Distributions; Poisson process; Random closed sets; Stienen model; Voronoi tessellation.

1 Introduction

Consider two stationary point processes in $\mathbb{R}^2$, Φ_b and Φ_e, having intensities λ_b and λ_e, respectively. Here, b stands for beginning and e stands for ending. We connect each point $\mathbf{y} \in \Phi_e$ to the closest point in $\mathbf{x} \in \Phi_b$. That is, each "end" $\mathbf{y} \in \Phi_e$, is connected to a unique "beginning" in Φ_b. Note that a single beginning may be connected to multiple (or zero) ends. The case of both Φ_e and Φ_b being Poisson processes was explored by Foss and Zuyev [2], where the authors introduce this type of process as a model for telecommunication networks. For example the base process can consist of locations of the base stations and the end process of the locations of the users of the network, e.g. mobil phones or broad band.

Our motivation for studying this type of model is coming from reinnervation of the epidermis. Epidermal nerve fibers (ENFs) are thin sensory fibers in the epidermis. The fibers grow from the basement membrane of the dermis and up into the epidermis via a trunk and then branch out in the epidermis. The terminal nodes of the fibres transmit sensations of heat and pain through the ENFs to the central nervous system. Kennedy *et al.* [4] first imaged ENFs from skin biopsies. ENFs appear in the epidermis throughout the body. The number of ENFs per square unit of skin decreases as one moves to more peripheral sites in the body (i.e., the intensity of ENFs is smaller in the hands and feet than in the central parts of the body), and several researchers have noted significant reduction in ENF intensity in patients experiencing diabetic neuropathy (nerve and sensory loss, often severe, in diabetic patients) [5, 6].

Here, one aim is to find models that have enough flexibility to capture the above described changes in the observed patterns. In our setting we would like to be able to have flexibility in both the beginning and the ending process. That is, it is not only the system of nerve fibre trunks that changes as a neuropathy advances but also the fibre structure. As always though, there is a balance between model complexity and analytical tractability. Even in the baseline case of both processes being Poisson processes it is hard to obtain analytical results regarding distributions for characteristics, also called marks, of the fibre structure, i.e. for branch length etc. In order to not completely depend on simulation based evaluation of the models we confine to the case when the base process is a Poisson process. For measurable functions $g : \mathbb{R}^2 \to \mathbb{R}_+$ we define the following additive functional

$$\Sigma_g = \sum_{\mathbf{x} \in \Phi_e} g(\mathbf{x}) \mathbf{1}_{\mathcal{V}_o}(\mathbf{x}), \tag{1.1}$$

where $\mathcal{V}_o$ is the typical cell of the Poisson-Voronoi tessellation generated by Φ_b. For specific choices of the function g we obtain characteristics of some of the marks we are interested in. We have however not been able to obtain analytical results for the mark distributions. When it comes to the functional in (1.1) most results concern mean, variance and covariance. These results can be used in the first step of inference for observed patterns, but also when evaluating estimators. We give integral formulas in the case when Φ_e is a general stationary and isotropic point process and provide numerical results when Φ_e is a specific type of Cox process, namely a *random set generated Cox process*. This type of process was introduced by Penttinen and Niemi [11], motivated by an application in forestry. Here the driving random measure is based on a random set model and this model is of interest in connection with the ENF patterns since the random set model can represent an underlying heterogeneity in the epidermis. We look in more detail in the case of the random set being the Stienen model generated by Φ_b. It should be noted that this procedure will induce dependence between the beginning and ending processes. Other Cox processes, e.g. when the driving measure is a random field, could be of interest as well. One example of this is the Log-Gaussian Cox process introduced by Møller *et al.* [9]. In this case as well, the random field would represent some sort of underlying heterogeneity.

To apply the type of process where the jagged and irregular nerve fiber branches are replaced by line segments is of course a great simplification, but it can be justified by the fact that it is only the endings of the nerve fibers that transmit heat, pain etc. Some of the results and proofs thereof in this paper are based on ideas in Foss and Zuyev [2]. In this paper, all results are given in $\mathbb{R}^2$, but many of them can be extended into $\mathbb{R}^d$ without much effort.

2 Definition of the process

The specific ending process we consider is a *random set generated Cox process* (RSGCP). Following Penttinen and Niemi [11], we divide the plane into two regions (or phases) Θ and Θ^c, respectively, where Θ is a stationary random closed set, see e.g. [16]. Conditionally on Θ, the points in Θ and Θ^c are distributed according to two independent Poisson processes Φ_1 and Φ_2 having intensities λ_1 and λ_2, respectively. Then $\Phi_e = \Phi_1 \cup \Phi_2$. This is a flexible generalization of a Poisson process and with an ENF application in mind Θ will represent an underlying heterogeneity in the epidermis. Note that Φ_e is stationary, since Θ is stationary. In Figure 1, four different realizations of the RSGCP, when Θ is the Stienen model generated by Φ_b (see Section 3), are displayed.

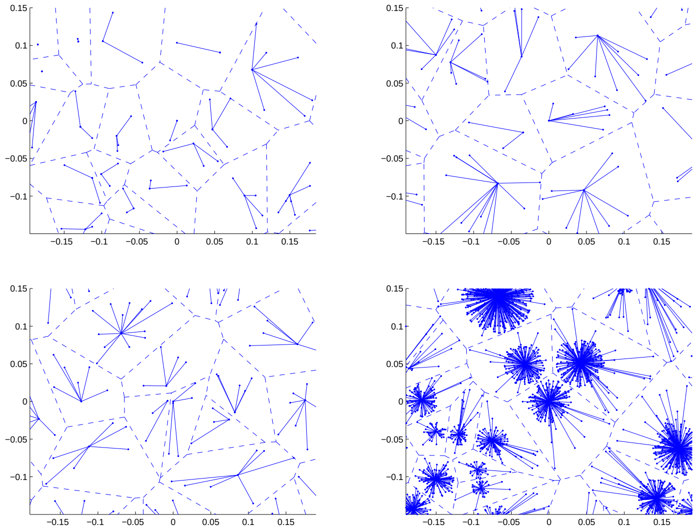

Figure 1: *Realizations of the RSGCP when* Θ *is the Stienen model generated by* Φ_b*. Top left:* $\lambda_1 = 700$, $\lambda_2 = 300$*. Top right:* $\lambda_1 = 300$, $\lambda_2 = 700$*. Bottom Left:* $\lambda_1 = \lambda_2 = 700$*. Bottom right:* $\lambda_1 = 50000$, $\lambda_2 = 2000$, $\lambda_b = 100$ *in all cases.*

The intensity measure of the ending process is given by

$$\Lambda_e(x) = \lambda_1 \mathbf{1}_{\Theta}(x) + \lambda_2 \mathbf{1}_{\Theta^c}(x), \tag{2.1}$$

and then

$$\lambda_e(x) = \mathbb{E}[\Lambda_e(x)] = \lambda_1 P(\mathbf{x} \in \Theta) + \lambda_2 P(\mathbf{x} \in \Theta^c) = p\lambda_1 + (1-p)\lambda_2, \tag{2.2}$$

where p is the area fraction of the random closed set and is defined by $p = P(o \in \Theta)$. Since the process is stationary the intensity is constant and denoted by λ_e. Furthermore, the pair-correlation function of the ending process is given by

$$g_e(r) = \frac{1}{\lambda_e^2}[C(r)(\lambda_1 - \lambda_2)^2 + 2p(\lambda_1 - \lambda_2)\lambda_2 + \lambda_2^2], \tag{2.3}$$

where $C(r)$ is the covariance of the random closed set Θ [11]. The function $C(r)$ is defined by $C(r) = P(o \in \Theta, \mathbf{x} \in \Theta)$, for $|\mathbf{x}| = r$.

If we let $\mathcal{V}$ denote the Voronoi tessellation based on the points in Φ_b, and $\mathcal{V}_{\mathbf{x}}$ is the Voronoi cell associated with the point $\mathbf{x} \in \Phi_b$, i.e.

$$\mathcal{V}_{\mathbf{x}} = \{\mathbf{y} \in \mathbb{R}^2 : |\mathbf{y} - \mathbf{x}| \leq |\mathbf{y} - \mathbf{z}|, \forall \mathbf{z} \in \Phi_b\},$$

we can write

$$\mathcal{V} = \{\, \mathcal{V}_{\mathbf{x}} \, : \, \mathbf{x} \in \Phi_b \,\}.$$

Then, if $\mathbf{y} \in \mathcal{V}_{\mathbf{x}}$ it means that $\mathbf{y}$ is connected to $\mathbf{x}$. There is a notion of a *typical cell*, which represents a (loosely speaking) randomly chosen cell. If we assume that $o \in \Phi_b$, then $\mathcal{V}_o$ denotes the cell having the origin as nucleus. It is known that, see e.g. Møller [8], $\mathcal{V}_o$ and the typical cell have the same distributional properties and it therefore in our case suffices to regard $\mathcal{V}_o$.

As mentioned in the introduction, following the ideas in [2], we will regard the following additive functional. In the definition we do not restrict Φ_e to be a RSGCP, it can be any motion-invariant point process.

DEFINITION 1. *For any measurable function* $f : \mathbb{R}^2 \to \mathbb{R}_+$, *let*

$$\Sigma_f = \sum_{\mathbf{x} \in \Phi_e} f(\mathbf{x}) \mathbf{1}_{\mathcal{V}_o}(\mathbf{x}), \tag{2.4}$$

and further for $f(\mathbf{x}) = 1$ *and* $f(\mathbf{x}) = |\mathbf{x}|$, *define*

$$N = \sum_{\mathbf{x} \in \Phi_e} \mathbf{1}_{\mathcal{V}_o}(\mathbf{x}), \tag{2.5}$$

$$L = \sum_{\mathbf{x} \in \Phi_e} |\mathbf{x}| \mathbf{1}_{\mathcal{V}_o}(\mathbf{x}), \tag{2.6}$$

i.e. the number of endings and the total branch length associated with the typical cell, respectively.

In the following we will assume that the function f is such that the second moment of Σ_f exists and is finite. Now, for any motion-invariant ending process, we can state the following theorem giving integral formulas for the mean of and covariance between different functionals of the form given in (2.4). If nothing else is mentioned, the base process is a Poisson process.

THEOREM 1. *Let Φ_b be a homogenous Poisson process independent of a motion-invariant point process, Φ_e. Then, for measurable functions $f, f_1, f_2 : \mathbb{R}^2 \to \mathbb{R}_+$ the following two assertions hold*

$$\mathbb{E}[\Sigma_f] = \lambda_e \int_{\mathbb{R}^2} f(\mathbf{x}) \mathrm{e}^{-\lambda_b \pi |\mathbf{x}|^2} d\mathbf{x}, \tag{2.7}$$

and

$$\begin{aligned} \mathrm{Cov}\,(\Sigma_{f_1}, \Sigma_{f_2}) = {} & \lambda_e \int_{\mathbb{R}^2} f_1(\mathbf{x}) f_2(\mathbf{x}) \mathrm{e}^{-\lambda_b \pi |\mathbf{x}|^2} d\mathbf{x} \\ & + \lambda_e^2 \int_{\mathbb{R}^2} \int_{\mathbb{R}^2} f_1(\mathbf{x}_1) f_2(\mathbf{x}_2) \mathrm{e}^{-\lambda_b U(\mathbf{x}_1, \mathbf{x}_2)} g_e(|\mathbf{x}_1 - \mathbf{x}_2|) d\mathbf{x}_1 d\mathbf{x}_2 \\ & - \lambda_e^2 \int_{\mathbb{R}^2} \int_{\mathbb{R}^2} f_1(\mathbf{x}_1) f_2(\mathbf{x}_2) \mathrm{e}^{-\lambda_b \pi (|\mathbf{x}_1|^2 + |\mathbf{x}_2|^2)} d\mathbf{x}_1 d\mathbf{x}_2, \end{aligned} \tag{2.8}$$

where g_e is the pair-correlation function of the ending process and $U(\mathbf{x}_1, \mathbf{x}_2)$ is the area of the union of two disks centered at $\mathbf{x}_1$ and $\mathbf{x}_2$ and having radii $|\mathbf{x}_1|$ and $|\mathbf{x}_2|$, respectively.

Proof of (2.7). The result follows by recognizing that

$$\begin{aligned} \mathbb{E}[\Sigma_f] &= \mathbb{E}[\mathbb{E}[\Sigma_f \mid \Phi_b]] = \mathbb{E}[\lambda_e \int_{\mathbb{R}^2} f(\mathbf{x}) \mathbf{1}_{\mathcal{V}_o}(\mathbf{x}) d\mathbf{x}] \\ &= \lambda_e \int_{\mathbb{R}^2} f(\mathbf{x}) P(\mathbf{x} \in \mathcal{V}_o) d\mathbf{x} = \lambda_e \int_{\mathbb{R}^2} f(\mathbf{x}) \mathrm{e}^{-\pi \lambda_b |\mathbf{x}|^2} d\mathbf{x}. \end{aligned} \tag{2.9}$$

The last equality holds since $\mathbf{x} \in \mathcal{V}_o$ is equivalent to $\Phi_b \cap b(\mathbf{x}, |\mathbf{x}|) = \emptyset$. □

Using (2.7), straight forward calculations give

$$\mathbb{E}[N] = \frac{\lambda_e}{\lambda_b} \quad \text{and} \quad \mathbb{E}[L] = \frac{\lambda_e}{2\lambda_b^{\frac{3}{2}}}.$$

It should be noted that these can alternatively be obtained using conditioning. Also, the expectation of N holds for any stationary point process, Φ_e, Φ_b while the expectation of L relies on Φ_b being a Poisson process.

In order to prove (2.8) we will use the following lemma.

LEMMA 1. *For a stationary point process* Φ *in* $\mathbb{R}^2$ *and measurable functions* $f_1, f_2 : \mathbb{R}^2 \to \mathbb{R}_+$*, the following assertion holds*

$$\begin{aligned}\mathrm{Cov}\left(\sum_{\mathbf{x}\in\Phi} f_1(\mathbf{x}), \sum_{\mathbf{x}\in\Phi} f_2(\mathbf{x})\right) &= \lambda \int_{\mathbb{R}^2} f_1(\mathbf{x}) f_2(\mathbf{x}) d\mathbf{x} \\ &+ \int_{\mathbb{R}^2}\int_{\mathbb{R}^2} f_1(\mathbf{x}_1) f_2(\mathbf{x}_2) \varrho^{(2)}(\mathbf{x}_1, \mathbf{x}_2) d\mathbf{x}_1 d\mathbf{x}_2, \\ &- \lambda^2 \int_{\mathbb{R}^2}\int_{\mathbb{R}^2} f_1(\mathbf{x}_1) f_2(\mathbf{x}_2) d\mathbf{x}_1 d\mathbf{x}_2,\end{aligned} \tag{2.10}$$

where $\varrho^{(2)}$ *is the* second-order product density *of* Φ.

Proof. We can write

$$\begin{aligned}&\mathrm{Cov}\left(\sum_{\mathbf{x}\in\Phi} f_1(\mathbf{x}), \sum_{\mathbf{x}\in\Phi} f_2(\mathbf{x})\right) \\ &= \mathbb{E}\left[\sum_{\mathbf{x}_1,\mathbf{x}_2\in\Phi} f_1(\mathbf{x}_1) f_2(\mathbf{x}_2)\right] - \mathbb{E}\left[\sum_{\mathbf{x}\in\Phi} f_1(\mathbf{x})\right] \mathbb{E}\left[\sum_{\mathbf{x}\in\Phi} f_2(\mathbf{x})\right].\end{aligned} \tag{2.11}$$

Furthermore, we have that

$$\begin{aligned}\mathbb{E}\left[\sum_{\mathbf{x}_1,\mathbf{x}_2\in\Phi} f_1(\mathbf{x}_1) f_2(\mathbf{x}_2)\right] &= \mathbb{E}\left[\sum_{\mathbf{x}\in\Phi} f_1(\mathbf{x}) f_2(\mathbf{x})\right] + \mathbb{E}\left[\sum_{\substack{\mathbf{x}_1,\mathbf{x}_2\in\Phi \\ \mathbf{x}_1\neq\mathbf{x}_2}} f_1(\mathbf{x}_1) f_2(\mathbf{x}_2)\right] \\ &= \lambda \int_{\mathbb{R}^d} f_1(\mathbf{x}) f_2(\mathbf{x}) d\mathbf{x} \\ &+ \int_{\mathbb{R}^2}\int_{\mathbb{R}^2} f_1(\mathbf{x}_1) f_2(\mathbf{x}_2) \varrho^{(2)}(\mathbf{x}_1, \mathbf{x}_2) d\mathbf{x}_1 d\mathbf{x}_2,\end{aligned}$$

where the last equality follows from the Campbell theorem, see e.g. [16] and Equation (14.20) in [17]. The lemma now follows from using the Campbell theorem on the last term of the right-hand side of (2.11). □

Proof of (2.8). We have for random variables X, Y and any σ-algebra $\mathcal{Z}$ that

$$\mathrm{Cov}(X, Y) = \mathrm{Cov}(\mathbb{E}[X|\mathcal{Z}], \mathbb{E}[Y|\mathcal{Z}]) + \mathbb{E}[\mathrm{Cov}(X, Y|\mathcal{Z})]. \tag{2.12}$$

By using (2.12) we have

$$\mathrm{Cov}\left(\Sigma_{f_1}, \Sigma_{f_2}\right) = \mathbb{E}\left[\mathrm{Cov}\left(\Sigma_{f_1}, \Sigma_{f_2} \middle| \Phi_b\right)\right] + \mathrm{Cov}\left(\mathbb{E}[\Sigma_{f_1} \mid \Phi_b], \mathbb{E}[\Sigma_{f_2} \mid \Phi_b]\right). \quad (2.13)$$

Now, from Lemma 1 it follows that

$$\begin{aligned}
&\mathbb{E}\left[\mathrm{Cov}\left(\Sigma_{f_1}, \Sigma_{f_2} \middle| \Phi_b\right)\right] \\
&\quad = \mathbb{E}\left[\lambda_e \int_{\mathbb{R}^2} f_1(\mathbf{x}) f_2(\mathbf{x}) \mathbf{1}_{\mathcal{V}_o}(\mathbf{x}) d\mathbf{x}\right] \\
&\qquad + \ \mathbb{E}\left[\int_{\mathbb{R}^2}\int_{\mathbb{R}^2} f_1(\mathbf{x}_1) f_2(\mathbf{x}_2) \mathbf{1}_{\mathcal{V}_o}(\mathbf{x}_1, \mathbf{x}_2) \varrho_e^{(2)}(\mathbf{x}_1, \mathbf{x}_2) d\mathbf{x}_1 d\mathbf{x}_2\right] \\
&\qquad - \ \mathbb{E}\left[\lambda_e^2 \int_{\mathbb{R}^2}\int_{\mathbb{R}^2} f_1(\mathbf{x}_1) f_2(\mathbf{x}_2) \mathbf{1}_{\mathcal{V}_o}(\mathbf{x}_1, \mathbf{x}_2) d\mathbf{x}_1 d\mathbf{x}_2\right] \\
&\quad = \lambda_e \int_{\mathbb{R}^2} f_1(\mathbf{x}) f_2(\mathbf{x}) P(\mathbf{x} \in \mathcal{V}_o) d\mathbf{x} \\
&\qquad + \ \int_{\mathbb{R}^2}\int_{\mathbb{R}^2} f_1(\mathbf{x}_1) f_2(\mathbf{x}_2) P(\mathbf{x}_1, \mathbf{x}_2 \in \mathcal{V}_o) \varrho_e^{(2)}(\mathbf{x}_1, \mathbf{x}_2) d\mathbf{x}_1 d\mathbf{x}_2 \\
&\qquad - \ \lambda_e^2 \int_{\mathbb{R}^2}\int_{\mathbb{R}^2} f_1(\mathbf{x}_1) f_2(\mathbf{x}_2) P(\mathbf{x}_1, \mathbf{x}_2 \in \mathcal{V}_o) d\mathbf{x}_1 d\mathbf{x}_2 \\
&\quad = \lambda_e \int_{\mathbb{R}^2} f_1(\mathbf{x}) f_2(\mathbf{x}) \mathrm{e}^{-\pi\lambda_b|\mathbf{x}|^2} d\mathbf{x} \\
&\qquad + \ \int_{\mathbb{R}^2}\int_{\mathbb{R}^2} f_1(\mathbf{x}_1) f_2(\mathbf{x}_2) \mathrm{e}^{-\lambda_b U(\mathbf{x}_1, \mathbf{x}_2)} \varrho_e^{(2)}(\mathbf{x}_1, \mathbf{x}_2) d\mathbf{x}_1 d\mathbf{x}_2 \\
&\qquad - \ \lambda_e^2 \int_{\mathbb{R}^2}\int_{\mathbb{R}^2} f_1(\mathbf{x}_1) f_2(\mathbf{x}_2) \mathrm{e}^{-\lambda_b U(\mathbf{x}_1, \mathbf{x}_2)} d\mathbf{x}_1 d\mathbf{x}_2, \qquad (2.14)
\end{aligned}$$

where the last equality holds since $\mathbf{x}_1, \mathbf{x}_2 \in \mathcal{V}_o$ is equivalent to

$$\Phi_b \cap \left(b(\mathbf{x}_1, |\mathbf{x}_1|) \cup b(\mathbf{x}_2, |\mathbf{x}_2|)\right) = \emptyset.$$

Furthermore, using (2.7) we obtain

$$\begin{aligned}
&\text{Cov}\left(\mathbb{E}[\Sigma_{f_1} \mid \Phi_b], \mathbb{E}[\Sigma_{f_2} \mid \Phi_b]\right) \\
&\quad = \text{Cov}\left(\lambda_e \int_{\mathbb{R}^2} f_1(\mathbf{x}_1)\mathbf{1}_{\mathcal{V}_o}(\mathbf{x}_1)d\mathbf{x}_1, \lambda_e \int_{\mathbb{R}^2} f_2(\mathbf{x}_2)\mathbf{1}_{\mathcal{V}_o}(\mathbf{x}_2)d\mathbf{x}_2\right) \\
&\quad = \mathbb{E}\left[\lambda_e^2 \int_{\mathbb{R}^2}\int_{\mathbb{R}^2} f_1(\mathbf{x}_1)f_2(\mathbf{x}_2)\mathbf{1}_{\mathcal{V}_o}(\mathbf{x}_1,\mathbf{x}_2)d\mathbf{x}_1 d\mathbf{x}_2\right] \\
&\quad - \mathbb{E}\left[\lambda_e \int_{\mathbb{R}^2} f_1(\mathbf{x}_1)\mathbf{1}_{\mathcal{V}_o}(\mathbf{x}_1)d\mathbf{x}_1\right]\mathbb{E}\left[\lambda_e \int_{\mathbb{R}^2} f_2(\mathbf{x}_2)\mathbf{1}_{\mathcal{V}_o}(\mathbf{x}_2)d\mathbf{x}_2\right] \\
&\quad = \lambda_e^2 \int_{\mathbb{R}^2}\int_{\mathbb{R}^2} f_1(\mathbf{x}_1)f_2(\mathbf{x}_2)P(\mathbf{x}_1,\mathbf{x}_2 \in \mathcal{V}_o)d\mathbf{x}_1 d\mathbf{x}_2 \\
&\quad - \lambda_e^2 \int_{\mathbb{R}^2}\int_{\mathbb{R}^2} f_1(\mathbf{x}_1)f_2(\mathbf{x}_2)P(\mathbf{x}_1 \in \mathcal{V}_o)P(\mathbf{x}_2 \in \mathcal{V}_o)d\mathbf{x}_1 d\mathbf{x}_2 \\
&\quad = \lambda_e^2 \int_{\mathbb{R}^2}\int_{\mathbb{R}^2} f_1(\mathbf{x}_1)f_2(\mathbf{x}_2)\mathrm{e}^{-\lambda_b U(\mathbf{x}_1,\mathbf{x}_2)}d\mathbf{x}_1 d\mathbf{x}_2 \\
&\quad - \lambda_e^2 \int_{\mathbb{R}^2}\int_{\mathbb{R}^2} f_1(\mathbf{x}_1)f_2(\mathbf{x}_2)\mathrm{e}^{-\pi\lambda_b(|\mathbf{x}_1|^2+|\mathbf{x}_2|^2)}d\mathbf{x}_1 d\mathbf{x}_2 \qquad (2.15)
\end{aligned}$$

Lastly, we use the relationship $\varrho_e^{(2)}(\mathbf{x}_1,\mathbf{x}_2) = \lambda_e^2 g_e(|\mathbf{x}_1 - \mathbf{x}_2|)$. □

To obtain results concerning variances and covariances of e.g. N and L in the RSGCP setting, we would need to use Theorem 1 together with (2.3). The main challenge then is to evaluate

$$\int_{\mathbb{R}^2}\int_{\mathbb{R}^2} C(|\mathbf{x}_1 - \mathbf{x}_2|)\,\mathrm{e}^{-\lambda_b U(\mathbf{x}_1,\mathbf{x}_2)}d\mathbf{x}_1 d\mathbf{x}_2,$$

for given covariance function $C(r)$. Unfortunately, $C(r)$ is hard to obtain analytically and is known only for a few models. Even in the cases when it is known it has a complicated form. One possible approach would be to use any of the following approximations of $C(r)$

$$C(r) \approx p(1-p)\mathrm{e}^{-ar} + p^2 \quad \text{or} \quad C(r) \approx p(1-p)\mathrm{e}^{-(ar+br^2)} + p^2,$$

which are valid for suitable choices of a and b [1].

The following result lies a little bit outside the main scope of the paper but is worth mentioning. In the case when Θ and Φ_b are independent, it is possible to obtain the following integral expression for $\text{Cov}(|\mathcal{V}_o \cap \Theta|, |\mathcal{V}_o \cap \Theta^c|)$.

PROPOSITION 1. *If Θ and Φ_b are independent, then*

$$\begin{aligned}\mathrm{Cov}(|\mathcal{V}_o \cap \Theta|, |\mathcal{V}_o \cap \Theta^c|) = p \int_{\mathbb{R}^2}\int_{\mathbb{R}^2} \mathrm{e}^{-\lambda_b U(\mathbf{x}_1,\mathbf{x}_2)} d\mathbf{x}_1 d\mathbf{x}_2 - \frac{p\,(1-p)}{\lambda_b^2} \\ - \int_{\mathbb{R}^2}\int_{\mathbb{R}^2} \mathrm{e}^{-\lambda_b U(\mathbf{x}_1,\mathbf{x}_2)} C(|\mathbf{x}_1 - \mathbf{x}_2|) d\mathbf{x}_1 d\mathbf{x}_2. \quad (2.16)\end{aligned}$$

Proof. We have that

$$\mathrm{Var}(|\mathcal{V}_o|) = \mathrm{Var}(|\mathcal{V}_o \cap \Theta|) + \mathrm{Var}(|\mathcal{V}_o \cap \Theta^c|) + 2\mathrm{Cov}(|\mathcal{V}_o \cap \Theta|, |\mathcal{V}_o \cap \Theta^c|). \quad (2.17)$$

By using Robbin's formula [12, 13] we obtain

$$\begin{aligned}\mathrm{Var}(|\mathcal{V}_o|) &= \int_{\mathbb{R}^2}\int_{\mathbb{R}^2} \mathrm{e}^{-\lambda_b U(\mathbf{x}_1,\mathbf{x}_2)} d\mathbf{x}_1 d\mathbf{x}_2 - \frac{1}{\lambda_b^2}, \quad (2.18)\\ \mathbb{E}[|\mathcal{V}_o \cap \Theta|] &= \int_{\mathbb{R}^2} P(x \in \mathcal{V}_o \cap \Theta) d\mathbf{x} = \int_{\mathbb{R}^2} P(x \in \mathcal{V}_o) P(\mathbf{x} \in \Theta) d\mathbf{x} \\ &= p \int_{\mathbb{R}^2} \mathrm{e}^{-\pi\lambda_b |\mathbf{x}|^2} d\mathbf{x} = \frac{p}{\lambda_b}, \quad (2.19)\end{aligned}$$

and

$$\begin{aligned}\mathrm{Var}(|\mathcal{V}_o \cap \Theta|) &= \mathbb{E}[|\mathcal{V}_o \cap \Theta|^2] - \mathbb{E}[|\mathcal{V}_o \cap \Theta|]^2 \\ &= \int_{\mathbb{R}^2}\int_{\mathbb{R}^2} P(\mathbf{x}_1, \mathbf{x}_2 \in \mathcal{V}_o \cap \Theta) d\mathbf{x}_1 d\mathbf{x}_2 - \frac{p^2}{\lambda_b^2} \\ &= \int_{\mathbb{R}^2}\int_{\mathbb{R}^2} P(\mathbf{x}_1, \mathbf{x}_2 \in \mathcal{V}_o) P(\mathbf{x}_1, \mathbf{x}_2 \in \Theta) d\mathbf{x}_1 d\mathbf{x}_2 - \frac{p^2}{\lambda_b^2} \\ &= \int_{\mathbb{R}^2}\int_{\mathbb{R}^2} C(|\mathbf{x}_1 - \mathbf{x}_2|)\, \mathrm{e}^{-\lambda_b U(\mathbf{x}_1,\mathbf{x}_2)} d\mathbf{x}_1 d\mathbf{x}_2 - \frac{p^2}{\lambda_b^2}. \quad (2.20)\end{aligned}$$

By similar arguments

$$\begin{aligned}\mathrm{Var}(|\mathcal{V}_o \cap \Theta^c|) = (1-2p) \int_{\mathbb{R}^2}\int_{\mathbb{R}^2} \mathrm{e}^{-\lambda_b U(\mathbf{x}_1,\mathbf{x}_2)} d\mathbf{x}_1 d\mathbf{x}_2 \\ + \int_{\mathbb{R}^2}\int_{\mathbb{R}^2} C(|\mathbf{x}_1 - \mathbf{x}_2|)\, \mathrm{e}^{-\lambda_b U(\mathbf{x}_1,\mathbf{x}_2)} d\mathbf{x}_1 d\mathbf{x}_2 - \frac{(1-p)^2}{\lambda_b^2}, \\ (2.21)\end{aligned}$$

where we have used that

$$P(\mathbf{x}_1, \mathbf{x}_2 \notin \Theta) = P(\mathbf{x}_1 \notin \Theta) + P(\mathbf{x}_2 \notin \Theta) - P\left(\mathbf{x}_1 \notin \Theta \cup \mathbf{x}_2 \notin \Theta\right). \quad (2.22)$$

The result follows by combining (2.18)-(2.21). □

A numerical approximation, first given by Gilbert [3] is the following

$$\int_{\mathbb{R}^2}\int_{\mathbb{R}^2} \mathrm{e}^{-\lambda_b U(\mathbf{x}_1,\mathbf{x}_2)} d\mathbf{x}_1 d\mathbf{x}_2 \approx 1.280\lambda_b^{-2},$$

but as mentioned above, it is difficult to evaluate the second integral.

2.1 Branch length distribution

We will now derive the distribution of the length of a randomly chosen branch, i.e. the distance from a typical point of Φ_e to the nearest point of Φ_b. Here, Φ_e can be any motion-invariant point process, independent of Φ_b. Since Φ_b and Φ_e are independent the distribution of B is then given by the *spherical contact distribution* of the base process, denoted by H_b. This holds since, the typical point of Φ_e is just a random point in space. More formally, this can be seen using the following suitable definition of the distribution function of B

$$P(B \le r) = \frac{1}{\lambda_e |A|}\mathbb{E}\left[\sum_{\mathbf{x}\in\Phi_e\cap A} \mathbf{1}_{\{\Phi_b(b(\mathbf{x},r))>0\}}\right], \tag{2.23}$$

for any set $A \subset \mathbb{R}^2$ s.t. $0 < |A| < \infty$. Here $b(\mathbf{x}, r)$ denotes a closed disk in $\mathbb{R}^2$ with center $\mathbf{x}$ and radius r. Now, for any given set A we have that

$$\begin{aligned}
\mathbb{E}\left[\sum_{\mathbf{x}\in\Phi_e\cap A} \mathbf{1}_{\{\Phi_b(b(\mathbf{x},r))>0\}}\right] &= \mathbb{E}\left[\mathbb{E}\left[\sum_{\mathbf{x}\in\Phi_e} \mathbf{1}_{\{\Phi_b(b(\mathbf{x},r))>0,\, \mathbf{x}\in A\}} \middle| \Phi_b\right]\right] \\
&= \lambda_e \mathbb{E}\left[\int_A \mathbf{1}_{\{\Phi_b(b(\mathbf{x},r))>0\}} d\mathbf{x}\right] \\
&= \lambda_e \int_A P(\Phi_b(b(\mathbf{x},r)) > 0) d\mathbf{x} \\
&= \lambda_e \int_A P(\Phi_b(b(o,r)) > 0) d\mathbf{x} \\
&= \lambda_e |A| H_b(r).
\end{aligned} \tag{2.24}$$

Equation (2.24) then implies that,

$$P(B \le r) = 1 - \mathrm{e}^{-\lambda_b \pi r^2}, \tag{2.25}$$

see e.g. [16].

3 Stienen Model generated by Φ_b

In this section we present results when Θ is the Stienen model having the points of Φ_b as generators in a way which will be described below. This special case is of interest in connection with the ENF patterns since it induces a hierarchical structure between the ending process and the base process. This model allows for different intensities close to the base points than in more periferal parts of respective Voronoi cell. The Stienen model is defined as follows. For each $\mathbf{x} \in \Phi_b$, assign the following mark

$$R_{\mathbf{x}} = \min_{\mathbf{y} \in \Phi_b \,:\, \mathbf{y} \neq \mathbf{x}} \{ ||\mathbf{x} - \mathbf{y}||/2 \}.$$

Then, the random closed set

$$\mathcal{S} = \bigcup_{\mathbf{x} \in \Phi_b} b(\mathbf{x}, R_{\mathbf{x}}), \tag{3.1}$$

is called the Stienen model [15]. For a further introduction to the Stienen model the reader is referred to [16, 14, 10, 7]. Furthermore, let $\mathcal{S}_o$ denote the typical disk (meaning the disk that has the origin as centre) and R_o represents the typical mark. It is well known that the area fraction of the Stienen model is $p = \frac{1}{4}$ which implies using (2.2) and (2.3) that

$$\lambda_e = \frac{\lambda_1 + 3\lambda_2}{4}, \tag{3.2}$$

and

$$g_e(r) = \frac{1}{\lambda_e^2}[C_{\mathcal{S}}(r)(\lambda_1 - \lambda_2)^2 + \frac{1}{2}(\lambda_1 - \lambda_2)\lambda_2 + \lambda_2^2], \tag{3.3}$$

where $C_{\mathcal{S}}(r)$ is the covariance function of the Stienen model. In Schlather and Stoyan [14], the authors investigate the covariance of the Stienen model in general dimensions. They produce integral expressions for $C_{\mathcal{S}}(r)$ and obtain an analytical formula on the line. Furthermore, they produce numerical estimates for $d = 3$. Doing the same for $d = 2$ would make it possible to obtain a numerical estimate of $g_e(r)$.

3.1 Mark distributions

In this section we deduce the density of the individual branch length, i.e. the distance from a randomly chosen point in Φ_e to its nearest neighbor in Φ_b. If Θ and Φ_b are independent the density of the length an individual branch, denoted by B, is given by

$$f_B(x) = 2\pi\lambda_b r \mathrm{e}^{-\pi\lambda_b r^2}, \tag{3.4}$$

which follows from (2.25). However, if Θ and Φ_b are dependent, as in the case when $\Theta = \mathcal{S}$, then

$$f_{B_d}(x\,;\,\lambda_b) = \frac{p\lambda_1}{p\lambda_1 + (1-p)\lambda_2} f_{B_1}(x\,;\,\lambda_b) + \frac{(1-p)\lambda_2}{p\lambda_1 + (1-p)\lambda_2} f_{B_2}(x\,;\,\lambda_b), \tag{3.5}$$

where f_{B_Θ} and $f_{B_{\Theta^c}}$ denote the lengths of branches with endings in Θ and Θ^c, respectively. The weights represent the probability that the branch corresponds to a point lying in Θ or Θ^c, respectively. The expression for the weight associated with f_{B_Θ} can be derived by

$$\begin{aligned}
&\mathbb{E}\left[\frac{\Phi_1(\mathcal{V}_o)}{\Phi_1(\mathcal{V}_o) + \Phi_2(\mathcal{V}_o)}\right] \\
&\quad = \mathbb{E}\left[\mathbb{E}\left[\frac{\Phi_1(\mathcal{V}_o)}{\Phi_1(\mathcal{V}_o) + \Phi_2(\mathcal{V}_o)} \,\middle|\, \Theta, \Phi_b\right]\right] \\
&\quad = \mathbb{E}\left[\mathbb{E}\left[\mathbb{E}\left[\frac{\Phi_1(\mathcal{V}_o)}{\Phi_1(\mathcal{V}_o) + \Phi_2(\mathcal{V}_o)} \,\middle|\, \Phi_1(\mathcal{V}_o) + \Phi_2(\mathcal{V}_o), \Theta, \Phi_b\right] \,\middle|\, \Theta, \Phi_b\right]\right] \\
&\quad = \mathbb{E}\left[\mathbb{E}\left[\frac{\mathbb{E}\left[\Phi_1(\mathcal{V}_o) \,\middle|\, \Phi_1(\mathcal{V}_o) + \Phi_2(\mathcal{V}_o), \Theta, \Phi_b\right]}{\Phi_1(\mathcal{V}_o) + \Phi_2(\mathcal{V}_o)} \,\middle|\, \Theta, \Phi_b\right]\right] \\
&\quad = \mathbb{E}\left[\frac{\lambda_1 |\mathcal{V}_o \cap \Theta|}{\lambda_1 |\mathcal{V}_o \cap \Theta| + \lambda_2 |\mathcal{V}_o \cap \Theta^c|}\right].
\end{aligned} \tag{3.6}$$

The last equality follows from that for independent Poisson distributed random variables U, V with intensities λ_U and λ_V, respectively, the conditional distribution of $U \mid U + V$ is binomial with parameters $U + V$ and $\frac{\lambda_U}{\lambda_U + \lambda_V}$. Using Jensen's inequality gives

$$\begin{aligned}
\mathbb{E}\left[\frac{\lambda_1 |\mathcal{V}_o \cap \Theta|}{\lambda_1 |\mathcal{V}_o \cap \Theta| + \lambda_2 |\mathcal{V}_o \cap \Theta^c|}\right] \leq & \frac{\lambda_1}{\lambda_1 - \lambda_2 + \lambda_2 \mathbb{E}\left[\frac{|\mathcal{V}_o|}{|\mathcal{V}_o \cap \Theta|}\right]} \\
= & \frac{p\lambda_1}{p\lambda_1 + (1-p)\lambda_2},
\end{aligned} \tag{3.7}$$

where the last equality follows from that on average $p|\mathcal{V}_o| = |\mathcal{V}_o \cap \Theta|$. Analogous arguments give that

$$\mathbb{E}\left[\frac{\lambda_2 |\mathcal{V}_o \cap \Theta^c|}{\lambda_1 |\mathcal{V}_o \cap \Theta| + \lambda_2 |\mathcal{V}_o \cap \Theta^c|}\right] \leq \frac{(1-p)\lambda_2}{p\lambda_1 + (1-p)\lambda_2}, \tag{3.8}$$

and since the expected values sum to one, (3.7) and (3.8) imply that

$$\mathbb{E}\left[\frac{\lambda_1|\mathcal{V}_o\cap\Theta|}{\lambda_1|\mathcal{V}_o\cap\Theta|+\lambda_2|\mathcal{V}_o\cap\Theta^c|}\right] = \frac{p\lambda_1}{p\lambda_1+(1-p)\lambda_2}. \tag{3.9}$$

Now, $\Theta = \mathcal{S}$, $B_1 = B_{\mathcal{S}}$ and $B_2 = B_{\mathcal{S}^c}$ and we will derive the form of $f_{B_{\mathcal{S}}}$ and $f_{B_{\mathcal{S}^c}}$, respectively. The distribution function of R_o is given by $F_{R_o}(r) = 1 - \mathrm{e}^{-\lambda_b\pi 4r^2}$ since $R_o > r$ is equivalent to $\Phi_b \cap b(o, 2r) = \emptyset$. Furthermore, conditionally on R_o the density of the length of an individual branch belonging to an ending not lying in $\mathcal{S}$ is given by

$$f_{B_{\mathcal{S}^c}|R_o}(x|\lambda_b, R_o = r) = 2\lambda_b\pi x\,\mathrm{e}^{-\lambda_b\pi\left(x^2-r^2\right)}\mathbf{1}_{\{x\geq r\}}. \tag{3.10}$$

This means that

$$f_{B_{\mathcal{S}^c}}(x|\lambda_b) = \frac{8}{3}\pi\lambda_b x\,\mathrm{e}^{-\lambda_b\pi x^2}\left(1-\mathrm{e}^{-3\pi\lambda_b x^2}\right). \tag{3.11}$$

Furthermore, the branch length from an ending point inside $\mathcal{S}$ has the density

$$f_{B_{\mathcal{S}}}(x|\lambda_b) = 8\pi\lambda_b x\,\mathrm{e}^{-4\lambda_b\pi x^2}. \tag{3.12}$$

A plot of f_B, $f_{B_{\mathcal{S}}}$ and $f_{B_{\mathcal{S}^c}}$ can be seen in Figure 2. Further, by (3.5) we have

$$\begin{aligned} f_{B_d}(x\,;\,\lambda_b) &= \frac{\lambda_1}{\lambda_1+3\lambda_2}f_{B_{\mathcal{S}}}(x\,;\,\lambda_b) + \frac{3\lambda_2}{\lambda_1+3\lambda_2}f_{B_{\mathcal{S}^c}}(x\,;\,\lambda_b) \\ &= \frac{8\pi\lambda_b\,x}{\lambda_1+3\lambda_2}\,\mathrm{e}^{-\pi\lambda_b x^2}\left(\lambda_2+(\lambda_1-\lambda_2)\,\mathrm{e}^{-3\pi\lambda_b x^2}\right), \end{aligned} \tag{3.13}$$

which gives $\mathbb{E}[B_d] = \frac{\lambda_1+7\lambda_2}{4(\lambda_1+3\lambda_2)\sqrt{\lambda_b}}$. Let $N_{\mathcal{S}}$ be the analogue of N defined in (2.5) when $\Theta = \mathcal{S}$, i.e.

$$N_{\mathcal{S}} = \sum_{\mathbf{x}\in\Phi_1}\mathbf{1}_{\mathcal{S}_o}(\mathbf{x}).$$

We have that

$$P(|\mathcal{S}_o| > r) = P\left(R_o > \sqrt{\frac{r}{\pi}}\right),$$

meaning that $|\mathcal{S}_o| \sim \mathrm{Exp}(4\lambda_b)$. It then follows that

$$f_{N_{\mathcal{S}}}(n\,;\,\lambda_b,\lambda_1) = \frac{4\lambda_b}{4\lambda_b+\lambda_1}\left(\frac{\lambda_1}{\lambda_1+4\lambda_b}\right)^n. \tag{3.14}$$

Furthermore,

$$L_{\mathcal{S}} \overset{\mathcal{D}}{=} \sum_{j=1}^{N} B_{1,j}, \tag{3.15}$$

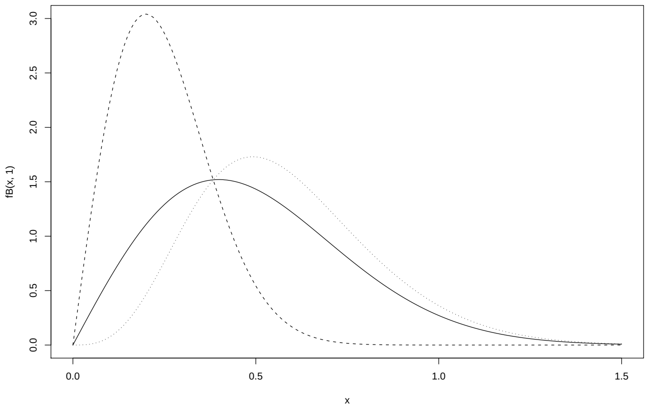

Figure 2: *Left: Plot of the densities for individual branch lengths,* f_B *(solid line),* $f_{B_{\mathcal{S}}}$ *(dashed line) and* $f_{B_{\mathcal{S}^c}}$ *(dotted line). In all three cases* $\lambda_b = 1$. *Right: Plot of* $f_{\tilde{B}}$ *based on* (3.13).

where $B_{1,1}, B_{1,2}, ...$ is an i.i.d. sequence of random variables having the density given in (3.12). Conditionally on $N = n$, for $n \geq 1$, we have that

$$\begin{aligned} & f_{L_{\mathcal{S}} \mid N_{\mathcal{S}}=n}(x\,;\,\lambda_b, n) \\ &= \int_0^x ... \int_0^{y_2} f_{B_1}(x - y_{n-1}) f_{B_1}(y_{n-1} - y_{n-2}) ... f_{B_1}(y_2 - y_1) f_{B_1}(y_1) dy_{n-1} ... dy_1, \end{aligned} \tag{3.16}$$

and then the unconditional density is given by

$$\begin{aligned} f_{L_{\mathcal{S}}}(x\,;\,\lambda_b, \lambda_e) = \mathbf{1}_{\{x=0\}} & \frac{4\lambda_b}{4\lambda_b + \lambda_1} \\ & + \mathbf{1}_{\{x>0\}} \frac{4\lambda_b}{4\lambda_b + \lambda_1} \sum_{n=1}^{\infty} f_{L \mid N=n}(x\,;\,\lambda_b, n) \left(\frac{\lambda_1}{\lambda_1 + 4\lambda_b} \right)^n . \end{aligned} \tag{3.17}$$

A plot of numerical estimates of $f_{L \mid N=n}(x\,;\,1, n)$ for $n = 1, ..., 5$, and $f_L(x\,;\,1, 2)$ are displayed in Figure 3. The above is not possible to do for neither $N_{\mathcal{S}^c}$ nor $L_{\mathcal{S}^c}$, since we do not know the distribution of $|\mathcal{V}_o \backslash \mathcal{S}_o|$.

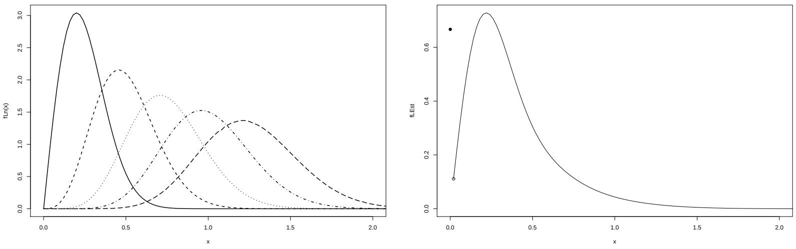

Figure 3: *Left: Plot of numerical estimate of* $f_{L_{\mathcal{S}}\,|\,N_{\mathcal{S}}=n}(x\,;\,1,n)$*,* $n = 1$ *(solid),* $n = 2$ *(dashed),* $n = 3$ *(dotted),* $n = 4$ *(dashed-dotted), ,* $n = 5$ *(long dashed), using* (3.16)*. Right: Plot of numerical estimate of* $f_{L_{\mathcal{S}}}(x\,;\,1,2)$ *using* (3.17).

Means, variances and covariances

In this section we present integral formulas for the first two moments of Σ_f and also numerical estimates of these for N and L.

Definition 2. *For a measurable function* $f : \mathbb{R}^2 \to \mathbb{R}_+$ *define*

$$\Sigma_f^1 = \sum_{\mathbf{x}\in\Phi_1} f(\mathbf{x})\mathbf{1}_{\mathcal{S}_o}(\mathbf{x}), \tag{3.18}$$

and

$$\Sigma_f^2 = \sum_{\mathbf{x}\in\Phi_2} f(\mathbf{x})\mathbf{1}_{\mathcal{V}_o\cap\mathcal{S}^c}(\mathbf{x}). \tag{3.19}$$

Elementary we can write $\Sigma_f = \Sigma_f^1 + \Sigma_f^2$, which will be used in the following.

Proposition 2. *For any measurable function* $f : \mathbb{R}^2 \to \mathbb{R}_+$ *the following assertion holds*

$$\mathbb{E}[\Sigma_f] = \int_{\mathbb{R}^2} f(\mathbf{x})\mathrm{e}^{-\lambda_b\pi|\mathbf{x}|^2}\left[\lambda_2 + (\lambda_1-\lambda_2)\mathrm{e}^{-\lambda_b 3\pi|\mathbf{x}|^2}\right]d\mathbf{x}. \tag{3.20}$$

Specifically we have that

$$\mathbb{E}[N] = \frac{\lambda_1 + 3\lambda_2}{4\lambda_b}, \tag{3.21}$$

and

$$\mathbb{E}[L] = \frac{\lambda_1 + 7\lambda_2}{16\lambda_b^{\frac{3}{2}}}. \tag{3.22}$$

Proof. We have that

$$\begin{aligned}\mathbb{E}\left[\Sigma_f^1\right] &= \lambda_1 \int_{\mathbb{R}^2} f(\mathbf{x}) P(\mathbf{x} \in \mathcal{V}_o \cap \mathcal{S}) d\mathbf{x} = \lambda_1 \int_{\mathbb{R}^2} f(\mathbf{x}) P(R_o \geq |\mathbf{x}|) d\mathbf{x} \\ &= \lambda_1 \int_{\mathbb{R}^2} f(\mathbf{x}) \mathrm{e}^{-4\pi\lambda_b |\mathbf{x}|^2} d\mathbf{x}. \end{aligned} \tag{3.23}$$

Furthermore,

$$\mathbb{E}\left[\Sigma_f^2\right] = \lambda_2 \int_{\mathbb{R}^2} f(\mathbf{x}) P(\mathbf{x} \in \mathcal{V}_o,\, R_o < |\mathbf{x}|) d\mathbf{x}, \tag{3.24}$$

since $\mathbf{x} \in \mathcal{S}^c$ is equivalent to $R_o < |\mathbf{x}|$. We have that

$$P(\mathbf{x} \in \mathcal{V}_o,\, R_o < |\mathbf{x}|) = P(R_o < |\mathbf{x}| \,|\, \mathbf{x} \in \mathcal{V}_o) P(\mathbf{x} \in \mathcal{V}_o), \tag{3.25}$$

and

$$P(R_{\mathbf{o}} < |\mathbf{x}|) = P(R_o < |\mathbf{x}| \,|\, \mathbf{x} \in \mathcal{V}_o) P(\mathbf{x} \in \mathcal{V}_o) + P(R_o < |\mathbf{x}| \,|\, \mathbf{x} \in \mathcal{V}_o^c) P(\mathbf{x} \in \mathcal{V}_o^c),$$

Now, it is readily seen that $P(R_o < |\mathbf{x}| \,|\, \mathbf{x} \in \mathcal{V}_o^c) = 1$, since the radius of the largest circle contained in the typical cell, centered at the generator, is always less than the distance to any point outside the typical cell. This means that

$$P(\mathbf{x} \in \mathcal{V}_o,\, R_o < |\mathbf{x}|) \quad = \quad P(R_{\mathbf{o}} < |\mathbf{x}|) - P(\mathbf{x} \in \mathcal{V}_o^c). \tag{3.26}$$

We have that $P(\mathbf{x} \in \mathcal{V}_o^c) = 1 - \mathrm{e}^{-\lambda_b \pi |\mathbf{x}|^2}$, since a point $\mathbf{x}$ belongs to the typical cell iff there are no points of the process Φ_b in $b(\mathbf{x}, |\mathbf{x}|)$, meaning that $P(\mathbf{x} \in \mathcal{V}_o) = \mathrm{e}^{-\lambda_b \pi |\mathbf{x}|^2}$. Inserting these into equation (3.26) and then into Equation (3.24) completes the proof.

□

Furthermore, concerning second moments we will use that

$$\begin{aligned}\mathrm{Cov}\left(\Sigma_{f_1}, \Sigma_{f_2}\right) &= \mathrm{Cov}\left(\Sigma_{f_1}^1, \Sigma_{f_2}^1\right) + \mathrm{Cov}\left(\Sigma_{f_1}^2, \Sigma_{f_2}^2\right) \\ &\quad + \mathrm{Cov}\left(\Sigma_{f_1}^1, \Sigma_{f_2}^2\right) + \mathrm{Cov}\left(\Sigma_{f_2}^1, \Sigma_{f_1}^2\right). \end{aligned} \tag{3.27}$$

The covariances on the right-hand side fort this Stienen model construction will be given in Lemmas 2,3 and 4.

LEMMA 2. *For any measurable functions $f_1, f_2 : \mathbb{R}^2 \to \mathbb{R}_+$, we have that*

$$\begin{aligned}
\mathrm{Cov}\left(\Sigma_{f_1}^2, \Sigma_{f_2}^2\right) \;=\; & \lambda_2 \int_{\mathbb{R}^2} f_1(\mathbf{x}) f_2(\mathbf{x}) \mathrm{e}^{-\lambda_b \pi |\mathbf{x}|^2} \left(1 - \mathrm{e}^{-3\lambda_b \pi |\mathbf{x}|^2}\right) d\mathbf{x} \\
& + \lambda_2^2 \int_{\mathbb{R}^2} \int_{\mathbb{R}^2} f_1(\mathbf{x}_1) f_2(\mathbf{x}_2) \mathrm{e}^{-\lambda_b U(\mathbf{x}_1, \mathbf{x}_2)} d\mathbf{x}_1 d\mathbf{x}_2. \\
& - \lambda_2^2 \iint_{|\mathbf{x}_1| \leq |\mathbf{x}_2|} f_1(\mathbf{x}_1) f_2(\mathbf{x}_2) \mathrm{e}^{-\lambda_b V(\mathbf{x}_1, \mathbf{x}_2)} d\mathbf{x}_1 d\mathbf{x}_2 \\
& - \lambda_2^2 \iint_{|\mathbf{x}_1| \leq |\mathbf{x}_2|} f_2(\mathbf{x}_1) f_1(\mathbf{x}_2) \mathrm{e}^{-\lambda_b V(\mathbf{x}_1, \mathbf{x}_2)} d\mathbf{x}_1 d\mathbf{x}_2 \\
& - \lambda_2^2 \int_{\mathbb{R}^2} \int_{\mathbb{R}^2} f_1(\mathbf{x}_1) f_2(\mathbf{x}_2) \mathrm{e}^{-\lambda_b \pi (|\mathbf{x}_1|^2 + |\mathbf{x}_2|^2)} d\mathbf{x}_1 d\mathbf{x}_2 \\
& - \lambda_2^2 \int_{\mathbb{R}^2} \int_{\mathbb{R}^2} f_1(\mathbf{x}_1) f_2(\mathbf{x}_2) \mathrm{e}^{-4\lambda_b \pi (|\mathbf{x}_1|^2 + |\mathbf{x}_2|^2)} d\mathbf{x}_1 d\mathbf{x}_2 \\
& + \lambda_2^2 \int_{\mathbb{R}^2} \int_{\mathbb{R}^2} f_1(\mathbf{x}_1) f_2(\mathbf{x}_2) \mathrm{e}^{-\lambda_b \pi (4|\mathbf{x}_1|^2 + |\mathbf{x}_2|^2)} d\mathbf{x}_1 d\mathbf{x}_2 \\
& + \lambda_2^2 \int_{\mathbb{R}^2} \int_{\mathbb{R}^2} f_1(\mathbf{x}_1) f_2(\mathbf{x}_2) \mathrm{e}^{-\lambda_b \pi (|\mathbf{x}_1|^2 + 4|\mathbf{x}_2|^2)} d\mathbf{x}_1 d\mathbf{x}_2
\end{aligned}$$

where $U(\mathbf{x}_1, \mathbf{x}_2)$ is defined in Theorem 1 and $V(\mathbf{x}_1, \mathbf{x}_2)$ is the area of the union of two disks centered at o and $\mathbf{x}_2$ and having radii $2|\mathbf{x}_1|$ and $|\mathbf{x}_2|$,respectively.

Proof. The proof follows the same lines as the proof of Theorem 1, and then we need to find

$$P(\mathbf{x}_1, \mathbf{x}_2 \in \mathcal{V}_o \cap \mathcal{S}^c) = P(R_o < |\mathbf{x}_1|, R_o < |\mathbf{x}_2|, \, \mathbf{x}_1, \mathbf{x}_2 \in \mathcal{V}_o).$$

This will be solved for $\mathbf{x}_1, \mathbf{x}_2$ s.t. $|\mathbf{x}_1| \leq |\mathbf{x}_2|$ and for $\mathbf{x}_1, \mathbf{x}_2$ s.t. $|\mathbf{x}_1| > |\mathbf{x}_2|$ respectively. For $|\mathbf{x}_1| \leq |\mathbf{x}_2|$

$$P(R_o < |\mathbf{x}_1|, R_o < |\mathbf{x}_2|, \, \mathbf{x}_1, \mathbf{x}_2 \in \mathcal{V}_o) = P(R_o < |\mathbf{x}_1|, \, \mathbf{x}_1, \mathbf{x}_2 \in \mathcal{V}_o).$$

Further, it holds that

$$P(\mathbf{x}_1, \mathbf{x}_2 \in \mathcal{V}_o) = P(R_o < |\mathbf{x}_1|, \, \mathbf{x}_1, \mathbf{x}_2 \in \mathcal{V}_o) + P(R_o \geq |\mathbf{x}_1|, \, \mathbf{x}_1, \mathbf{x}_2 \in \mathcal{V}_o).$$

Now, $P(\mathbf{x}_1, \mathbf{x}_2 \in \mathcal{V}_o) = \mathrm{e}^{-\lambda_b U(\mathbf{x}_1, \mathbf{x}_2)}$ since the points $\mathbf{x}_1$, $\mathbf{x}_2$ lie in $\mathcal{V}_o$ iff there are no points of Φ_b in $b(\mathbf{x}_1, |\mathbf{x}_1|) \cup b(\mathbf{x}_2, |\mathbf{x}_2|)$. Furthermore, $R_o > |\mathbf{x}_1| \cap \mathbf{x}_1, \mathbf{x}_2 \in \mathcal{V}_o$ is equivalent to $\Phi_b \cap (b(o, 2|\mathbf{x}_1|) \cup b(\mathbf{x}_2, |\mathbf{x}_2|)) = \emptyset$, which means that $P(R_o \geq |\mathbf{x}_1|, \, \mathbf{x}_1, \mathbf{x}_2 \in \mathcal{V}_o) = \mathrm{e}^{-\lambda_b V(\mathbf{x}_1, \mathbf{x}_2)}$. This completes the proof. □

REMARK 1. *The function $V(\mathbf{x}_1,\mathbf{x}_2)$ is given by*

$$\begin{aligned} V(\mathbf{x}_1,\mathbf{x}_2) &= 4|\mathbf{x}_1|^2\left[\pi-\arccos\left(\frac{|\mathbf{x}_1|}{|\mathbf{x}_2|}\right)\right]+2|\mathbf{x}_1|\sqrt{|\mathbf{x}_2|^2-|\mathbf{x}_1|^2} \\ &\quad +|\mathbf{x}_2|^2\left[\pi-\arccos\left(\frac{|\mathbf{x}_2|^2-2|\mathbf{x}_1|^2}{|\mathbf{x}_2|^2}\right)\right], \end{aligned}$$

which can be obtained by using Equation (K.1) in [17].

In order to obtain numerical values for the integrals above we need to estimate

$$\mathcal{I}(f_1,f_2,\lambda_b)=\int_{\mathbb{R}^2}\int_{\mathbb{R}^2} f_1(\mathbf{x}_1)f_2(\mathbf{x}_2)\mathrm{e}^{-\lambda_b U(\mathbf{x}_1,\mathbf{x}_2)}d\mathbf{x}_1 d\mathbf{x}_2,$$

and

$$\mathcal{J}(f_1,f_2,\lambda_b)=\iint_{|\mathbf{x}_1|\le|\mathbf{x}_2|} f_1(\mathbf{x}_1)f_2(\mathbf{x}_2)\mathrm{e}^{-\lambda_b V(\mathbf{x}_1,\mathbf{x}_2)}d\mathbf{x}_1 d\mathbf{x}_2,$$

for $f_i(\mathbf{x}_i)=1$ and $f_i(\mathbf{x}_i)=|\mathbf{x}_i|$, $i=1,2$. These are displayed in Table 1.

f_1, f_2	$\mathcal{I}(f_1,f_2,\lambda_b)$	$\mathcal{J}(f_1,f_2,\lambda_b)$
$f_1(\mathbf{x}_1)=f_2(\mathbf{x}_2)=1$	$1.280\lambda_b^{-2}$	$0.281\lambda_b^{-2}$
$f_1(\mathbf{x}_1)=1$, $f_2(\mathbf{x}_2)=\lvert\mathbf{x}_2\rvert$	$0.698\lambda_b^{-\frac{3}{2}}$	$0.168\lambda_b^{-\frac{3}{2}}$
$f_1(\mathbf{x}_1)=\lvert\mathbf{x}_1\rvert$, $f_2(\mathbf{x}_2)=1$	$0.698\lambda_b^{-\frac{3}{2}}$	$0.073\lambda_b^{-\frac{3}{2}}$
$f_i(\mathbf{x}_i)=f_i(\mathbf{x}_i)=\lvert\mathbf{x}_i\rvert$, $i=1,2$	$0.397\lambda_b^{-3}$	$0.047\lambda_b^{-3}$

Table 1: *Numerical estimates of $\mathcal{I}(f_1,f_2,\lambda_b)$ and $\mathcal{J}(f_1,f_2,\lambda_b)$.*

The integral $\mathcal{I}(f_1,f_2,\lambda_b)$ is approximated by the technique suggested in [2]. The values for $\mathcal{J}(f_1,f_2,\lambda_b)$ are obtained in an analogous way. We will briefly display the method for $f_i(\mathbf{x}_i)=f_i(\mathbf{x}_i)=|\mathbf{x}_i|$, $i=1,2$. Let $r_1=|\mathbf{x}_1|$, $r_2=|\mathbf{x}_2|$ and further denote the interior angles of the triangle $o\mathbf{x}_1\mathbf{x}_2$ by α_1 and α_2 respectively (see Figure 4 below). We then have that $\frac{r_1}{r_2}=\frac{\sin\alpha_2}{\sin\alpha_1}$ and by using Remark 1 it follows that

$$\begin{aligned} V(\mathbf{x},\mathbf{y}) = S_3(r_1,r_2,\theta) &= 4r_1^2\left[\pi-\cos^{-1}\left(\frac{\sin\alpha_2}{\sin\alpha_1}\right)\right] \\ &\quad + r_2^2\left[\pi-\cos^{-1}\left(1-2\frac{\sin^2\alpha_2}{\sin^2\alpha_1}\right)\right]+2r_1r_2\sqrt{1-\frac{\sin^2\alpha_2}{\sin^2\alpha_1}}. \qquad (3.28) \end{aligned}$$

Using Equation 3.28, we have that

$$\begin{aligned}&\iint_{|\mathbf{x}_1|\leq|\mathbf{x}_2|}|\mathbf{x}_1||\mathbf{x}_2|\mathrm{e}^{-\lambda_b V(\mathbf{x}_1,\mathbf{x}_2,2)}d\mathbf{x}_1 d\mathbf{x}_2\\&=2\pi\int_0^{\infty}\int_0^{r_2}\int_0^{\pi}r_1^2 r_2^2\mathrm{e}^{-\lambda_b S_3(r_1,r_2,\theta)}d\theta dr_1 dr_2=2\pi I_3.\end{aligned}$$

Now, regard the following change of variables $(r_1, r_2, \theta) \mapsto (D\sin u, D\sin v, \pi - u - v)$, giving the Jacobian $\mathcal{J} = D\sin(u+v)$. A graphical explanation of this change of variables is displayed in Figure 4. It follows that $\alpha_1 = \pi - \beta_1 = v$ and $\alpha_2 = \pi - \beta_2 = u$.

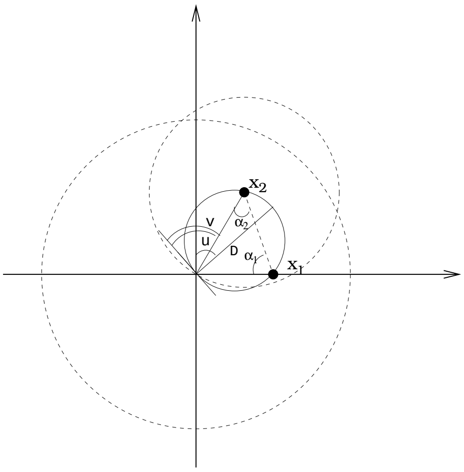

Figure 4: *Graphical explanation of the change of variables used.*

This means that

$$V(\mathbf{x}_1, \mathbf{x}_2) = D^2 K(u, v) \tag{3.29}$$

where

$$\begin{aligned}K(u,v) = 4\sin^2 u\left[\pi - \cos^{-1}\left(\frac{\sin u}{\sin v}\right)\right] + \sin^2 v\left[\pi - \cos^{-1}\left(1 - 2\frac{\sin^2 u}{\sin^2 v}\right)\right]\\ + 2\sin u\sin v\sqrt{1 - \frac{\sin^2 u}{\sin^2 v}}.\end{aligned}$$

Lastly,

$$
\begin{aligned}
I_3 &= \int_0^{\frac{\pi}{2}} \int_u^{\pi-u} \int_0^{\infty} D^5 \sin^2 u \sin^2 v \sin{(u+v)} \mathrm{e}^{-\lambda_b D^2 K(u,v)} dD dv du \\
&= \frac{1}{\lambda_b^3} \int_0^{\pi} \int_u^{\pi-u} \frac{\sin^2 u \sin^2 v \sin{(u+v)}}{K(u,v)^3} dv du \approx \frac{0.0075}{\lambda_b^3}. \qquad (3.30)
\end{aligned}
$$

Using Table 1 it is possible to obtain the following numerical estimates for $N_{\mathcal{S}^c}$ and $L_{\mathcal{S}^c}$

$$
\begin{aligned}
\mathrm{Var}(N_{\mathcal{S}^c}) &\approx \frac{3\lambda_2}{4\lambda_b} + 0.156\frac{\lambda_2^2}{\lambda_b^2}, \\
\mathrm{Var}(L_{\mathcal{S}^c}) &\approx \frac{15\lambda_2}{16\pi\lambda_b^2} + 0.112\frac{\lambda_2^2}{\lambda_b^3}, \\
\mathrm{Cov}(N_{\mathcal{S}^c}, L_{\mathcal{S}^c}) &\approx \frac{7\lambda_2}{16\lambda_b^{\frac{3}{2}}} + 0.129\frac{\lambda_2^2}{\lambda_b^{\frac{5}{2}}}.
\end{aligned}
$$

LEMMA 3.

$$
\begin{aligned}
\mathrm{Cov}\left(\Sigma_{f_1}^1, \Sigma_{f_2}^2\right) &= \lambda_1\lambda_2 \iint_{|\mathbf{x}_1| \leq |\mathbf{x}_2|} f_1(\mathbf{x}_1) f_2(\mathbf{x}_2) \mathrm{e}^{-\lambda_b V(\mathbf{x}_1, \mathbf{x}_2)} d\mathbf{x}_1 d\mathbf{x}_2 \\
&- \lambda_1\lambda_2 \iint_{|\mathbf{x}_1| \leq |\mathbf{x}_2|} f_1(\mathbf{x}_1) f_2(\mathbf{x}_2) \mathrm{e}^{-4\pi\lambda_b |\mathbf{x}_2|^2} d\mathbf{x}_1 d\mathbf{x}_2 \\
&- \lambda_1\lambda_2 \int_{\mathbb{R}^2} \int_{\mathbb{R}^2} f_1(\mathbf{x}_1) f_2(\mathbf{x}_2) \mathrm{e}^{-\pi\lambda_b (4|\mathbf{x}_1|^2 + |\mathbf{x}_2|^2)} d\mathbf{x}_1 d\mathbf{x}_2 \\
&+ \lambda_1\lambda_2 \int_{\mathbb{R}^2} \int_{\mathbb{R}^2} f_1(\mathbf{x}_1) f_2(\mathbf{x}_2) \mathrm{e}^{-4\pi\lambda_b (|\mathbf{x}_1|^2 + |\mathbf{x}_2|^2)} d\mathbf{x}_1 d\mathbf{x}_2 \qquad (3.31)
\end{aligned}
$$

and

$$
\begin{aligned}
\mathrm{Cov}\left(\Sigma_{f_2}^1, \Sigma_{f_1}^2\right) &= \lambda_1\lambda_2 \iint_{|\mathbf{x}_1| \leq |\mathbf{x}_2|} f_2(\mathbf{x}_1) f_1(\mathbf{x}_2) \mathrm{e}^{-\lambda_b V(\mathbf{x}_1, \mathbf{x}_2)} d\mathbf{x}_1 d\mathbf{x}_2 \\
&- \lambda_1\lambda_2 \iint_{|\mathbf{x}_1| \leq |\mathbf{x}_2|} f_2(\mathbf{x}_1) f_1(\mathbf{x}_2) \mathrm{e}^{-4\pi\lambda_b |\mathbf{x}_2|^2} d\mathbf{x}_1 d\mathbf{x}_2 \\
&- \lambda_1\lambda_2 \int_{\mathbb{R}^2} \int_{\mathbb{R}^2} f_2(\mathbf{x}_1) f_1(\mathbf{x}_2) \mathrm{e}^{-\pi\lambda_b (4|\mathbf{x}_1|^2 + |\mathbf{x}_2|^2)} d\mathbf{x}_1 d\mathbf{x}_2 \\
&+ \lambda_1\lambda_2 \int_{\mathbb{R}^2} \int_{\mathbb{R}^2} f_2(\mathbf{x}_1) f_1(\mathbf{x}_2) \mathrm{e}^{-4\pi\lambda_b (|\mathbf{x}_1|^2 + |\mathbf{x}_2|^2)} d\mathbf{x}_1 d\mathbf{x}_2 \qquad (3.32)
\end{aligned}
$$

Proof. We will prove (3.31). The proof of (3.32) follows similar arguments. For $|\mathbf{x}_1| > |\mathbf{x}_2|$ we have that $P(\mathbf{x}_1 \in \mathcal{V}_o \cap \mathcal{S}, \mathbf{x}_2 \in \mathcal{V}_o \cap \mathcal{S}^c) = 0$. Concerning $|\mathbf{x}_1| \leq |\mathbf{x}_2|$, we first identify that

$$P(\mathbf{x}_1 \in \mathcal{V}_o \cap \mathcal{S}, \mathbf{x}_2 \in \mathcal{V}_o \cap \mathcal{S}^c) = P(R_o \geq |\mathbf{x}_1|, R_o < |\mathbf{x}_2|, \mathbf{x}_2 \in \mathcal{V}_o),$$

and further

$$\begin{aligned} P(R_o \geq |\mathbf{x}_1|, \mathbf{x}_2 \in \mathcal{V}_o) &= P(R_o \geq |\mathbf{x}_1|, R_o \geq |\mathbf{x}_2|) \\ &\quad + P(R_o \geq |\mathbf{x}_1|, R_o < |\mathbf{x}_2|, \mathbf{x}_2 \in \mathcal{V}_o) \\ &= P(R_o \geq |\mathbf{x}_2|) + P(R_o \geq |\mathbf{x}_1|, R_o < |\mathbf{x}_2|, \mathbf{x}_2 \in \mathcal{V}_o), \end{aligned}$$

which implies that

$$\begin{aligned} P(R_o \geq |\mathbf{x}_1|, R_o < |\mathbf{x}_2|, \mathbf{x}_2 \in \mathcal{V}_o) &= P(R_o \geq |\mathbf{x}_1|, \mathbf{x}_2 \in \mathcal{V}_o) - P(R_o \geq |\mathbf{x}_2|) \\ &= \mathrm{e}^{-\lambda_b V(\mathbf{x}_1, \mathbf{x}_2)} - \mathrm{e}^{-4\pi\lambda_b |\mathbf{x}_2|^2}. \end{aligned}$$

□

Using Lemma 3 together with Table 1 we obtain the following numerical estimates for the covariances between $N_{\mathcal{S}}, N_{\mathcal{S}^c}, L_{\mathcal{S}}$ and $L_{\mathcal{S}^c}$, respectively.

$$\begin{aligned} \mathrm{Cov}(N_{\mathcal{S}}, N_{\mathcal{S}^c}) &\approx \; 0.031 \, \frac{\lambda_1 \lambda_2}{\lambda_b^2}, && (3.33) \\ \mathrm{Cov}(L_{\mathcal{S}}, L_{\mathcal{S}^c}) &\approx \; 0.013 \, \frac{\lambda_1 \lambda_2}{\lambda_b^3}, && (3.34) \\ \mathrm{Cov}(N_{\mathcal{S}}, L_{\mathcal{S}^c}) &\approx \; 0.035 \, \frac{\lambda_1 \lambda_2}{\lambda_b^{\frac{5}{2}}}, && (3.35) \\ \mathrm{Cov}(L_{\mathcal{S}}, N_{\mathcal{S}^c}) &\approx \; 0.0105 \, \frac{\lambda_1 \lambda_2}{\lambda_b^{\frac{5}{2}}}. && (3.36) \end{aligned}$$

LEMMA 4.

$$\begin{aligned} \mathrm{Cov}\left(\Sigma^1_{f_1}, \Sigma^1_{f_2}\right) = \lambda_1 & \int_{\mathbb{R}^2} f_1(\mathbf{x}) f_2(\mathbf{x}) \mathrm{e}^{-\lambda_b \pi \, 4|\mathbf{x}|^2} d\mathbf{x} \\ & + \lambda_1^2 \int_{\mathbb{R}^2} \int_{\mathbb{R}^2} f_1(\mathbf{x}_1) f_2(\mathbf{x}_2) \mathrm{e}^{-\lambda_b \pi \, 4 \max(|\mathbf{x}_1|^2, |\mathbf{x}_2|^2)} d\mathbf{x}_1 d\mathbf{x}_2, \\ & - \lambda_1^2 \int_{\mathbb{R}^2} \int_{\mathbb{R}^2} f_1(\mathbf{x}_1) f_2(\mathbf{x}_2) \mathrm{e}^{-\lambda_b \pi \, 4(|\mathbf{x}_1|^2 + |\mathbf{x}_2|^2)} d\mathbf{x}_1 d\mathbf{x}_2 \qquad (3.37) \end{aligned}$$

which implies that

$$\begin{aligned}
\mathrm{Var}(N_{\mathcal{S}}) &= \frac{\lambda_1}{4\lambda_b} + \frac{\lambda_1^2}{16\lambda_b^2}, \\
\mathrm{Var}(L_{\mathcal{S}}) &= \frac{\lambda_1}{16\pi\lambda_b^2} + \frac{256-24\pi}{6144\pi}\frac{\lambda_1^2}{\lambda_b^3}, \\
\mathrm{Cov}(N_{\mathcal{S}}, L_{\mathcal{S}}) &= \frac{\lambda_1}{16\lambda_b^{\frac{3}{2}}} + \frac{3\lambda_1^2}{128\lambda_b^{\frac{5}{2}}}.
\end{aligned}$$

The proof of Lemma 4 follows the same type of ideas as we used in the proof of Lemma 2, and using that

$$P(\mathbf{x}_1, \mathbf{x}_2 \in \mathcal{V}_o \cap \mathcal{S}) = P(\mathbf{x}_1, \mathbf{x}_2 \in \mathcal{S}) = \mathrm{e}^{-\lambda_b \pi\, 4 \max\left(|\mathbf{x}_1|^2, |\mathbf{x}_2|^2\right)}.$$

Combining Lemmas 2,3 and 4 and using the numerical approximations we obtain the following approximations of the variance and covariance of N and L.

$$\mathrm{Var}(N) \approx \frac{\lambda_e}{\lambda_b} + \frac{1}{\lambda_b^2}\left(\frac{1}{16}\lambda_1^2 + 0.156\lambda_2^2 + 0.062\lambda_1\lambda_2\right), \tag{3.38}$$

$$\mathrm{Var}(L) \approx \frac{\lambda_1 + 15\lambda_2}{16\pi\lambda_b} + \frac{1}{\lambda_b^3}\left(\frac{256-24\pi}{6144\pi}\lambda_1^2 + 0.112\lambda_2^2 + 0.026\lambda_1\lambda_2\right), \tag{3.39}$$

$$\mathrm{Cov}(N, L) \approx \frac{\lambda_1 + 7\lambda_2}{\lambda_b^{\frac{3}{2}}} + \frac{1}{\lambda_b^{\frac{5}{2}}}\left(\frac{3}{128}\lambda_1^2 + 0.129\lambda_2^2 + 0.0455\lambda_1\lambda_2\right). \tag{3.40}$$

REMARK 2. *By setting* $\lambda_1 = \lambda_2$ *in* (3.38), (3.39) *and* (3.40) *we obtain the same results as in [2].*

REMARK 3. *In this setting it is possible to obtain a numerical value for* $\mathrm{Cov}(|\mathcal{V}_o \cap \mathcal{S}|, |\mathcal{V}_o \cap \mathcal{S}^c|)$*, namely*

$$\mathrm{Cov}(|\mathcal{V}_o \cap \mathcal{S}|, |\mathcal{V}_o \cap \mathcal{S}^c|) = \mathrm{Cov}(|\mathcal{V}_o|, |\mathcal{S}_o|) - \frac{1}{16} \approx \frac{0.0310}{\lambda_b^2}, \tag{3.41}$$

where the first equality follows from the fact that $|\mathcal{V}_o \cap \mathcal{S}^c| = |\mathcal{V}_o| - |\mathcal{S}_o|$ *and* $\mathrm{Var}(|\mathcal{S}_o|) = \frac{1}{16}$*. The numerical approximation of* $\mathrm{Cov}(|\mathcal{V}_o|, |\mathcal{S}_o|)$ *can be obtained using the results in [10].*

3.2 Conditional Angle distribution

If we let Γ denote the angle between the x-axis and the branch connecting the typical base to a randomly chosen ending. The conditional distribution of Γ, given a realization of bases $(\Gamma|\Phi_b = \varphi)$ is one feature of interest in our ENF application: Given the locations of the bases, where would the process place branches? For $o \in \Phi_b$, Γ_o depends on the position of the nearest neighbors, $\mathbf{y}_1, ..., \mathbf{y}_n$, of o. This distribution will "favor" directions in which there is relatively more open area. Conditionally (on the base process) the position of a randomly chosen ending, X, connected to the origin has a uniform distribution over either $\mathcal{S}_o$ or $\tilde{\mathcal{V}}_o$, depending on whether the point lies in $\mathcal{S}$ or $\mathcal{S}^c$, respectively. Here $\tilde{\mathcal{V}}_o = \mathcal{V}_o \backslash \mathcal{S}_o$. The above means that X has the following density

$$f_X(\mathbf{x}|\Phi_b) = \frac{\lambda_1}{\lambda_1|\mathcal{S}_o| + \lambda_2|\tilde{\mathcal{V}}_o|}\mathbf{1}_{\mathcal{S}_o}(\mathbf{x}) + \frac{\lambda_2}{\lambda_1|\mathcal{S}_o| + \lambda_2|\tilde{\mathcal{V}}_o|}\mathbf{1}_{\tilde{\mathcal{V}}_o}(\mathbf{x}),\ \mathbf{x} \in \mathcal{V}_o. \tag{3.42}$$

This is a weighting of the two uniform distributions over $\mathcal{S}_o$ and $\tilde{\mathcal{V}}_o$. The weights are given by the probability that the point we pick is lying in respective region of the typical cell, and are derived analogously to the unconditional case in (3.6).

Now, if we express X in polar coordinates, i.e. $X = (R, \Gamma)$, we get the following density

$$f_{R,\Gamma}(r, \gamma|\Phi_b) = \frac{\lambda_1\, r}{\lambda_1|\mathcal{S}_o| + \lambda_2|\tilde{\mathcal{V}}_o|}\mathbf{1}_{r \le R_o}(r) + \frac{\lambda_2\, r}{\lambda_1|\mathcal{S}_o| + \lambda_2|\tilde{\mathcal{V}}_o|}\mathbf{1}_{R_o \le r \le r_m(\gamma)}(r), \tag{3.43}$$

where $r_m(\gamma)$ is the distance from the origin to the perimeter of $\mathcal{V}_o$ at an angle γ w.r.t. the x-axis. The density for Γ is then given by

$$\begin{aligned} f_\Gamma(\gamma|\Phi_b) &= \int_0^{r_{\mathrm{m}}(\gamma)} f_{R,\Gamma}(r, \gamma|\Phi_b)dr \\ &= \frac{(\lambda_1 - \lambda_2)|\mathcal{S}_o| + \lambda_2\pi\, r_{\mathrm{m}}(\gamma)^2}{2\pi(\lambda_1|\mathcal{S}_o| + \lambda_2|\tilde{\mathcal{V}}_o|)},\ 0 \le \gamma \le 2\pi. \end{aligned} \tag{3.44}$$

The part of the density arising from endings lying in $\mathcal{S}_o$ is uniform and then there is the more complex part coming from the points lying in $\tilde{\mathcal{V}}_o$, resulting in an irregulars, jagged shape. This can be seen in Figure 5.

4 Discussion

We have suggested a class of spatial point process models motivated by modelling ENF patterns. These models should be viewed as a first attempt to model ENF patterns. To

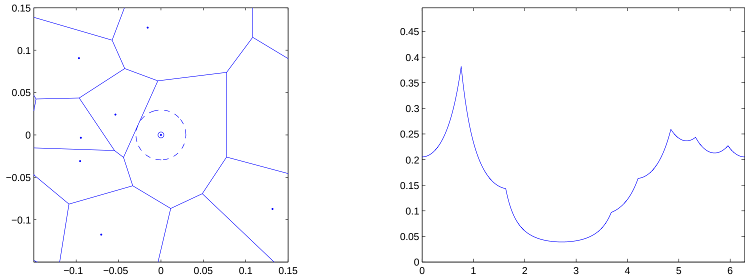

Figure 5: *Left: Realization of* $\mathcal{V}_o$. *Right: Conditional Angle Distribution of branches connected to the origin in the realization on the left, for* $\lambda_1 = 7$ *and* $\lambda_2 = 5$, $|\mathcal{S}_o| = 0.0027$ *and* $|\tilde{\mathcal{V}}_o| = 0.0117$.

capture more of the complexity of such patterns will most likely render in simulation based techniques. We have considered quantities such as number of branches per base, branch lengths and angles of the segments joining bases and their associated endings. Furthermore, we have considered the first and second moments of additive functionals which give the number of branches per base and total branch length per base as special cases. In the case of $\Theta = \mathcal{S}$, we have been able to obtain expressions for the density of the branch length as well as the conditional angle distribution (conditionally on the base process). We have also given integral formulas for the covariance between the area of the part of a random set which lies inside the typical Poisson-Voronoi cell and the area of the complement to the same random set which lies inside the typical Poisson-Voronoi cell.

References

[1] BØHM, P. AND SCHMIDT, V. (2003) *Palm representation and approximations of the covariance of a random closed set*, Adv. in Appl. Prob., **35**(2), pp. 295-302.

[2] FOSS, S. AND ZUYEV, S. (1996) *On a Voronoi Aggregative Process Related to a Bivariate Poisson Process*, Adv. Appl. Prob., 28, pp. 965-981.

[3] GILBERT, E.N. (1962) *Random subdivisions of space into crystals*, Ann. Math. Stat., 33, pp. 958-972.

[4] KENNEDY, W.R., AND WENDELSCHAFER-CRABB, G. (1993) *The innervation of human epidermis*, Journal of the Neurological Sciences **115**, 184-190.

[5] KENNEDY, W.R., WENDELSCHAFER-CRABB, G. AND JOHNSON, T. (1996) *Quantitation of epidermal nerves in diabetic neuropathy*, Neurology, **47**, 1042-1448.

[6] MCARTHUR, J.C., STOCKS, E.A., HAUER, P., CORNBLATH, D.R. AND GRIFFIN, J.W. (1998) *Epidermal nerve fiber density: Normative reference range and diagnostic efficiency*, Archives of Neurology, **55**, 1513-1520.

[7] MÅNSSON, M. (2007) *A connection between the volume fractions of the Stienen model and the dead leaves model*, Adv. in Appl. Prob., **39**(1), pp. 41-52.

[8] MØLLER, J. (1994) *Lectures on Random Voronoi Tessellations*, Springer-Verlag, New-York.

[9] MØLLER, J. SYVERSVEEN, A.R. AND WAAGEPETERSEN, R.P. (1998) *Log Gaussian Cox processes*, Scand. Journal. of Stat., **25**, pp. 451-482.

[10] OLSBO, V. (2007) *On the correlation between the volumes of the typical Poisson-Voronoi cell and the typical Stienen sphere*, Adv. Appl. Prob., **39**, pp. 883-892.

[11] PENTTINEN, A. AND NIEMI, A. (2007) *On Statistical Inference for the Random Set Generated Cox Process with Set-marking*, Biometrical Journal, **49**(2), pp. 197-213.

[12] ROBBINS, H.E. (1944) *On the measure of a random set I*, Annals of Math. Stat., **15**, pp. 70-74.

[13] ROBBINS, H.E. (1945) *On the measure of a random set II*, Annals of Math. Stat., **16**, pp. 342-347.

[14] SCHLATHER, M. AND STOYAN, D. (1997) *The covariance of the Stienen model*, In D. Jeulin (ed) Advances in Theory and Applications of Random Sets, Singapore. World Scientific, pp. 157-174.

[15] STIENEN H. (1982) *Die Vergroeberung von Karbiden in reinen Eisen-Kohlenstoff Stahlen*, Dissertation, RWTH Aachen.

[16] STOYAN D., KENDALL W.S. AND MECKE J. (1995) *Stochastic Geometry and its Applications, 2ed*, John Wiley & Sons.

[17] STOYAN D., AND STOYAN, H. (1994) *Fractals, Random Shapes and Point Fields*, John Wiley & Sons.

Paper III

Development and evaluation of spatial point process models of epidermal nerve fibers

Viktor Olsbo[1]* and Lance Waller[2]

[1] *Departement of Mathematical Statistics,*
Chalmers University of Technology, Gothenburg, Sweden

[2] *Department of Biostatistics and Bioinformatics, Rollings School of Public Health,*
Emory University, Atlanta, GA, U.S.A.

Abstract

We define two stochastic models describing the growth of branching systems, motivated by the growth and development of epidermal nerve fibers (ENFs) in human skin. The models derive from two point process, (Φ_b, Φ_e), describing the *base* and *ending* points of the fibers. Each point of Φ_e (the end point process) is connected to a unique point in Φ_b (the base point process). In the first model, both Φ_e and Φ_b are Poisson processes, yielding general baseline results. In the second model, we model the branching structure more directly by defining Φ_b as a general point process and Φ_e as a cluster process conditioned on the realization of Φ_b as its parent points. In both cases, we derive distributional properties for observable quantities of direct interest to neurologists such as the number, direction, and length of fibers for any particular base, conditional on the number and location of the other bases. We illustrate both models by fitting them to data arising from skin biopsy images of ENFs and provide inference regarding physiological properties of ENF growth.

Keywords: Angle Distribution; Branch length; Campbell Theorem; Epidermal nerve fibers; Poisson Process;

---

*Corresponding author; email: vikol@math.chalmers.se

1 Introduction

In this paper, we consider a set of two-stage point process models describing the following scenario: fibers represent branches and grow from "base" points to "ending" points under a process that encourages placement of "ending" points in current gaps in coverage. As a conceptual example, consider branch growth in trees, where new branches tend to grow into open spaces between trees offering increased access to sunlight between existing trees and branches. The conditional nature of the problem is of particular interest, namely, we wish to describe the number, length, and direction of branches growing from a particular base, given the location of all other bases in the data set.

A more specific example motivating the current study involves the spatial growth and replacement patterns of epidermal nerve fibers (ENFs) in skin samples. ENFs are thin sinuous fibers branching from root ganglion cells in the dermis and terminating at all levels of the epidermis. The basic structure of ENFs is a tree-like structure with a "trunk" entering the epidermis from the dermis and "branches" spreading in different directions ending in terminal nodes that transmit sensations of heat and pain through the ENFs to the central nervous system. Kennedy et al. (1996) first imaged ENFs from skin biopsies via confocal microscopy, revealing intriguing spatial patterns. ENFs appear in the epidermis throughout the body, however, the number of ENFs per square unit of skin decreases as one moves to more peripheral sites in the body (i.e., the intensity of ENFs is smaller in the hands and feet than in the trunk), and several researchers have noted significant reduction in ENF intensity in patients experiencing diabetic neuropathy (nerve and sensory loss, often severe, in diabetic patients). In subsequent work, Kennedy et al. (1993 & 1996) noted that not only does the intensity decline, but the spatial distribution of ENFs also appears to change with disease progression. Leong (2005) quantified such a change in pattern by showing increased clustering (as measured by the pair correlation function) in the distribution of ENF trunks in skin samples from patients suffering small fiber sensory neuropathy (SFSN), i.e., loss of feeling preceding quantifiable reduction in the number of ENFs.

In this paper, rather than studying the differences between patients with and without neuropathy, we suggest stochastic point/fiber process models describing the observed ENF pattern in order to more precisely understand and describe the spatial structure of the ENF system as observed in skin blister biopsies. Such models provide insight into observable quantities in the images and can later be used as the basis for more extensive models, e.g., space-time models for the growth of the nerve fibers.

We suggest two types of models. First, we suggest a model where both the nerve trunks (base points) and the end points of the fibers are realizations of two independent Poisson processes. Each of the ending points are connected to one of the base points according to a probabilistic assignment mechanism. We term this a *two stage Poisson* (TSP) model. In the second, more mechanistic model, we allow a general point process for the base locations then define a cluster process for the end point locations conditioned on the realization of the base process as its parent process. This is similar to the definition of a Neyman-Scott process. However, in our model, all end points are assigned a base as their unique parent, and we refer to this model as a *non-orphan cluster* (NOC) model. In both cases above, each ending point is connected to its base point via a line segment, i.e., fibers are approximated by line segments.

The Two Stage Poisson model has some similarities with a model proposed by Foss & Zuyev (1996) for telecommunication networks. In this setting, the base process represents locations of local relay stations and the end process represent the users of the network, e.g., the locations of mobile phones or broad band users. Foss & Zuyev (1996) provide a basis for our TSP results, and we extend their results to more general end-to-base assignment. All results below are given in $\mathbb{R}^2$ (with proofs in the appendix), but can be extended into $\mathbb{R}^d$ without much effort.

2 Data

The ENF data arise from a "suction induced" skin biopsy. Using this method, some portion of the epidermis is removed from the dermis, mounted on a slide, and stained for imaging. Next, the ENFs in each slide are traced manually using confocal microscopy and stored as traces via Neurolucida software (MicroBrightField, Inc. Williston, WT). The original data are in $\mathbb{R}^3$ and come in sample "boxes" of sizes $330 \times 430 \times z \ \ \mu m$, where z varies between $20 - 50\mu m$, and samples are taken from the thigh, foot, calf, back and forearm of study subjects, see Wendelschafer-Crabb et al. (2005). In this paper, we focus on thigh data from four subjects distinguished by labels $171, 224, 230$ and 256. Because of non-isotropy in the z-direction and by the shape of the sample "box" (which is much smaller in the z direction) we use the $\mathbb{R}^2$ projection of the resulting patterns, focusing on the spatial pattern of ENF coverage across the skin, rather than their depth within the skin. The observed patterns are displayed in Figure 1. Our goal is to define a stochastic process which generates patterns similar to those observed in the data (with the proper parameter values). Quantities of particular interest, i.e., summaries of the process whose distribution we wish to mirror their empirical counterparts within the data, are the total number of fibers, the total length of fibers and the directional distribution of fibers within an image.

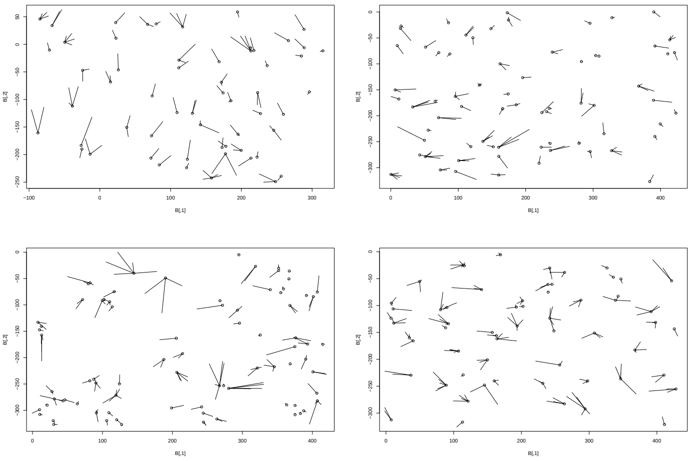

Figure 1: *Observed patterns, where the fibers are replaced by line segments connecting the end points and the base points. Top left: 171, Top right: 224, Bottom left: 230, Bottom right: 256.*

3 Two Stage Poisson model

3.1 Definition and Basic Properties

Here we assume Φ_b and Φ_e to be two independent *homogenous* Poisson processes having intensities λ_b and λ_e, respectively. We connect each end point $\mathbf{y} \in \Phi_e$ to one of the base points $\mathbf{x} \in \Phi_b$ according to the following scheme:

$$\mathbf{y} \sim \begin{cases} \mathbf{x}_o^y & \text{, with prob. } f(0\,;\theta), \\ \mathbf{x}_1^y & \text{, with prob. } f(1\,;\theta), \\ \mathbf{x}_2^y & \text{, with prob. } f(2\,;\theta), \\ \vdots & \end{cases}$$

where $\mathbf{x}_o^y$ is the point of Φ_b that is nearest to $\mathbf{y}$, $\mathbf{x}_1^y$ is the second nearest, $\mathbf{x}_2^y$ is the third nearest etc. Note that a single base may be connected to multiple (or zero) ends. The *connection probability*, $f(m\,;\theta)$, $m \in \mathbb{N}$, may depend on a parameter vector $\theta \in \mathbb{R}^k$.

We consider Φ_e as a marked point process, where the mark m of the point $\mathbf{y} \in \Phi_e$

denotes how many further points of Φ_b lie closer to $\mathbf{y}$ than the point $\mathbf{x} \in \Phi_b$, to which $\mathbf{y}$ is connected. This means that, if $\mathbf{y} \in \Phi_e$ is connected to the m^{th} nearest point of Φ_b, then the mark of $\mathbf{y}$ is $m - 1$. The marks are assumed to be independent of both processes. Concerning the number of line segments, N, and total length, L, we could also consider the following more general characteristic

DEFINITION 1. *For any measurable function* $g : \mathbb{R}^2 \to \mathbb{R}_+$, *let*

$$\Sigma_g = \sum_{\mathbf{x} \in \Phi_e} g(\mathbf{x}) \mathbf{1}_{\{\mathbf{x} \in \mathcal{O}\}}, \tag{1}$$

where $\mathcal{O}$ *denotes the set of all points of* Φ_e *which are connected to the origin.*

Then N and L are special cases of Σ_g, namely $N = \sum_{\mathbf{x} \in \Phi_e} \mathbf{1}_{\{\mathbf{x} \in \mathcal{O}\}}$ and $L = \sum_{\mathbf{x} \in \Phi_e} |\mathbf{x}| \mathbf{1}_{\{\mathbf{x} \in \mathcal{O}\}}$, respectively.

Foss & Zuyev (1996) regarded a similar type of additive functional as in Equation (1), but using the form $\tilde{\Sigma}_g = \sum_{\mathbf{x} \in \Phi_e} g(\mathbf{x}) \mathbf{1}_{\{\mathbf{x} \in \mathcal{V}_o\}}$ where $\mathcal{V}_o$ denotes the typical cell of the Poisson-Voronoi Tessellation generated by Φ_b. Their model is a special case of the one defined above, i.e. when all the mass of the mark distribution is concentrated at 0. This means that each point in Φ_e is connected to the nearest point of Φ_b, and we will refer to this as the *hard boundary* setting. In Foss & Zuyev (1996), the authors give results regarding $\tilde{\Sigma}_g$, such as expectation, variance, and covariance. Large deviation results are also given for the counterparts of N and L. It is worth noting that there is a possibility in the general Two stage Poisson (TSP) model that branches will cross. This is not the case in the hard boundary setting. It is possible to obtain results similar to Foss and Zuyev (1996) for the first moments for Σ_g in the TSP model, but analytical results regarding distribution will be very difficult to derive. Instead, we provide simulation based estimates of the densities of N and L, respectively. The estimated densities are diplayed in Figure 3 and 5, respectively.

3.2 Moments

The following proposition gives the expectation of N and L, respectively. The expectation of N is the same as in the hard boundary model of Foss & Zuyev (1996), which means that, on average, we “lose” the same amount of endings to the other bases as we “gain” from them.

PROPOSITION 1. *For N and L defined above, the following two assertions hold.*

$$E(N) = \frac{\lambda_e}{\lambda_b}$$

and

$$E(L) = \frac{\lambda_e}{\lambda_b^{\frac{3}{2}} \pi^{\frac{1}{2}}} \sum_{m=0}^{\infty} f(m\,;\,\theta) \frac{\Gamma(m+\frac{3}{2})}{\Gamma(m+1)}.$$

It is worth noting that the expectation of N does not depend on the mark distribution, but the expectation of L does. It is also possible to obtain formulas for the variances and covariances of N and L. A corresponding result for a general function g is given in Theorem 2 in the Appendix.

PROPOSITION 2. *For N and L defined above, the following holds.*

$$\begin{aligned} \text{var}(N) &= \frac{\lambda_e}{\lambda_b}\left(1 - \frac{\lambda_e}{\lambda_b}\right) \\ &\quad + \frac{2\pi\lambda_e^2}{\lambda_b^2} \sum_{m_1=0}^{\infty} \sum_{m_2=0}^{\infty} \sum_{n=0}^{\min(m_1,m_2)} \mathcal{K}_f(n, m_1, m_2, 0, 0\,;\theta) \end{aligned} \tag{2}$$

$$\begin{aligned} \text{var}(L) &= \frac{\lambda_e}{\lambda_b^2 \pi} \sum_{m=0}^{\infty} (m+1)\, f(m\,;\,\theta) \\ &\quad + \frac{\lambda_e^2}{\lambda_b^3}\left[2\pi \sum_{m_1=0}^{\infty} \sum_{m_2=0}^{\infty} \sum_{n=0}^{\min(m_1,m_2)} \mathcal{K}_f(n, m_1, m_2, 1, 1\,;\theta) \right. \\ &\quad \left. - \frac{1}{\pi}\left(\sum_{m=0}^{\infty} \frac{\Gamma\left(m+\frac{3}{2}\right)}{\Gamma\left(m+1\right)} f(m\,;\,\theta)\right)^2\right] \end{aligned} \tag{3}$$

$$\begin{aligned} \text{cov}(N, L) &= \frac{\lambda_e}{\lambda_b^{\frac{3}{2}}\sqrt{\pi}}\left(1 - \frac{\lambda_e}{\lambda_b}\right) \sum_{m=0}^{\infty} \frac{\Gamma\left(m+\frac{3}{2}\right)}{\Gamma\left(m+1\right)} f(m\,;\,\theta) \\ &\quad + \frac{2\pi\lambda_e^2}{\lambda_b^{\frac{7}{2}}} \sum_{m_1=0}^{\infty} \sum_{m_2=0}^{\infty} \sum_{n=0}^{\min(m_1,m_2)} \mathcal{K}_f(n, m_1, m_2, 0, 1\,;\theta), \end{aligned} \tag{4}$$

where

$$\begin{aligned}\mathcal{K}_f(n, m_1, m_2, p, q\,;\,\theta) = {} & \frac{f(m_1\,;\,\theta)f(m_2\,;\,\theta)\Gamma(2+m_1+m_2-n+\frac{p+q}{2})}{(m_1-n)!(m_2-n)!n!}\times \\ & \int_0^{\pi}\int_0^{\pi-u} \sin^{1+p} u \sin^{1+q} v \sin(u+v)\times \\ & (A(u,v)-\pi\sin^2 v)^{m_1-n}(\pi(\sin^2 u+\sin^2 v)-A(u,v))^n\times \\ & (A(u,v)-\pi\sin^2 u)^{m_2-n}A(u,v)^{n-2-m_1-m_2-\frac{p+q}{2}}\,dvdu,\end{aligned} \tag{5}$$

for

$$A(u,v) = \sin u \sin v \sin(u+v) + (\pi - v)\sin^2 u + (\pi - u)\sin^2 v.$$

For given n, m_1, m_2, p, q, it is possible to numerically estimate the double integral in (5). Using this, for a given f and θ we can get a numerical estimates of $\mathcal{K}_f$ and via this get numerical estimates of the series in (2)- (4). Furthermore, using Proposition 2 in the hard boundary setting we have the following results, agreeing with the corresponding result in Foss & Zuyev (1996). In the hard boundary setting, i.e. $f(0\,;\theta) = 1$, the following holds

$$\begin{aligned}\text{var}(N) &= \frac{\lambda_e}{\lambda_b} + \frac{\lambda_e^2}{\lambda_b^2}\left[2\pi\int_0^{\pi}\int_0^{\pi-u}\frac{\sin u\sin v\sin(u+v)}{A(u,v)^2}dvdu - 1\right] \\ &\approx \frac{\lambda_e}{\lambda_b} + 0.280\,\frac{\lambda_e^2}{\lambda_b^2} \qquad (6) \\ \text{var}(L) &= \frac{\lambda_e}{\pi\,\lambda_b^2} + \frac{\lambda_e^2}{\lambda_b^3}\left[4\pi\int_0^{\pi}\int_0^{\pi-u}\frac{\sin^2 u\sin^2 v\sin(u+v)}{A(u,v)^3}dvdu - \frac{1}{4}\right] \\ &\approx \frac{\lambda_e}{\pi\,\lambda_b^2} + 0.147\,\frac{\lambda_e^2}{\lambda_b^3}, \qquad (7) \\ \text{cov}(N,L) &= \frac{\lambda_e}{2\lambda_b^{\frac{3}{2}}} + \frac{\lambda_e^2}{\lambda_b^{\frac{5}{2}}}\left[\frac{3\pi^{\frac{3}{2}}}{2}\int_0^{\pi}\int_0^{\pi-u}\frac{\sin u\sin^2 v\sin(u+v)}{A(u,v)^{\frac{3}{2}}}dvdu - \frac{1}{2}\right] \\ &\approx \frac{\lambda_e}{2\lambda_b^{\frac{3}{2}}} + 0.190\frac{\lambda_e^2}{\lambda_b^{\frac{5}{2}}}. \qquad (8)\end{aligned}$$

Equations (6), (7) and (8) follow by setting $m_1 = m_2 = 0$ (and hence also $n = 0$) in Proposition 2. The approximations are obtained, via numerical integration, using the `NIntegrate` routine in Mathematica.

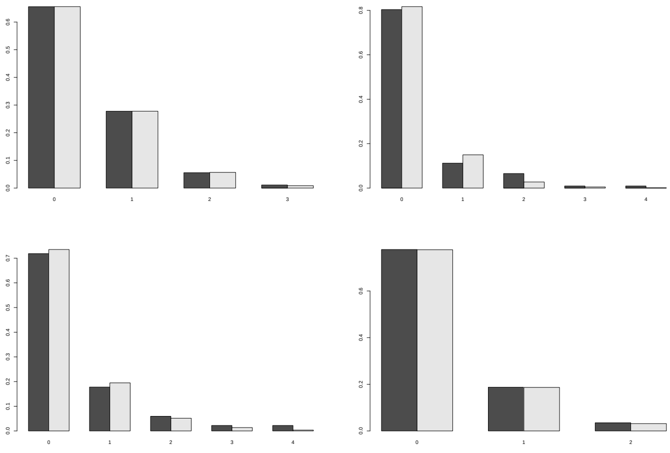

Figure 2: *Empirical (black) and model based (grey) distributions for the marks. Top left: 171, Top right: 224, Bottom left: 230, Bottom right: 256.*

3.3 Branch Length Distributions

Following Stoyan and Stoyan (1994) concerning the nearest-neighbor distribution function, the distribution of the distance from a typical point of Φ_e to its n^{th} nearest neighbor in Φ_b ($m = n - 1$, where $m = 0$ means the closest), denoted by, D_m, is given by $P(D_m \geq r) = \mathrm{e}^{-\lambda_b \pi r^2} \sum_{i=0}^{m} \frac{(\lambda_b \pi r^2)^i}{i!}$, which implies that

$$f_{D_m}(r\,;\,\lambda_b) = \frac{2(\lambda_b \pi)^{m+1}}{\Gamma(m+1)}\, r^{2m+1}\, \mathrm{e}^{-\lambda_b \pi r^2}. \tag{9}$$

Concerning the mark distribution, initial diagnostics suggests that one parameter models (e.g. Poisson) are not flexible enough for our ENF application. We therefore suggest a density of the following kind

$$f(m\,;\,\alpha,\beta) = G_\alpha(\mathrm{e}^{-\beta})^{-1}\,(m+1)^{-\alpha}\mathrm{e}^{-\beta(m+1)},\ m \in \mathbb{N},\ \alpha \in \mathbb{R}, \beta > 0. \tag{10}$$

Here, $G_\eta(\xi)$ is the polylogarithm function, also called Jonquire's function, and it is defined by $G_\eta(\xi) = \sum_{j=1}^{\infty} \frac{\xi^j}{j^\eta}$. A fit of the mark distribution to our ENF data can be seen in Figure 2. This two-parameter distribution fits the data very well. The downside of using this type of distribution is that there will most likely be no closed form expression for the branch length distribution. Still, the basic hierarchical structure of the process model allows us to obtain numerical estimates in the following manner. Using (9) and (10), the density of the branch length distribution can be written as

$$f_B(r;\lambda_b,\alpha,\beta) = \frac{2}{G_\alpha(\mathrm{e}^{-\beta})\, r}\, \mathrm{e}^{-\lambda_b \pi r^2} \sum_{m=1}^{\infty} \frac{(\lambda_b \pi r^2)^m}{\Gamma(m)}\, m^{-\alpha}\, \mathrm{e}^{-\beta m}, \tag{11}$$

which we can numerically estimate given estimates of $r, \lambda_b, \alpha, \beta$. Note that we do not need to use (11) to estimate λ_b, α and β, since these can be estimated directly from the observed base process and the marks, respectively.

A plot of the branch length distribution based on parameter values estimated from our four data sets can be seen in Figure 4 together with a kernel density estimate based on the observed branch lengths in the same data. We note some discrepancy between our estimated parametric formulation and the nonparametric density estimate, in particular, the parametric model tends to produce branches that are longer, in general, than what we observe in the data. In order to address this situation, we next consider an alternative family of models based more directly on the underlying physiological structure of ENFs.

4 Non-Orphan Cluster model

In contrast to the basic TSP structure (and giving up some of the general Poisson process based results), we now consider a two-stage point process model of ENF structure with explicit models for the connections between base and ending points. We allow the base process to be a general point process, and around each base a cluster of endings is scattered and connected to the base. This is a similar construction to a Neyman-Scott process, but in this case, we maintain information regarding to which parent each offspring belongs as part of the realization of the process, i.e., each realization of the process consists of a set of fibers defined by line segments connecting each ending to its associated base. An advantage of this approach over the TSP model is that we are no longer restricted to the use of Poisson processes but we do lose some associated convenient analytic shortcuts.

The main challenge now becomes modeling the interaction between the end points, especially, our desire for the underlying process to have a tendency to grow branches into empty spaces between base point locations. For the TSP model, this property follows by the definition of the component Poisson processes. For the Non-orphan cluster

(NOC) model with fibers generated around each base as described above, we will not see this behavior unless we model directional preference explicitly. We explore two possible angle distributions to address this issue.

4.1 Definition and Basic Properties

Using the same notation as in the previous section, the clusters are modeled in the following way. The number of points per cluster (fiber branches per base) is assumed to follow a distribution having a density given by

$$f_N(n\,;\,\delta,\gamma) = G_\delta(\mathrm{e}^{-\gamma})^{-1} n^{-\delta}\,\mathrm{e}^{-\gamma n}, \quad n = 1, 2, ... \tag{12}$$

This is a translated version of the mark density of the TSP model, given in (10). In Figure 3 a fit of f_N, together with the empirical and an simulation based estimate of the density of N in the TSP model is shown. For the TSP model there is a possibility of zero endings for a base, which is not the case in the NOC model. Furthermore, the TSP model produces more endings than are present in the data.

The positions of endings follow a bivariate distribution $\Xi = (\Theta, B)$, where Θ, B are independent and represent the angle and distance between the offspring and the parent point. Also the Ξ's are assumed to be mutually independent. The distances from ending to base are modeled as independent gamma distributed random variables, i.e. $B \sim \Gamma(\mu, \tau)$. In Figure 4 we plot the density of B for the model with parameters estimated from respective pattern, and also a kernel density estimate based on observed branch lengths. The fit of the Γ-distribution to the data is very good. The assumptions above mean that

$$f_L(x; \mu, \tau, \delta, \gamma) = \frac{1}{G_\delta(\mathrm{e}^{-\gamma})\,x}\,\mathrm{e}^{-\tau x} \sum_{n=1}^{\infty} \frac{(\mathrm{e}^{-\gamma}(\tau x)^{\mu})^n}{n^\delta \Gamma(n\mu)}. \tag{13}$$

For given x and parameters $\mu, \tau, \delta, \gamma$ it is possible to numerically estimate this density. In Figure 5 we plot the density f_L for each pattern together with a kernel density estimate based on the data.

4.2 Angle Distributions

In this section we will discuss two different options when it comes to angle distributions. In both cases the distributions are conditional on the base process. The first approach

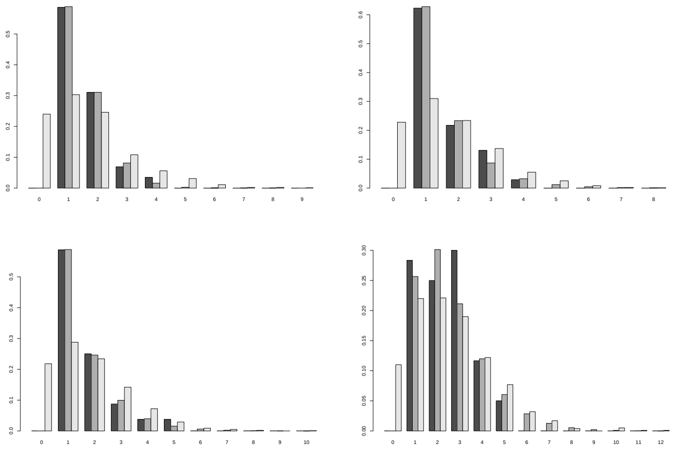

Figure 3: *Empirical (black) and model based, NOC (dark grey) TSP (light grey), distributions for the number of endings per base. The density for the TSP model is an simulation based estimate. Top left: 171, Top right: 224, Bottom left: 230, Bottom right: 256.*

is based on the angle to the nearest neighbor and the second is through all neighboring points. We will first use a modified version of the *von Mises* distribution, often used in directional statistics (Fisher (1993)), leading to a density of the following kind

$$f_\Theta(\theta; \kappa, \tilde{\theta}) = \frac{1}{2\pi I_o(\kappa)} \exp\{-\kappa \cos(\theta - \tilde{\theta})\}, \quad \theta \in (0, 2\pi),$$

where $\tilde{\theta}$ is the angle between the x-axis and the nearest neighbor of the typical point of the base process (i.e. the origin) and $I_j(\kappa)$ is the modified Bessel function of order j. This means that the distribution of Θ will be centered around $\tilde{\theta} + \pi$, i.e. more likely to produce branches in directions away from the nearest other base.

The second approach to define an angle distribution with directional reference for open space is to consider the conditional angle distribution from a hard-boundary TSP model where each ending point is connected to the closest base point. Conditional on the base process, the position of a randomly chosen ending X, connected to the origin, has a uniform distribution over the typical cell of the Voronoi tessellation generated by the base process, $\mathcal{V}_o$. This means X has the density $f_X(\mathbf{x}\,; \mathcal{V}_o) = |\mathcal{V}_o|^{-1}$, $\mathbf{x} \in \mathcal{V}_o$, where $|\cdot|$ denotes area. Representing X in polar coordinates, i.e. $X = (\Theta, B)$, gives

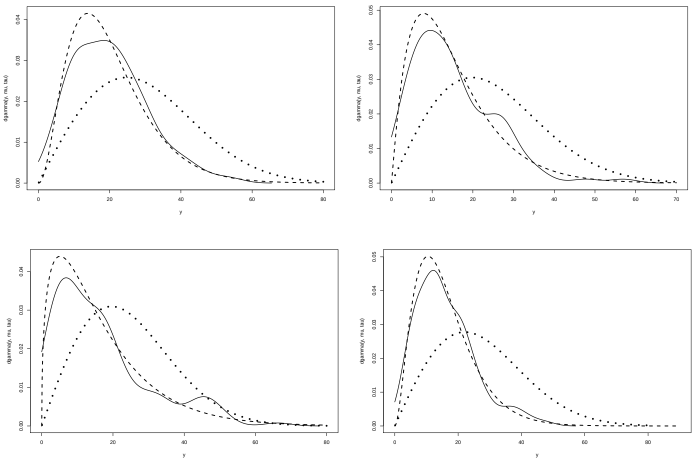

Figure 4: *Branch length densities, both model based and a kernel density estimate. TSP (..), NOC (- -), Kernel estimate (–). Top left: 171, Top right: 224, Bottom left: 230, Bottom right: 256.*

$f_{\Theta,B}(\theta, r\,;\,\mathcal{V}_o^p) = r|\mathcal{V}_o|^{-1}$, $(r,\theta) \in \mathcal{V}_o^p$, where $\mathcal{V}_o^p$ is $\mathcal{V}_o$ represented in polar coordinates, i.e. $\mathcal{V}_o^p = \{(\theta, r) \,:\, 0 \leq \theta \leq 2\pi,\, 0 \leq r \leq r_{\mathrm{m}}(\theta)\}$. Here, $r_{\mathrm{m}}(\theta)$ denotes the distance from the origin to the cell border, in the direction θ w.r.t. the x-axis. It then follows that $f_\Theta(\theta\,;\,\mathcal{V}_o^p) = \frac{r_{\mathrm{m}}(\theta)^2}{2\,|\mathcal{V}_o|}$. An example appears in Figure 6. Since ending points are uniformly distributed within the Voronoi cell having their parent point as generator, we see peaks associated with each vertex of the cell as we rotate around the parent location.

5 Parameter Estimates and Simulation

The intensities λ_b and λ_e can be estimated by the total number of base points or ending points, respectively, divided by the area of the study region. Further, for observations $m_1, ...m_k$, $n_1, ..., n_\ell$ and $y_1, ..., y_j$ of the marks (the number of base points closer than the attached base points), number of branches and branch lengths, respectively, we have

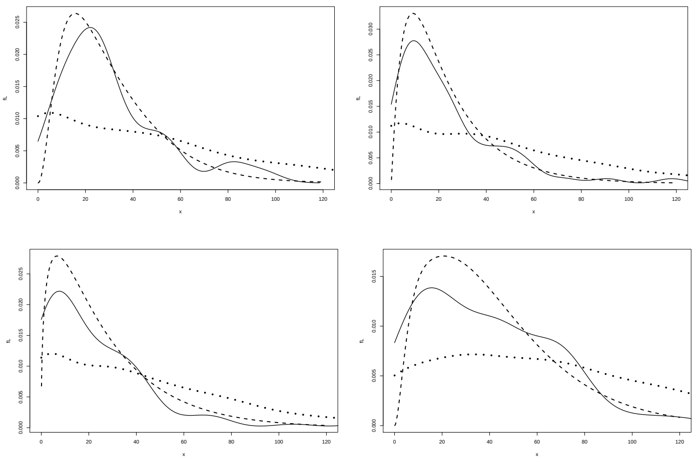

Figure 5: *Total branch length densities, both model based and a kernel density estimate. NOC (- -), TSP (..), kernel estimate (–). The density for the TSP model is an simulation based estimate. Top left: 171, Top right: 224, Bottom left: 230, Bottom right: 256.*

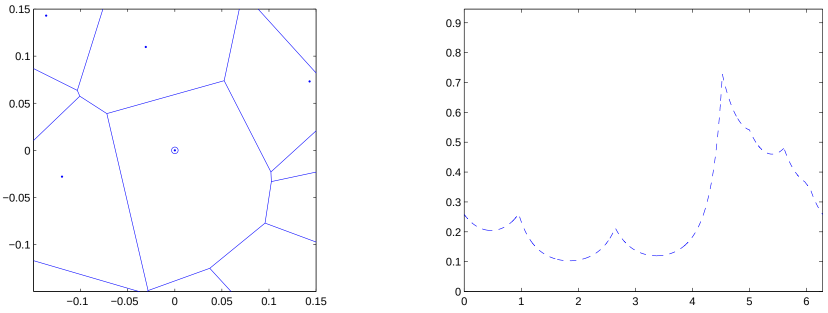

Figure 6: *Left: Typical cell of the Poisson-Voronoi tessellation generated by Φ_b; Right: Conditional Angle Distribution of branches in the typical cell (- -).*

the following log-likelihood functions for the parameters $\alpha, \beta, \delta, \gamma, \mu$ and τ,

$$\begin{aligned}\ell(\alpha,\beta) &= -k\log\left(G_\alpha(\mathrm{e}^{-\beta})\right) - k\alpha\,\overline{\log{(m+1)}} - k\beta\,(\overline{m}+1),\\ \ell(\delta,\gamma) &= -\ell\log G_\delta(\mathrm{e}^{-\gamma}) - \ell\delta\,\overline{\log n} - \ell\gamma\,\overline{n},\\ \ell(\mu,\tau) &= j\mu\log\tau + j(\mu+1)\overline{\log y} - j\log\Gamma(\mu) - j\tau\overline{y}.\end{aligned}$$

Sample	$\hat{\alpha}$ (s.d.)	$\hat{\beta}$ (s.d.)	$\hat{\delta}$ (s.d.)
171	-2.54 (0.05)	2.62 (0.09)	-2.44 (0.06)
224	$4 \cdot 10^{-6}$ (0.04)	1.70 (0.06)	0.34 (0.06)
230	$5 \cdot 10^{-6}$ (0.04)	1.33 (0.08)	-0.14 (0.06)
256	-0.17 (0.05)	1.01 (0.10)	-1.39 (0.04)
Sample	$\hat{\gamma}$ (s.d.)	$\hat{\mu}$ (s.d.)	$\hat{\tau}$ (s.d.)
171	2.33 (0.10)	3.23 (0.18)	0.16 (0.009)
224	0.77 (0.13)	2.09 (0.12)	0.14 (0.009)
230	0.95(0.12)	1.45 (0.09)	0.09 (0.006)
256	2.27 (0.06)	3.33 (0.15)	0.12 (0.006)
	$\hat{\kappa}$ (s.d.)	$\hat{\lambda}_b$ (s.d.)	$\hat{\lambda}_e$ (s.d.)
171	0.05 (0.15)	0.0004 (0.0001)	0.0006 (0.0001)
224	0.03 (0.14)	0.0005 (0.0001)	0.0008 (0.0001)
230	0.39 (0.13)	0.0006 (0.0001)	0.0010 (0.0001)
256	0.04 (0.13)	0.0004 (0.0001)	0.0010 (0.0001)

Table 1: *Parameter estimates*

We use numerical methods to maximize these. Furthermore, in order to estimate κ using maximum-likelihood it follows that we need to solve

$$\frac{I_1(\kappa)}{I_o(\kappa)} = -\frac{1}{\sum_{j=1}^{k} n_j} \sum_{j=1}^{k} \sum_{i=1}^{n_j} \cos(\theta_{ij} - \tilde{\theta}_j),$$

which is done numerically. Here we have observed the angles θ_{ij} and the nearest neighbor angles $\tilde{\theta}_j$, $i = 1, ..., n_j$, $j = 1, ..., k$, and assume that κ is a global parameter. However, there could be different κ's for each base. However, with the present data there are too few endings per base to get good estimates of the individual κ's.

In Table 5 estimates of the parameters are displayed for respective sample. It should be noted that $\lim_{\kappa \to 0} f_{\Theta}(\theta\,;\,\kappa, \tilde{\theta}) = (2\pi)^{-1}$, and also $\lim_{\alpha \to 0} f_M(m\,;\,\alpha, \beta) = \mathrm{e}^{-\beta m}(1 - \mathrm{e}^{-\beta})$. Using the estimated parameters it is possible to simulate realizations from the fitted process. In Figure 7, simulated patterns are visualized together with that subject's observed pattern. The simulations are based on the parameter estimates from sample 171. As one could see in Figure 4, the TSP model produces noticeably longer branches than there are in the observed pattern.

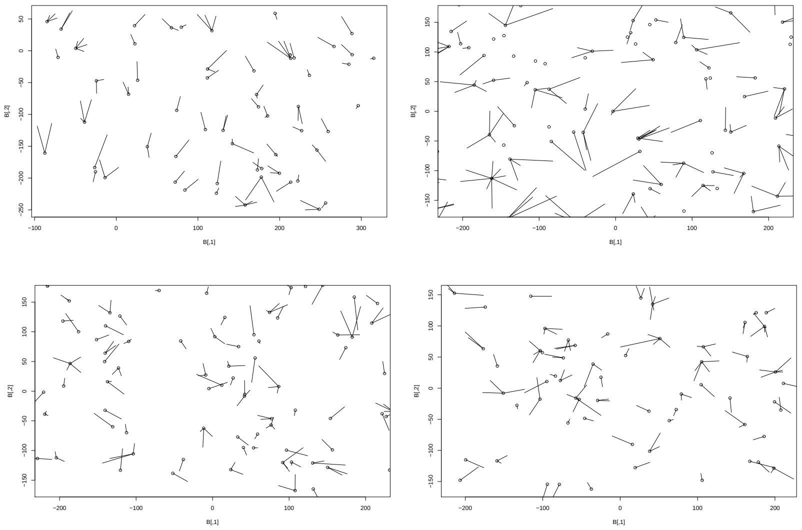

Figure 7: *Simulated ENF structures based on proposed models. Top left: Data, 171, Top right: TSP model, Bottom left: NOC model with von Mises angular distribution, Bottom right: NOC model with conditional angular distribution.*

6 Discussion

In the sections above, we propose and compare two classes of two-stage point processes to describe particular aspects of the spatial distribution of epidermal nerve fibers (ENFs) observed in microscopy images obtained in studies of peripheral neurology. The features of interest involve the number, length, and direction of branches growing from base points. For the ENF application, the *conditional* distributions of fiber properties given the location of base points are of interest in order to quantify changes in pattern which have been qualitatively observed in previous neurological studies.

The first class is based on independent Poisson processes defining the base and end points of the fibers, building on previous "territory"-based models from telecommunications. The attraction of the two-stage Poisson (TSP) approach is the wealth of theoretical properties associated with Poisson process and Voronoi tessellations which may be used as building blocks to construct the conditional distributions of interest. Unfortunately, the models as presented here do not provide sufficient flexibility to capture some aspects of pattern observed in our data, particularly the observed fiber length distribution as illustrated in the preceding section. This problem appears to be a direct aspect of allowing generality in the base-to-end assignment, and reveals an underlying identifiability complication in the class of TSP models.

The second class of models represents a more mechanistic model of fiber structure wherein we distribute base points, then generate the associated endpoints for the fibers originating at each base. These non-orphan cluster (NOC) models avoid ambiguous base assignment and take advantage of the physiological structure of the system under study, but result in more involved calculation of the conditional distributions of the fiber properties of interest than in the TSP models. The increased detail involved in specifying the NOC process appears to be justified by improved fit to the data and improved inference regarding the quantities of interest.

Using our ENF data, we estimate the parameters defining the distributions of both the number and direction of branches (both conditional on the number and location of base points) via maximum likelihood. These distributions in turn define the overall distribution of branch lengths (again, conditional on the base locations). For our data, we observe that the Poisson-process-based TSP model defined in section 4 tends to overpredict the number of base locations without branches, and also overestimates branch length. It is possible that extending the TSP model by allowing more general (i.e., non-Poisson) point processes for both the base and end locations may alleviate this problem, however, the need to accurately estimate parameters associated with end-to-base assignment likely hampers general application of the TSP process in our and similar applications. In contrast, the NOC process defined in Section 5 accurately captures the number of fibers per base, the individual branch length distribution for each base, and the distribution of total branch length observed in our data. While the NOC model is less general than the TSP formulation, it does appear that the mechanistic structure leads to much more specific inference for our application.

The next steps in the statistical analysis of spatial patterns in traced ENF microscopy images include investigation of variations in the estimated process characteristics (distributions of number, length, and direction of fibers) between observations on the same subject and between different subjects at various levels of disease progression. Such analyses will explore the diagnostic capability of quantified spatial pattern to identify disease state, perhaps offering additional diagnostic tools for early-stage neuropathy.

In addition, confocal images represent cross-sectional snapshots of a dynamic process of ENF growth and removal. For example, initial within-subject temporal replicates of ENF data following removal of a section of the epidermis (e.g., through the removal of a blister) suggest adaptive growth pattern wherein branches extend from existing base locations into denervated areas until new base locations can be established again Wendelschafer-Crabb et al. (2006). Such results suggest extensions allowing the addition of a temporal component to the NOC process wherein the number, length, and direction of ENF growth adapts to changes in the distribution of base points.

Finally, there appears to be suggestion of global anisotropy in the direction of branches in the data, see e.g. the top left in Figure 7. One way to incorporate this into the NOC model would be to use a more generalized von Mises type of distribution, with density on the form

$$f_\Theta(\theta\,;\,\theta_g,\tilde{\theta},\mu,\kappa) \propto \exp\left\{\mu\cos(\theta-\theta_g)-\kappa\cos(\theta-\tilde{\theta})\right\}, \tag{14}$$

where θ_g is a global direction for fibers to tend to. Depending on the values of κ and μ, it may be possible to extend the model to produce an anisotropic pattern.

In summary, two-stage (or more generally, hierarchical) point process models offer a rich framework for describing and quantifying observed spatial structure in peripheral neuropathy.

7 Acknowledgements

The authors wishes to thank William R. Kennedy, Gwen Wendelschafer-Crabb and Ioanna Panoutsopoulou at the Kennedy Research Laboratory at the University of Minnesota Medical Center for introducing us to this very interesting problem, providing us with the data and also for their great hospitality. Furthermore, the authors are very grateful for useful comments and suggestions from Aila Särkkä and Tommy Norberg. Viktor Olsbo appreciate the financial support from the Swedish Foundation for Strategic Research.

References

[1] FISHER, N.I. (1993) *Statistical Analysis of Circular Data*, New York. Cambridge.

[2] FOSS, S. AND ZUYEV, S. (1996) *On a Voronoi Aggregative Process Related to a Bivariate Poisson Process*, Adv. Appl. Prob., **28**, pp. 965-981.

[3] KENNEDY, W.R., WENDELSCHAFER-CRABB, G. AND JOHNSON, T. (1996) *Quantitation of epidermal nerves in diabetic neuropathy*, Neurology, **47**, 1042-1448.

[4] KENNEDY, W.R., AND WENDELSCHAFER-CRABB, G. (1993) *The innervation of human epidermis*, Journal of the Neurological Sciences **115**, 184-190.

[5] LEONG, T. (2005) First- and Second-Order Properties of Spatial Point Processes in Biostatistics. Ph.D. dissertation, Department of Biostatistics, Rollins School of Public Health, Emory University. Atlanta, GA.

[6] STOYAN D. (1984) *On Correlations of Marked Point Processes*, Math. Nachr., **116**, 197–207.

[7] STOYAN D., KENDALL W.S. AND MECKE J. (1995) *Stochastic Geometry and its Applications, 2ed*, John Wiley & Sons

[8] STOYAN D. AND STOYAN H. (1994) *Fractals, Random Shapes and Point Fields*, John Wiley & Sons

[9] WENDELSCHAFER-CRABB, G., WALK, D., FOSTER, S. AND KENNEDY, W.R. (2005) *Epidermal nerve fibre densities in six body locations of normal and diabetic subjects*, Journal of the Peripheral Nervous System **10**, 104.

[10] WENDELSCHAFER-CRABB, G., KENNEDY, W.R. AND WALK, D. (2005) *Morphological features of nerves in skin biopsies*, Journal of the neurological sciences **242**, 15-21.

8 Appendix

Here we give proofs of the theorems in the main section of the paper, and also state more general versions of them. The space of marks is denoted by $\mathbb{M}$. Furthermore, the following two results are key elements to proving the main results. For a marked homogenous point process Ψ, we have for measurable function $h : \mathbb{R}^2 \times \mathbb{M} \to \mathbb{R}_+$

$$E\left(\sum_{[\mathbf{x};\, m]\in\Psi} h(x,m)\right) = \lambda \int_{\mathbb{R}^2}\int_{\mathbb{M}} h(x,m)M(dm)d\mathbf{x}, \tag{A1}$$

and further for measurable function $g : \mathbb{R}^2 \times \mathbb{R}^2 \times \mathbb{M} \times \mathbb{M} \to \mathbb{R}_+$

$$
\begin{aligned}
&E\left(\sum_{\substack{[\mathbf{x}_1 : m_1],[\mathbf{x}_2 : m_2] \in \Psi \\ \mathbf{x}_1 \neq \mathbf{x}_2}} g(\mathbf{x}_1, \mathbf{x}_2, m_1, m_2) \right) \\
&= \int_{\mathbb{R}^2} \int_{\mathbb{R}^2} \int_{\mathbb{M}\times\mathbb{M}} g(\mathbf{x}_1, \mathbf{x}_2, m_1, m_2) M_{\mathbf{x}_1,\mathbf{x}_2}(d(m_1, m_2)) \varrho^{(2)}(\mathbf{x}_1, \mathbf{x}_2) d\mathbf{x}_1, d\mathbf{x}_2,
\end{aligned}
$$

where $M_{\mathbf{x}_1,\mathbf{x}_2}$ is the *two-point mark distribution* for Ψ and $\varrho^{(2)}$ is the second-order product density for the underlying unmarked point processes associated with Ψ, Stoyan et al. (1995) and Stoyan (1984). Since Φ_e is a homogenous Poisson process, it follows that $\varrho^{(2)}(\mathbf{x}_1, \mathbf{x}_2) = \lambda_e^2$. If we assume independent marking, it follows that $M_{\mathbf{x}_1,\mathbf{x}_2}(d(m_1, m_2)) = M(dm_1)M(dm_2)$. In our case M will always have a density w.r.t. the counting measure. In the following, we further use that we can write

$$
\Sigma_g = \sum_{[\mathbf{x};\, m] \in \Phi_e} g(\mathbf{x}) \mathbf{1}_{\{\Phi_b(b(\mathbf{x},|\mathbf{x}|))=m\}}
$$

, where $b(\mathbf{x}, r) = \{\mathbf{y} \in \mathbb{R}^2 : |\mathbf{y} - \mathbf{x}| \leq r\}$. We will use the notation $b_\mathbf{x} = b(\mathbf{x}, |\mathbf{x}|)$. The distribution of Φ_b correspond to a reduced Palm distribution at the origin, i.e. we condition on Φ_b with a point at the origin and then regard $\Phi_b \backslash \{o\}$. Based on these assumptions we have the following Theorem.

THEOREM 1. *For any measurable $g : \mathbb{R}^2 \to \mathbb{R}_+$ and mark density f w.r.t. counting measure,*

$$
E(\Sigma_g) = \lambda_e \sum_{m=0}^{\infty} \frac{f(m\,;\,\theta)(\lambda_b \pi)^m}{m!} \int_{\mathbb{R}^2} g(\mathbf{x}) |\mathbf{x}|^{2m} \mathrm{e}^{-\lambda_b \pi |\mathbf{x}|^2} d\mathbf{x}.
$$

Proofs of Theorem 1 and Proposition 1. We have that

$$
\begin{aligned}
E(\Sigma_g) &= E\left(\sum_{[\mathbf{x};\, m] \in \Phi_e} g(\mathbf{x}) \mathbf{1}_{\{\Phi_b(b_\mathbf{x})=m\}} \right) \\
&= E\left(E\left(\sum_{(\mathbf{x};\, m) \in \Phi_e} g(\mathbf{x}) \mathbf{1}_{\{\Phi_b(b_\mathbf{x})=m\}} \middle| \sigma(\Phi_b) \right) \right) \\
&= \lambda_e E\left(\int_{\mathbb{R}^2} \int_{\mathbb{M}} g(\mathbf{x}) \mathbf{1}_{\{\Phi_b(b_\mathbf{x})=m\}} M(dm) d\mathbf{x} \right) \\
&= \lambda_e \int_{\mathbb{R}^2} \int_{\mathbb{M}} g(\mathbf{x}) pr\{\Phi_b(b_\mathbf{x}) = m\} M(dm) d\mathbf{x}.
\end{aligned}
$$

The result now follows since $P(\Phi_b(b_{\mathbf{x}}) = m) = \frac{(\lambda_b \pi |\mathbf{x}|^2)^m}{m!} \, \mathrm{e}^{-\lambda_b \pi |\mathbf{x}|^2}$. Furthermore, Proposition 1 follows by using Theorem 1 above with $g(\mathbf{x}) = |\mathbf{x}|^{\nu}$, for $\nu = 0$ and $\nu = 1$.

THEOREM 2. *For any measurable functions $g_1, g_2 : \mathbb{R}^2 \to \mathbb{R}_+$, we have that*

$$
\begin{aligned}
&\operatorname{cov}\left(\Sigma_{g_1}, \Sigma_{g_2}\right) \\
&= \lambda_e \sum_{m=0}^{\infty} f(m\,;\,\theta) \frac{(\lambda_b \pi)^m}{m!} \int_{\mathbb{R}^2} g_1(\mathbf{x}) g_2(\mathbf{x}) \, \mathrm{e}^{-\lambda_b \pi |\mathbf{x}|^2} |\mathbf{x}|^{2m} d\mathbf{x} \\
&\quad + \lambda_e^2 \sum_{m_1=0}^{\infty} \sum_{m_2=0}^{\infty} \sum_{n=0}^{\min(m_1, m_2)} \Bigg[f(m_1\,;\,\theta) f(m_2\,;\,\theta) \frac{\lambda_b^{m_1+m_2-n}}{(m_1-n)!(m_2-n)!n!} \times \\
&\qquad \int_{\mathbb{R}^2} \int_{\mathbb{R}^2} g_1(\mathbf{x}_1) g_2(\mathbf{x}_2) \, \mathrm{e}^{-\lambda_b U(\mathbf{x}_1, \mathbf{x}_2)} (\pi(|\mathbf{x}_1|^2 + |\mathbf{x}_2|^2) - U(\mathbf{x}_1, \mathbf{x}_2))^n \times \\
&\qquad (U(\mathbf{x}_1, \mathbf{x}_2) - \pi |\mathbf{x}_2|^2)^{m_1-n} (U(\mathbf{x}_1, \mathbf{x}_2) - \pi |\mathbf{x}_1|^2)^{m_2-n} d\mathbf{x}_1 d\mathbf{x}_2 \Bigg] \\
&\quad - \lambda_e^2 \sum_{m_1=0}^{\infty} \sum_{m_2=0}^{\infty} \Bigg[f(m_1\,;\,\theta) f(m_2\,;\,\theta) \frac{(\lambda_b \pi)^{m_1+m_2}}{m_1! m_2!} \times \\
&\qquad \int_{\mathbb{R}^2} \int_{\mathbb{R}^2} g_1(\mathbf{x}_1) g_2(\mathbf{x}_2) |\mathbf{x}_1|^{2m_1} |\mathbf{x}_2|^{2m_1} \mathrm{e}^{-\lambda_b \pi \left(|\mathbf{x}_1|^2 + |\mathbf{x}_2|^2\right)} d\mathbf{x}_1 d\mathbf{x}_2 \Bigg],
\end{aligned}
$$

where $U(\mathbf{x}_1, \mathbf{x}_2)$ is the volume of the union of two spheres centered at $\mathbf{x}_1$ and $\mathbf{x}_2$ and having radii $|\mathbf{x}_1|$ and $|\mathbf{x}_2|$ respectively.

Proof of Theorem 2. Using (A1) and changing order between expectation and integration we get

$$
E\left(E\left(\Sigma_g \,|\, \sigma(\Phi_b)\right)\right) = \lambda_e \int_{\mathbb{R}^2} \int_{\mathbb{M}} g(\mathbf{x}) P(\Phi_b(b_{\mathbf{x}}) = m) M(dm) d\mathbf{x}.
$$

Since

$$
\begin{aligned}
&E\left(E\left(\Sigma_{g_1} \Sigma_{g_2} \,|\, \sigma(\Phi_b)\right)\right) \\
&= E\left(E\left(\sum_{[\mathbf{x}_1 : m_1]} \sum_{\substack{[\mathbf{x}_2 : m_2] \\ \mathbf{x}_2 \neq \mathbf{x}_1}} g_1(\mathbf{x}_1) g_2(\mathbf{x}_2) \mathbf{1}_{\{\Phi_b(b_{\mathbf{x}_1}) = m_1,\, \Phi_b(b_{\mathbf{x}_2}) = m_2\}} \middle| \, \sigma(\Phi_b) \right) \right) \\
&\quad + E\left(E\left(\sum_{[\mathbf{x} : m]} g_1(\mathbf{x}) g_2(\mathbf{x}) \mathbf{1}_{\{\Phi_b(b_{\mathbf{x}}) = m\}} \middle| \, \sigma(\Phi_b) \right) \right),
\end{aligned}
$$

the result follows by using Equation (A1), changing order between integration and expectation and noting that

$$P(\Phi_b(b_{\mathbf{x}_1}) = m_1,\, \Phi_b(b_{\mathbf{x}_2}) = m_2) \;=\; \sum_{n=0}^{\min(m_1,m_2)} p(m_1, m_2, n)$$
$$=\lambda_b^{m_1+m_2}(U(\mathbf{x}_1,\mathbf{x}_2) - \pi|\mathbf{x}_2|^2)^{m_1}(U(\mathbf{x}_1,\mathbf{x}_2) - \pi|\mathbf{x}_1|^2)^{m_2}\mathrm{e}^{-\lambda_b U(\mathbf{x}_1,\mathbf{x}_2)}\times$$
$$\sum_{n=0}^{\min(m_1,m_2)} \frac{1}{(m_1-n)!\,(m_2-n)!\,n!}\times$$
$$\left(\frac{(\pi(|\mathbf{x}_1|^2 + |\mathbf{x}_2|^2) - U(\mathbf{x}_1,\mathbf{x}_2))}{\lambda_b(U(\mathbf{x}_1,\mathbf{x}_2) - \pi|\mathbf{x}_2|^2)(U(\mathbf{x}_1,\mathbf{x}_2) - \pi|\mathbf{x}_1|^2)}\right)^n.$$

Above

$$p(m_1, m_2, n)$$
$$= P\left(\Phi_b(b_{\mathbf{x}_1}\backslash b_{\mathbf{x}_2}) = m_1 - n,\, \Phi_b(b_{\mathbf{x}_2}\backslash b_{\mathbf{x}_1}) = m_2 - n,\, \Phi_b(b_{\mathbf{x}_1}\cap b_{\mathbf{x}_2}) = n\right).$$

Proof of Proposition 2. The main part of the proof is to work out the second term in Theorem 2, for $g_1(\mathbf{x}) = |\mathbf{x}|^p$ and $g_2(\mathbf{x}) = |\mathbf{x}|^q$. The first and the last term is solved using Theorem 1. Now, let $r_1 = |\mathbf{x}_1|$, $r_2 = |\mathbf{x}_2|$, $\theta = \angle(\mathbf{x}_1, o, \mathbf{x}_2)$ and further β_1, β_2 are the external angles of the triangle $o\mathbf{x}_1\mathbf{x}_2$ (see Figure 8). By using the *Cosine Theorem*, symmetry arguments and the following change of variables $(r_1, r_2, \theta) \mapsto (D\sin u, D\sin v, \pi - u - v)$ (the interpretation of D, u, v is presented in Figure 8), which has the Jacobian $D\sin(u+v)$ it follows, for

$$S(r_1, r_2, \theta) = r_1 r_2 \sin\theta + r_1^2\beta_1 + r_2^2\beta_2,$$
$$R(r_1, r_2, \theta, m_1, m_2, n, p, q) = r_1^{1+p} r_2^{1+q}(r_1^2(\pi - \beta_1) + r_2^2(\pi - \beta_2) - r_1 r_2 \sin\theta)^n\times$$
$$(r_1 r_2 \sin\theta + r_1^2\beta_1 + r_2^2(\beta_2 - \pi))^{m_1-n}\times$$
$$(r_1 r_2 \sin\theta + r_1^2(\beta_1 - \pi) + r_2^2\beta_2)^{m_2-n},$$

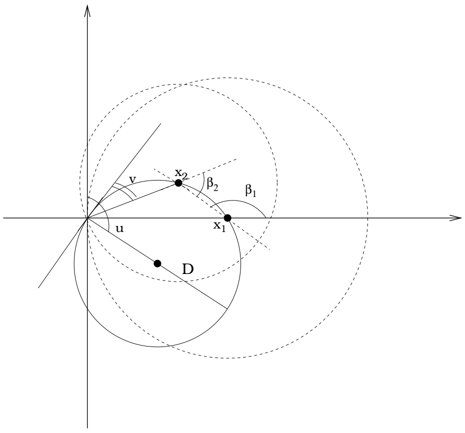

Figure 8: *Graphical explanation of the change of variables used in the proof of Proposition 2.*

that

$$
\begin{aligned}
&\int_{\mathbb{R}^2}\int_{\mathbb{R}^2} |\mathbf{x}_1|^p |\mathbf{x}_1|^q \, \mathrm{e}^{-\lambda_b U(\mathbf{x}_1,\mathbf{x}_2)} (\pi(|\mathbf{x}_1|^2 + |\mathbf{x}_2|^2) - U(\mathbf{x}_1,\mathbf{x}_2))^n \times \\
&\qquad (U(\mathbf{x}_1,\mathbf{x}_2) - \pi|\mathbf{x}_2|^2)^{m_1-n} (U(\mathbf{x}_1,\mathbf{x}_2) - \pi|\mathbf{x}_1|^2)^{m_2-n} d\mathbf{x}_1 d\mathbf{x}_2 \\
&= \int_0^\infty \int_0^\infty \int_0^\pi R(r_1,r_2,\theta,m_1,m_2,n,p,q) \, \mathrm{e}^{-\lambda_b S(r_1,r_2,\theta)} d\theta dr_1 dr_2 \\
&= 4\pi \int_0^\pi \int_0^{\pi-u} \int_0^\infty D^{3+p+q+2(m_1+m_2-n)} \sin^{1+p} u \sin^{1+q} v \sin(u+v) \times \\
&\qquad (A(u,v) - \pi \sin^2 v)^{m_1-n} (A(u,v) - \pi \sin^2 u)^{m_2-n} \times \\
&\qquad (\pi(\sin^2 u + \sin^2 v) - A(u,v))^n \mathrm{e}^{-\lambda_b D^2 A(u,v)} dD du dv, \\
&= \frac{2\pi \, \Gamma(2 + m_1 + m_2 - n + \frac{p+q}{2})}{\lambda_b^{2+m_1+m_2-n+\frac{p+q}{2}}} \int_0^\pi \int_0^{\pi-u} \sin^{1+p} u \sin^{1+q} v \sin(u+v) \times \\
&\qquad (A(u,v) - \pi \sin^2 v)^{m_1-n} (A(u,v) - \pi \sin^2 u)^{m_2-n} \times \\
&\qquad (\pi(\sin^2 u + \sin^2 v) - A(u,v))^n \, A(u,v)^{n-2-m_1-m_2-\frac{p+q}{2}} du dv,
\end{aligned}
$$

which completes the proof.

Paper IV

Applied Probability Trust (December 4, 2008)

ON THE CORRELATION BETWEEN THE VOLUMES OF THE TYPICAL POISSON-VORONOI CELL AND THE TYPICAL STIENEN SPHERE

VIKTOR OLSBO,* *Chalmers University of Technology and Göteborg University*

Abstract

In this paper we regard a tessellation $\mathcal{V}$ generated by a homogenous Poisson process Φ in $\mathbb{R}^d$, and further the random set of spheres with centers being the points in Φ and having radius half the distance to the closest other point in Φ. In $\mathbb{R}^d$ we give an integral formula for the correlation between the volume of the typical cell and the volume of the sphere in the typical cell, and we also show that this correlation is strictly positive. Further, on the real line we give an analytical expression for the correlation and in the plane and in space we give simplified integral formulas. Numerical values for the correlation for d=2,...,7 are also given.

Keywords: Correlation, Poisson process, Robbins' formula, Stienen model, Typical Cell, Voronoi tessellation

2000 Mathematics Subject Classification: Primary 60D05
Secondary 60G55

1. Introduction

Let Φ be a homogenous Poisson process in $\mathbb{R}^d$ with intensity $\lambda \in (0, \infty)$ and let $\mathcal{V}$ denote the tessellation generated by Φ. This means that for each point $\mathbf{x} \in \Phi$ we let $\mathcal{V}_\mathbf{x}$ be the cell that has the point $\mathbf{x}$ as nucleus (or generator), i.e.

$$\mathcal{V}_\mathbf{x} = \{\mathbf{y} \in \mathbb{R}^d \, : \, ||\mathbf{y} - \mathbf{x}|| \leq ||\mathbf{y} - \mathbf{z}||, \, \mathbf{z} \in \Phi\},$$

and then

$$\mathcal{V} = \{\, \mathcal{V}_\mathbf{x} \, : \, \mathbf{x} \in \Phi \,\}.$$

The tessellation $\mathcal{V}$ is known as the *Poisson-Voronoi tessellation* and was introduced by Meijering [5]. For a more in-depth view on Poisson-Voronoi Tessellations Møller [6] and Okabe *et al.* [10] are good starting points. Calka [1] [2] investigated size and form of Voronoi cells in the plane. Hug, Reitzner and Schneider [4] investigated the shape of large Voronoi cells.

In order to describe statistical properties of $\mathcal{V}$ it is useful to introduce the *typical cell.* Following [6] we let Γ denote the set of polytopes in $\mathbb{R}^d$ equipped with a "suitable" σ-field $\mathcal{A}$. For a set $A \in \mathcal{A}$ we define the following distribution

$$Q(A) = \frac{1}{\lambda \, \nu_d(B)} \mathbb{E}\left[\sum_{\mathbf{x} \in \Phi \cap B} \mathbf{1}(\mathcal{V}_\mathbf{x} - \mathbf{x} \in A)\right],$$

for an arbitrary Borel set B s.t. $0 < \nu_d(B) < \infty$. Here, ν_d denotes the Lebesgue measure. The typical Voronoi cell is defined as the random polytope $\mathcal{V}_\mathbf{t}$ on $(\Gamma, \mathcal{A})$ having distribution Q. It is known, see e.g. [6], that $\mathcal{V}_\mathbf{t}$ has the same distribution as $\mathcal{V}_o$, where $\mathcal{V}_o$ denotes the cell having the origin as nucleus. This means that the distribution P of Φ is given by the Palm distribution at the origin. To emphasise this we use the notation Φ_o. On the real line $\nu_1(\mathcal{V}_o) \sim \Gamma(2, 2\lambda)$ and for $\mathbb{R}^2$ Calka [2] gives an expression for both the density of the number of neighbours as well as

---

* Postal address: Mathematical Sciences, Chalmers University of Technology, SE-41296, Gothenburg, Sweden. E-mail: vikol@chalmers.se

the conditional distribution function of the area of the typical cell, conditioned on the number of neighbours. For $d \geq 3$, the distribution of the volume of the typical cell is unknown.

Around each point $\mathbf{x} \in \Phi$ we place a sphere with diameter being equal to the distance to the closest neighbor of $\mathbf{x}$. The random closed set made up of the union of these spheres is known as the Stienen model and was introduced by Stienen [9] motivated by an application in material science. Conditioning on Φ having a point at the origin, we call the sphere having the origin as center the *typical Stienen sphere* (or the typical sphere) and denote it by $\mathcal{S}_o$. Distributional properties of the Stienen model are studied by Schlater and Stoyan [8]. Although the distribution of the volumes of the typical sphere and the typical cell (at least for $d = 2$) are known the correlation between them is not available in the literature. At first it feels obvious that this correlation must be positive, but looking at the selected realizations in Figure 1.1 below the answer does not become as obvious. Since, e.g. two neighboring points lying close together often produce small spheres and large Voronoi cells.

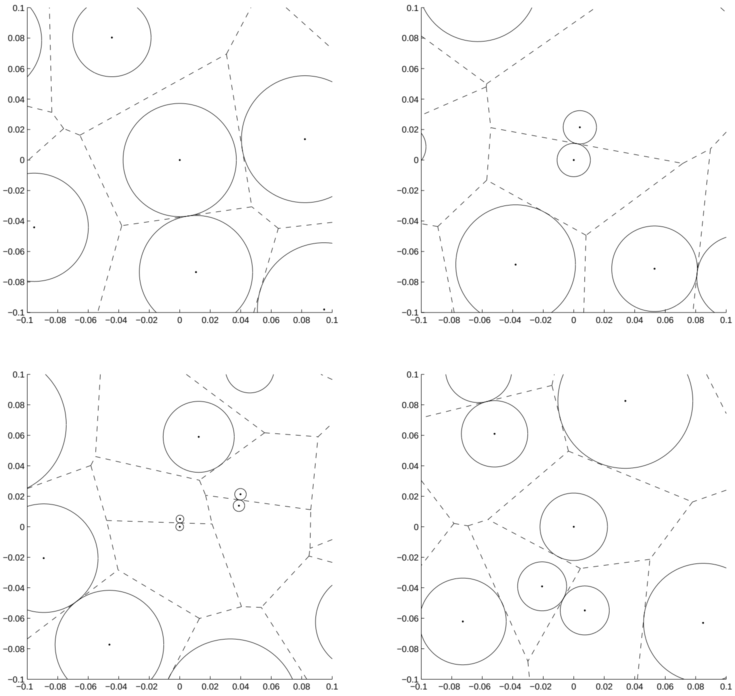

FIGURE 1.1: Examples of realizations of $\mathcal{V}_o$ and $\mathcal{S}_o$.

2. Main Results

In this section we state and discuss the main results while the proofs are left to Section 3. In Proposition 2.1 we give a closed form expression for the correlation between $\nu_1(\mathcal{V}_o)$ and $\nu_1(\mathcal{S}_o)$, and further in Theorem 2.1 we give an integral formula for $\operatorname{corr}(\nu_d(\mathcal{V}_o), \nu_d(\mathcal{S}_o))$ in arbitrary dimensions, $d \geq 2$.

Proposition 2.1. *On the real line it holds that*

$$\operatorname{corr}(\nu_1(\mathcal{V}_o), \nu_1(\mathcal{S}_o)) = \frac{1}{\sqrt{2}}. \tag{2.1}$$

The real line is the only case where we have been able to get an analytical expression for the $\operatorname{corr}(\nu_d(\mathcal{V}_o), \nu_d(\mathcal{S}_o))$. The following theorem gives an integral formula for $\operatorname{corr}(\nu_d(\mathcal{V}_o), \nu_d(\mathcal{S}_o))$ in arbitrary dimensions $d \geq 2$. Lemma 3.1 in Section 3 gives an integral formula that holds for any $d \geq 1$.

Theorem 2.1. *For $d \geq 2$, the correlation between the volume of $\mathcal{V}_o$ and the volume of $\mathcal{S}_o$ is given by*

$$\operatorname{corr}(\nu_d(\mathcal{V}_o), \nu_d(\mathcal{S}_o)) = \frac{\sigma_d^2 \int_0^\infty \int_0^{2v} u^{d-1} v^{d-1} \mathrm{e}^{-b_{d-1} W_d(u,v)} du dv - \frac{2^d - 1}{2^d}}{\sqrt{(d-1) \frac{b_d}{b_{d-1}} \int_0^\pi \int_0^\infty \frac{\sin^{d-2} \alpha \, R^{d-1}}{S_d(R,\alpha)^2} dR d\alpha - 1}}, \tag{2.2}$$

where

$$W_d(u,v) = u^d \int_{\arccos \frac{u}{2v}}^{\pi} \sin^d t dt + v^d \int_{\arccos \frac{2v^2 - u^2}{2v^2}}^{\pi} \sin^d t dt. \tag{2.3}$$

and further

$$S_d(R,\alpha) = R^d \int_\alpha^\pi \sin^d t \, dt + (R^2 + 1 - 2R\cos\alpha)^{\frac{d}{2}} \int_{T(R,\alpha)}^{\pi} sin^d t \, dt, \tag{2.4}$$

for

$$T(R,\alpha) = \arccos\left(\frac{1 - R\cos\alpha}{\sqrt{R^2 + 1 - 2R\cos\alpha}}\right).$$

Here, σ_d and b_d denote the surface area and the volume of the d-dimensional unit sphere, respectively.

The function $b_{d-1} W_d(u,v)$ can be interpreted as the volume of the union of two d-dimensional spheres with radius u and v, respectively and distance v between their centers. Furthermore, $b_{d-1} S_d(R,\alpha)$ can be interpreted as the volume of two spheres, unit distance between their centers, where one has radius R and the other has radius $\sqrt{R^2 + 1 - 2R\cos\alpha}$. For any $d \geq 2$, the integrals defining $S_d(R,\alpha)$ and $W_d(u,v)$ can be evaluated in terms of elementary functions. This means that e.g. in the plane and in space it is straightforward to use (2.2) to get numerical approximations of the correlation between $\nu_d(\mathcal{V}_o)$ and $\nu_d(\mathcal{S}_o)$.

Corollary 2.1. *In the plane and in space the following holds*

(i)

$$\operatorname{corr}(\nu_2(\mathcal{V}_o), \nu_2(\mathcal{S}_o)) = \frac{4\pi^2 \mathcal{I}_2 - \frac{3}{4}}{\sqrt{\frac{\pi}{2}\mathcal{I}_1 - 1}} \approx 0.7051,$$

where

$$\mathcal{I}_1 = \int_0^\pi \int_0^\infty \frac{R}{S_2(R,\alpha)^2} dR d\alpha,$$

for

$$S_2(R,\alpha) = \frac{1}{2}\Big\{(1 + R^2 - 2R\cos\alpha)\left(\pi - \arccos\left(\frac{1 - R\cos\alpha}{\sqrt{1 + R^2 - 2R\cos\alpha}}\right)\right) + R^2(\pi - \alpha) + R\sin\alpha\Big\}$$

and

$$\mathcal{I}_2 = \int_0^\infty \int_0^{2v} uv \, \mathrm{e}^{-2W_2(u,v)} du dv,$$

for

$$W_2(u,v) = \frac{u^2}{2}\left(\pi - \arccos\frac{u}{2v}\right) + \frac{v^2}{2}\left(\pi - \arccos\left(1 - \frac{u^2}{2v^2}\right)\right) + \frac{u}{4}\sqrt{4v^2 - u^2}$$

(ii)

$$\operatorname{corr}(\nu_3(\mathcal{V}_o), \nu_3(\mathcal{S}_o)) = \frac{16\pi^2 \mathcal{J}_2 - \frac{7}{8}}{\sqrt{\frac{8}{3}\mathcal{J}_1 - 1}} \approx 0.6778,$$

where

$$\mathcal{J}_1 = \int_0^{\pi} \int_0^{\infty} \frac{R^2 \sin\alpha}{S_3(R,\alpha)^2} dR d\alpha,$$

for

$$S_3(R,\alpha) = \frac{1}{6}(4 + 9R^2 + 4R^3 - 12R\cos\alpha + 4(1 + R^2 - 2R\cos\alpha)^{\frac{3}{2}} + 3R^2\cos 2\alpha),$$

and

$$\mathcal{J}_2 = \int_0^{\infty} \int_0^{2v} u^2 v^2 \mathrm{e}^{-\frac{\pi(3u^4+8u^3v+16v^4)}{12v}} du dv,$$

Table 1 displays numerical estimates of $\operatorname{corr}(\nu_d(\mathcal{V}_o), \nu_d(\mathcal{S}_o))$ for $d = 1, ..., 7$. The numerical results are obtained using the NIntegrate routine in Mathematica. As can be seen in Table 1 the correlation seems to decrease as the dimension increases. Using the bounds in (2.5) it follows that $\operatorname{corr}(\nu_d(\mathcal{V}_o), \nu_d(\mathcal{S}_o)) \to 0$, as $d \to \infty$.

1	2	3	4	5	6	7
0.707107	0.705143	0.677790	0.649534	0.623393	0.599667	0.578145

TABLE 1: *Approximate values of* $\operatorname{corr}(\nu_d(\mathcal{V}_o), \nu_d(\mathcal{S}_o))$ *for* $d = 1, ..., 7$.

One of the questions stated above was if the $\operatorname{corr}(\nu_d(\mathcal{V}_o), \nu_d(\mathcal{S}_o))$ is positive or not. As seen, we cannot find a closed form for the correlation between $\nu_d(\mathcal{V}_o)$ and $\nu_d(\mathcal{S}_o)$ in arbitrary dimensions but we can give a lower bound which shows that it is strictly positive. A result which is in accordance with intuition. Furthermore, we give bounds on the covariance between $\nu_d(\mathcal{V}_o)$ and $\nu_d(\mathcal{S}_o)$.

Proposition 2.2. *For any dimensions, it holds that*

(i)

$$\frac{1}{2^{2d}(1+2^d)\lambda^2} \leq \operatorname{cov}(\nu_d(\mathcal{V}_o), \nu_d(\mathcal{S}_o)) \leq \frac{1}{2^d\lambda^2}. \tag{2.5}$$

(ii)

$$\operatorname{corr}(\nu_d(\mathcal{V}_o), \nu_d(\mathcal{S}_o)) \geq \frac{1}{2^d(1+2^d)}. \tag{2.6}$$

A result which lies a little bit outside the main focus of this article is the following proposition which gives bounds on the second moment of the volume of the typical cell in arbitrary dimensions.

Proposition 2.3.

$$\frac{1}{\lambda^2} \leq \mathbb{E}[\nu_d(\mathcal{V}_o)^2] \leq \frac{2}{\lambda^2}. \tag{2.7}$$

Remark 1 The lower bound in Proposition 2.3 is elementary since $\mathbb{E}[\nu_d(\mathcal{V}_o)] = \frac{1}{\lambda}$, see (3.3). Note also that for $d = 1$ we have that $\mathbb{E}[\nu_1(\mathcal{V}_o)^2] = \frac{3}{2\lambda^2}$.

3. Proofs

A result, given by Robbins [7], that will be central in the proofs says that

$$\mathbb{E}[\nu_d(X)^n] = \int_{\mathbb{R}^d} \dots \int_{\mathbb{R}^d} P(\mathbf{x}_1, \dots, \mathbf{x}_n \in X) d\mathbf{x}_1 \dots d\mathbf{x}_n, \tag{3.1}$$

for any random closed set X.

3.1. Moments of the typical cell

Equation (3.1) implies that

$$\begin{aligned}\mathbb{E}[\nu_d(\mathcal{V}_o)^n] &= \int_{\mathbb{R}^d} \dots \int_{\mathbb{R}^d} P(\mathbf{x}_1, \dots, \mathbf{x}_n \in \mathcal{V}_o) d\mathbf{x}_1 \dots d\mathbf{x}_n \\ &= \int_{\mathbb{R}^d} \dots \int_{\mathbb{R}^d} \mathrm{e}^{-\lambda U_d(\mathbf{x}_1, \dots, \mathbf{x}_n)} d\mathbf{x}_1 \dots d\mathbf{x}_n, \end{aligned} \tag{3.2}$$

where $U_d(\mathbf{x}_1, \dots, \mathbf{x}_n)$ is the volume of the union of n spheres in $\mathbb{R}^d$ with centers $\mathbf{x}_1, \dots, \mathbf{x}_n$ and radii $||\mathbf{x}_1||, \dots, ||\mathbf{x}_n||$, respectively. The property $P(\mathbf{x}_1, \dots, \mathbf{x}_n \in \mathcal{V}_o) = \mathrm{e}^{-\lambda U(\mathbf{x}_1, \dots, \mathbf{x}_n)}$ follows from the fact that the points $\mathbf{x}_1, \dots, \mathbf{x}_n$ lie inside the typical cell iff

$$\Phi_o^! \bigcap \left(\bigcup_{i=1,\dots,n} B_d(\mathbf{x}_i, ||\mathbf{x}_i||) \right) = \emptyset,$$

where $\Phi_o^!$ denotes $\Phi_o \backslash \{ o \}$ and $B_d(\mathbf{x}, r) = \{\mathbf{y} \in \mathbb{R}^d \, : \, ||\mathbf{x} - \mathbf{y}|| \leq r\}$. It is well known that

$$\mathbb{E}[\nu_d(\mathcal{V}_o)] = \frac{1}{\lambda}, \tag{3.3}$$

which is straightforward to obtain from (3.2). This result was initially given by Gilbert [3]. Unfortunately it is the only moment known in analytical form, except for the special case $d = 1$, where all moments are known. On the real line $\mathcal{V}_o$ is an interval. The distance from the origin to the left end point of $\mathcal{V}_o$ and the distance from the origin to the right end point of $\mathcal{V}_o$ are two independent Exp(2λ)-distributed random variables. This means that $\nu_1(\mathcal{V}_o) \sim \Gamma(2, 2\lambda)$ which implies that

$$\mathbb{E}[\nu_1(\mathcal{V}_o)^n] = \frac{(n+1)!}{(2\lambda)^n}. \tag{3.4}$$

3.2. Distribution of the typical sphere

Let R_o denote the radius of a typical sphere in the Stienen model, i.e. the sphere that has the origin as center. We have that $P(R_o > r) = \mathrm{e}^{-\lambda 2^d b_d r^d}$, since R_o is greater than r iff $\Phi_o^! \cap B_d(o, 2\,r) = \emptyset$. This means that

$$P(\nu_d(S_o) > s) = P(b_d R_o^d > s) = P(R_o > (s/b_d)^{\frac{1}{d}}) = \mathrm{e}^{-\lambda 2^d s}, \tag{3.5}$$

i.e. $\nu_d(S_o) \sim$Exp($2^d\lambda$), hence

$$\mathbb{E}[\nu_d(S_o)^n] = \frac{n!}{(2^d\lambda)^n}. \tag{3.6}$$

3.3. Proofs of Proposition 2.1 and Theorem 2.1

In this section we give the proofs of Theorem 2.1 and Proposition 2.1. To prove these results we will use the following lemma which gives an integral formula for the correlation between $\nu_d(\mathcal{V}_o)$ and $\nu_d(\mathcal{S}_o)$ for any d.

Lemma 3.1. *The correlation between the volume of $\mathcal{V}_o$ and the volume of $\mathcal{S}_o$ is given by*

$$\operatorname{corr}(\nu_d(\mathcal{V}_o), \nu_d(\mathcal{S}_o)) = \frac{\frac{1-2^d}{2^d} + \iint_{||\mathbf{x}_1|| \le 2||\mathbf{x}_2||} \mathrm{e}^{-V_d(\mathbf{x}_1,\mathbf{x}_2)} d\mathbf{x}_1 d\mathbf{x}_2}{\sqrt{\int_{\mathbb{R}^d}\int_{\mathbb{R}^d} \mathrm{e}^{-U_d(\mathbf{x}_1,\mathbf{x}_2)} d\mathbf{x}_1 d\mathbf{x}_2 - 1}}, \tag{3.7}$$

where $V_d(\mathbf{x}_1, \mathbf{x}_2)$ is the volume of the union of two spheres in $\mathbb{R}^d$, centered at the origin and $\mathbf{x}_2$, having radii $||\mathbf{x}_1||$ and $||\mathbf{x}_2||$, respectively.

Proof. Define $\tilde{\mathcal{V}}_o$ as the part of $\mathcal{V}_o$ that lies outside $\mathcal{S}_o$, i.e. $\tilde{\mathcal{V}}_o = \mathcal{V}_o \backslash \mathcal{S}_o$. Now, to obtain the correlation between $\nu_d(\mathcal{V}_o)$ and $\nu_d(\mathcal{S}_o)$ we first compute the covariance. We have that

$$\operatorname{var}(\nu_d(\tilde{\mathcal{V}}_o)) = \operatorname{var}(\nu_d(\mathcal{V}_o) - \nu_d(\mathcal{S}_o)) = \operatorname{var}(\nu_d(\mathcal{V}_o)) + \operatorname{var}(\nu_d(\mathcal{S}_o)) - 2\operatorname{cov}(\nu_d(\mathcal{V}_o), \nu_d(\mathcal{S}_o)),$$

which implies that

$$\operatorname{cov}(\nu_d(\mathcal{V}_o), \nu_d(\mathcal{S}_o)) = \frac{1}{2}(\operatorname{var}(\nu_d(\mathcal{V}_o)) + \operatorname{var}(\nu_d(\mathcal{S}_o)) - \operatorname{var}(\nu_d(\tilde{\mathcal{V}}_o))). \tag{3.8}$$

Now, from (3.2), (3.3) and (3.6) it follows that

$$\operatorname{var}(\nu_d(\mathcal{V}_o)) = \int_{\mathbb{R}^d}\int_{\mathbb{R}^d} \mathrm{e}^{-\lambda U_d(\mathbf{x}_1,\mathbf{x}_2)} d\mathbf{x}_1 d\mathbf{x}_2 - \frac{1}{\lambda^2}, \tag{3.9}$$

and

$$\operatorname{var}(\nu_d(\mathcal{S}_o)) = \frac{1}{(2^d\lambda)^2}. \tag{3.10}$$

It remains to find $\operatorname{var}(\nu_d(\tilde{\mathcal{V}}_o))$. The expectation is given by

$$\mathbb{E}[\nu_d(\tilde{\mathcal{V}}_o)] = \mathbb{E}[\nu_d(\mathcal{V}_o) - \nu_d(\mathcal{S}_o)] = \frac{2^d - 1}{2^d\lambda}. \tag{3.11}$$

This is what one would expect since the volume fraction of the Stienen model is equal to 2^{-d}. We will use (3.1) to find the second moment of $\nu_d(\tilde{\mathcal{V}}_o)$, and then we need to compute $P(\mathbf{x}_1, \mathbf{x}_2 \in \tilde{\mathcal{V}}_o)$. Now, for $||\mathbf{x}_1|| \le ||\mathbf{x}_2||$

$$P(\mathbf{x}_1, \mathbf{x}_2 \in \tilde{\mathcal{V}}_o) = P(R_o < ||\mathbf{x}_1||,\ \mathbf{x}_1, \mathbf{x}_2 \in \mathcal{V}_o),$$

and

$$P(\mathbf{x}_1, \mathbf{x}_2 \in \mathcal{V}_o) = P(R_o < ||\mathbf{x}_1||,\ \mathbf{x}_1, \mathbf{x}_2 \in \mathcal{V}_o) + P(R_o \ge ||\mathbf{x}_1||,\ \mathbf{x}_1, \mathbf{x}_2 \in \mathcal{V}_o).$$

Further, $\mathbf{x}_1$, $\mathbf{x}_2$ lies in $\mathcal{V}_o$ and $R_o \ge ||\mathbf{x}_1||$ iff there are no points of $\Phi_o^!$ in $B_d(o, 2||\mathbf{x}_1||) \cup B_d(\mathbf{x}_2, ||\mathbf{x}_2||)$ and therefore, $P(R_o \ge ||\mathbf{x}_1||,\ \mathbf{x}_1, \mathbf{x}_2 \in \mathcal{V}_o) = \mathrm{e}^{-\lambda V_d(\mathbf{x}_1,\mathbf{x}_2,2)}$, where

$$V_d(\mathbf{x}_1, \mathbf{x}_2, 2) = \nu_d(B_d(o, 2||\mathbf{x}_1||) \cup B_d(\mathbf{x}_2, ||\mathbf{x}_2||)).$$

Using (3.1), the above means that

$$\mathbb{E}[\nu_d(\tilde{\mathcal{V}}_o)^2] = \int_{\mathbb{R}^d}\int_{\mathbb{R}^d} \mathrm{e}^{-\lambda U_d(\mathbf{x}_1,\mathbf{x}_2)} d\mathbf{x}_1 d\mathbf{x}_2 - 2\iint_{||\mathbf{x}_1|| \le ||\mathbf{x}_2||} \mathrm{e}^{-\lambda V_d(\mathbf{x}_1,\mathbf{x}_2,2)} d\mathbf{x}_1 d\mathbf{x}_2. \tag{3.12}$$

By using (3.2), (3.6), (3.11) and (3.12), Equation (3.8) now becomes

$$\begin{aligned}\operatorname{cov}(\nu_d(\mathcal{V}_o),\, \nu_d(\mathcal{S}_o)) &= \frac{1}{2}\int_{\mathbb{R}^d}\int_{\mathbb{R}^d} \mathrm{e}^{-\lambda U_d(\mathbf{x}_1,\mathbf{x}_2)} d\mathbf{x}_1 d\mathbf{x}_2 - \frac{1}{2\lambda^2} + \frac{1}{2(2^d\lambda)^2} \\ &- \frac{1}{2}\int_{\mathbb{R}^d}\int_{\mathbb{R}^d} \mathrm{e}^{-\lambda U_d(\mathbf{x}_1,\mathbf{x}_2)} d\mathbf{x}_1 d\mathbf{x}_2 \\ &+ \iint_{||\mathbf{x}_1||\le||\mathbf{x}_2||} \mathrm{e}^{-\lambda V_d(\mathbf{x}_1,\mathbf{x}_2,2)} d\mathbf{x}_1 d\mathbf{x}_2 + \frac{(2^d-1)^2}{2(2^d\lambda)^2} \\ &= \frac{1-2^d}{(2^d\lambda)^2} + \iint_{||\mathbf{x}_1||\le||\mathbf{x}_2||} \mathrm{e}^{-\lambda V_d(\mathbf{x}_1,\mathbf{x}_2,2)} d\mathbf{x}_1 d\mathbf{x}_2. \qquad (3.13)\end{aligned}$$

Finally, (3.2), (3.6) and (3.8) imply that

$$\operatorname{corr}(\nu_d(\mathcal{V}_o), \nu_d(\mathcal{S}_o)) = \frac{\frac{1-2^d}{(2^d\lambda)^2} + \iint_{||\mathbf{x}_1||\le||\mathbf{x}_2||} \mathrm{e}^{-\lambda V_d(\mathbf{x}_1,\mathbf{x}_2,2)} d\mathbf{x}_1 d\mathbf{x}_2}{\frac{1}{2^d\lambda}\sqrt{\int_{\mathbb{R}^d}\int_{\mathbb{R}^d} \mathrm{e}^{-\lambda U_d(\mathbf{x}_1,\mathbf{x}_2)} d\mathbf{x}_1 d\mathbf{x}_2 - \frac{1}{\lambda^2}}}.$$

The change of variables $(x_{i1}, ..., x_{id}) \mapsto (y_{i1}\lambda^{-\frac{1}{d}}, ..., y_{id}\lambda^{-\frac{1}{d}})$, $i = 1, 2$, has the Jacobian λ^{-1}, giving a factor of λ^{-2} outside each double integral. We also have that $\lambda U_d(\mathbf{x}_1, \mathbf{x}_2) = U_d(\mathbf{y}_1, \mathbf{y}_2)$ and $\lambda V_d(\mathbf{x}_1, \mathbf{x}_2, 2) = V_d(\mathbf{y}_1, \mathbf{y}_2, 2)$, respectively. Furthermore, the change of variables $(x_{11}, ..., x_{1d}) \mapsto (z_{11}2^{-1}, ..., z_{1d}2^{-1})$ has the Jacobian 2^{-d} and it further holds that $V_d(\mathbf{x}_1, \mathbf{x}_2, 2) = V_d(\mathbf{z}_1, \mathbf{x}_2, 1) = V_d(\mathbf{z}_1, \mathbf{x}_2)$. The integration limits become $||\mathbf{z}_1|| \le 2||\mathbf{x}_2||$. This completes the proof.

Proofs of Proposition 2.1 and Theorem 2.1

For $d = 1$, the integrals in (3.7) can be calculated explicitly but we will instead use the fact that $\nu_1(\mathcal{S}_o)$ and $\nu_1(\tilde{\mathcal{V}}_o)$ are independent, which follows from the basic properties of the Poisson process. The above directly gives that

$$\operatorname{corr}(\nu_1(\mathcal{V}_o), \nu_1(\mathcal{S}_o)) = \sqrt{\frac{\operatorname{var}(\nu_1(\mathcal{S}_o))}{\operatorname{var}(\nu_1(\mathcal{V}_o))}} = \frac{1}{\sqrt{2}}.$$

The last equality follows from (3.4) and (3.10). For $d \ge 2$, consider the following. Let $\alpha = \angle(o, \mathbf{x}_1, \mathbf{x}_2)$, $r = ||\mathbf{x}_1 - \mathbf{x}_2||$ and $R = \frac{||\mathbf{x}_1||}{||\mathbf{x}_1-\mathbf{x}_2||}$. Then, by using the results in [3] it follows that

$$\begin{aligned}&\int_{\mathbb{R}^d}\int_{\mathbb{R}^d} \mathrm{e}^{-U_d(\mathbf{x}_1,\mathbf{x}_2)} d\mathbf{x}_1 d\mathbf{x}_2 \\ &\quad = d(d-1)b_d b_{d-1}\int_0^\infty\int_0^\pi\int_0^\infty \sin^{d-2}\alpha\, \mathrm{e}^{-b_{d-1}S_d(R,\alpha)r^d} r^{2d-1}R^{d-1} dR\, d\alpha\, dr, \qquad (3.14)\end{aligned}$$

where $S_d(R, \alpha)$ is defined in (2.4). By integrating over r, we get the double integral of the denominator in (2.2). Furthermore, (2.3) holds since $B_d(o, ||\mathbf{x}_1||) \cup B_d(\mathbf{x}_2, ||\mathbf{x}_2||) = \mathcal{S}(||\mathbf{x}_1||, t_1) \cup \mathcal{S}(||\mathbf{x}_2||, t_2)$, where $\mathcal{S}(||\mathbf{x}_1||, t_1)$ and $\mathcal{S}(||\mathbf{x}_2||, t_2)$ are two disjoint, truncated d-dimensional spheres of radius $||\mathbf{x}_1||$ and $||\mathbf{x}_2||$, respectively, truncated at a distance $t_1 = \frac{||\mathbf{x}_1||^2}{2||\mathbf{x}_2||}$ and $t_2 = \frac{2||\mathbf{x}_2||^2-||\mathbf{x}_1||^2}{2||\mathbf{x}_2||}$ from respective center. Geometric considerations and straightforward calculations give that the volume of each of these spheres is equal to b_{d-1} times the corresponding term in (2.3). Changing into polar coordinates gives the expression in the denominator of (2.2).

3.4. Proofs of Proposition 2.2 and 2.3

We will use (3.7) to get bounds on the covariance. All we need then are bounds on $\iint_{||\mathbf{x}_1||\le 2||\mathbf{x}_2||} \mathrm{e}^{-V_d(\mathbf{x}_1,\mathbf{x}_2)} d\mathbf{x}_1 d\mathbf{x}_2$. Since $V_d(\mathbf{x}_1, \mathbf{x}_2) \le b_d(||\mathbf{x}_1||^d + ||\mathbf{x}_2||^d)$, we have

$$\begin{aligned}\iint_{||\mathbf{x}_1||\le 2||\mathbf{x}_2||} \mathrm{e}^{-V_d(\mathbf{x}_1,\mathbf{x}_2)} d\mathbf{x}_1 d\mathbf{x}_2 &\ge \iint_{||\mathbf{x}_1||\le 2||\mathbf{x}_2||} \mathrm{e}^{-b_d(||\mathbf{x}_1||^d+||\mathbf{x}_2||^d)} d\mathbf{x}_1 d\mathbf{x}_2 \\ &= \frac{1}{(1+2^d)}. \qquad (3.15)\end{aligned}$$

To get an upper bound we first use that

$$\iint_{||\mathbf{x}_1||\leq 2||\mathbf{x}_2||} \mathrm{e}^{-V_d(\mathbf{x}_1,\mathbf{x}_2)} d\mathbf{x}_1 d\mathbf{x}_2 = \iint_{||\mathbf{x}_1||\leq ||\mathbf{x}_2||} \mathrm{e}^{-V_d(\mathbf{x}_1,\mathbf{x}_2)} d\mathbf{x}_1 d\mathbf{x}_2 + \iint_{||\mathbf{x}_2||\leq||\mathbf{x}_1||\leq 2||\mathbf{x}_2||} \mathrm{e}^{-V_d(\mathbf{x}_1,\mathbf{x}_2)} d\mathbf{x}_1 d\mathbf{x}_2,$$

and further, since $V_d(\mathbf{x}_1,\mathbf{x}_2) \geq b_d||\mathbf{x}_2||^d$

$$\iint_{||\mathbf{x}_1||\leq ||\mathbf{x}_2||} \mathrm{e}^{-V_d(\mathbf{x}_1,\mathbf{x}_2)} d\mathbf{x}_1 d\mathbf{x}_2 \leq \frac{2\pi^{\frac{d}{2}}}{\Gamma(\frac{d}{2})} \int_{\mathbb{R}^d} \mathrm{e}^{-b_d||\mathbf{x}_2||^d} \int_0^{||\mathbf{x}_2||} r^{d-1} dr d\mathbf{x}_2 = 1,$$

and

$$\iint_{||\mathbf{x}_2||\leq||\mathbf{x}_1||\leq 2||\mathbf{x}_2||} \mathrm{e}^{-V_d(\mathbf{x}_1,\mathbf{x}_2)} d\mathbf{x}_1 d\mathbf{x}_2 \leq \frac{2\pi^{\frac{d}{2}}}{\Gamma(\frac{d}{2})} \int_{\mathbb{R}^d} \int_{||\mathbf{x}_2||}^{2||\mathbf{x}_2||} r^{d-1} \mathrm{e}^{-b_d r^d} dr d\mathbf{x}_2 = 1 - \frac{1}{2^d}.$$

Using the above together with (3.13) proves (i). Further, by symmetry

$$\int_{\mathbb{R}^d}\int_{\mathbb{R}^d} \mathrm{e}^{-U_d(\mathbf{x}_1,\mathbf{x}_2)} d\mathbf{x}_1 d\mathbf{x}_2 = 2\iint_{||\mathbf{x}_1||\leq ||\mathbf{x}_2||} \mathrm{e}^{-U_d(\mathbf{x}_1,\mathbf{x}_2)} d\mathbf{x}_1 d\mathbf{x}_2 \leq 2, \tag{3.16}$$

where we have used that $U_d(\mathbf{x}_1,\mathbf{x}_2) \geq b_d||\mathbf{x}_2||^d$. The lower bound in (3.15) and the upper bound in (3.16) gives (ii) in Proposition 2.1. Last, since $\int_{\mathbb{R}^d}\int_{\mathbb{R}^d} \mathrm{e}^{-\lambda U_d(\mathbf{x}_1,\mathbf{x}_2)} d\mathbf{x}_1 d\mathbf{x}_2 = \mathbb{E}[\nu_d(\mathcal{V}_o)^2]$, (3.16) together with Remark 1 give Proposition 2.3.

Acknowledgements

This research has been founded by the Swedish Foundation for Strategic Research and the Swedish Research Council, through Stochastic Centre and GMMC, respectively. The author is very grateful for useful comments and suggestions from Aila Särkkä, Mats Kvarnström and Tommy Norberg. He also acknowledges the comments from the editor and an anonymous referee.

References

[1] Calka, P. (2002) *The distribution of the smallest disks containing the Poisson-Voronoi typical cell and the Crofton cell in the plane.* Adv. Appl. Prob. , **34** , 702–717.

[2] Calka, P. (2003) *Precise formulae for the distributions of the principal geometric characteristics of the typical cells of a two-dimensional Poisson-Voronoi tessellation and a Poisson line process*, Adv. Appl. Prob., **35** , 551–562.

[3] Gilbert, E.N. (1962) *Random subdivisions of space into crystals*, Ann. Math. Stat., **33**, 958–972.

[4] Hug, D., Reitzner, M., Schneider, R. *Large Poisson-Voronoi cells and Crofton cells* (2002) Adv. Appl. Prob., **34** , 702–717.

[5] Meijering, J.L. (1953) *Interface area, edge length and number of vertices in crystal aggregates with random nucleation*, Philips Res. Rep., **8**, pp. 270-290.

[6] Møller, J. (1994). *Lectures on Random Voronoi Tessellations*, Springer-Verlag, New-York.

[7] Robbins, H.E., *On the measure of a random set*, I. (1944) Annals of Math. Stat. **15**, 70-74 , II. (1945) Ibid. **16**, 342-347.

[8] Schlather, M., Stoyan, D. (1997) *The covariance of the Stienen model*, In D. Jeulin (ed) Advances in Theory and Applications of Random Sets, Singapore. World Scientific, pp. 157-174.

[9] Stienen, H. (1982), *Die Vergröberung von Karbiden in reinen Eisen-Kohlenstoff Stählen.* Doctoral Thesis, RWTH Aachen.

[10] Okabe, A., Boots, B., Sugihara, K. and Chiu, S.N. (2000) *Spatial Tessellations, Concepts and Applications of Voronoi Diagrams, 2ed*, John Wiley & Sons.